

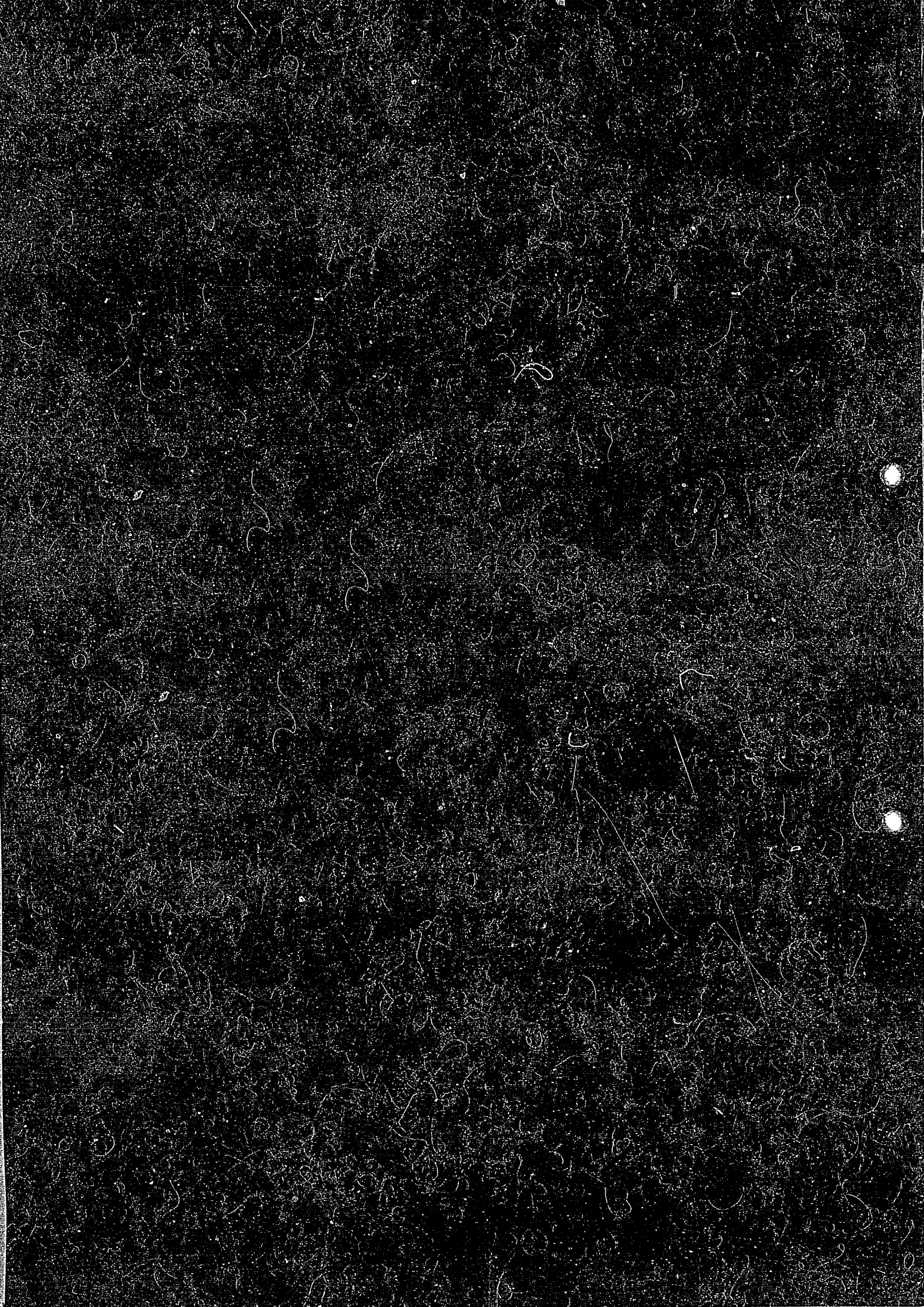
IPPJ-AM-44

**TOKAMAK PLASMA MODELLING
AND ATOMIC PROCESSES**

EDITED BY T. KAWAMURA

**INSTITUTE OF PLASMA PHYSICS
NAGOYA UNIVERSITY**

NAGOYA, JAPAN



IPPJ-AM-44

TOKAMAK PLASMA MODELLING AND ATOMIC PROCESSES

Memoirs of the Co-operative Workshop in
Institute of Plasma Physics, Nagoya University

Edited by
Takaichi KAWAMURA

Institute of Plasma Physics, Nagoya University
Chikusa-ku, Nagoya 464, Japan

June 1986

This document is prepared as a preprint of compilation of atomic data for fusion research sponsored fully or partly by the IPP/Nagoya University. This is intended for future publication in a journal or will be included in a data book after some evaluations or rearrangements of its contents. This document should not be referred without the agreement of the authors. Enquiries about copyright and reproduction should be addressed to Research Information Center, IPP/Nagoya University, Nagoya, Japan.

Preface

For the design and operation of fusion experiments the theoretical and computational works on the basis of appropriate plasma models in real devices are quite necessary. Recently such a procedure, so-called plasma modelling, has been recognized as an important field of fusion studies. As is well-known, the knowledge on many kinds of atomic processes and their data in the broad range of energy are needed for plasma modelling works.

In the Research Information Center (RIC) of Institute of Plasma Physics, Nagoya University, the collection and compilation of atomic and molecular data relevant to plasma and fusion researches are continuously being performed. In order to search a prospect of future data activities in RIC, a co-operative workshop was held on July 8-9, 1985, which was entitled Workshop on Tokamak Plasma Modelling and Atomic Processes. This workshop also was aimed at the arrangement of the contributions from RIC to the Advisory Group Meeting in Atomic Data for Fusion Plasma Modelling held at the IAEA headquarters on Sept. 18-20, 1985 (IAEA-AGM). This issue is devoted to the memoirs of the above-mentioned workshop.

Part I consists of two papers based on the talks given in the workshop. Part II consists of the papers prepared by RIC members and their collaborators as the contributions to IAEA-AGM. I would like to express my sincere thanks to Professor S. Hayakawa and all participants of the workshop for their discussions and comments on RIC activities and contributions to IAEA-AGM.

Takaichi Kawamura

CONTENTS

Preface

Part I

Particle Control in a Tokamak

S. Sengoku - - - - - 1

A Comment from a Plasma Spectroscopist---Ionizing Plasma and
Recombining Plasma

T. Fujimoto - - - - - 15

Part II

Effects of Accuracy of Atomic Data on Tokamak Impurity Transport
Modelling

T. Kawamura, T. Ono and A. Miyahara - - - - - 25

Multistep Ionization and K-Shell Ionization for Plasma Modelling of
Tokamaks

T. Kato and T. Fujimoto - - - - - 35

Plasma Spectroscopy for Plasma Modelling---VUV and X-Ray Spectroscopy
of JIPPT-IIU Tokamak Plasma

T. Kato, K. Masai and S. Morita - - - - - 57

AM Data for Fe --- Data Available and Data Needed

H. Tawara - - - - - 87

Workshop Program - - - - - 93

List of Participants - - - - - 95

PARTICLE CONTROL IN A TOKAMAK

Seio SENGOKU

Department of Thermonuclear Fusion Research,
Naka Fusion Research Establishment, JAERI

(July, 8, 1985)

A survey of the studies on particle control, for both impurity and fuel particles, on DIVA and Doublet III tokamaks is presented.

Relation between plasma-wall interactions and confinement characteristics of a tokamak plasma with respect to both impurity and fuel particle controls is discussed.

Following results are obtained from impurity control studies:

- (1) Physical models of boundary/divertor plasma and of divertor functions about impurity control are empirically obtained. By a computer simulation based on above model with respect to divertor functions for JT-60 tokamak, it is found that the allowable electron temperature of the divertor plasma is not restricted by a condition that the impurity release due to ion sputtering does not increase continuously. In this case, it is necessary to consider how to cope with handling heat load and erosion of a divertor plate.
- (2) Dense and cold divertor plasma accompanied with strong remote radiative cooling was diagnosed along the magnetic field line in the simple poloidal divertor of Doublet III tokamak. Strong particle recycling region is found to be localized near the divertor plate. In such a system, the heat load and the erosion by ion sputtering of the divertor plate are decreased.
- (3) By applying carbon coating on entire first wall of DIVA tokamak, dominant radiative region is concentrated more in boundary plasma resulting a hot peripheral plasma with cold boundary plasma. Energy confinement time of such a plasma is improved by a factor of two due to increasing of the effective radius of the core plasma by applying a carbon wall;

and from particle control studies:

- (1) The INTOR scaling on energy confinement time is applicable to high density region when a core plasma is fueled directly by solid deuterium pellet injection in Doublet III tokamak.
- (2) As remarkably demonstrated by direct fueling with pellet injection, energy confinement characteristics can be improved at high density range by decreasing particle deposition at peripheral plasma in order to reduce plasma-wall interaction.
- (3) If the particle deposition at boundary layer is necessarily reduced, the electron temperature at the boundary or divertor region increases due to decrease of the particle recycling and the electron density there. At that situation, the enhancement of impurity release can be the serious problem and thus some kind of "localized" control of particle or impurity at the boundary or near the divertor plate should be applied.

The controls of not only impurities but also fuel particles are important as shown above. Improvement of energy confinement time is demonstrated to be possible by controlling both impurity and fuel particles.

Required atomic data base for studying above scheme is presented at the last section.

1. BOUNDARY AND DIVERTOR PLASMAS

1.1 Characteristics [1,2,3,4,5]

In order to recognize the "impurity control", the following closed, cyclic processes are important (Fig.1): (1) the role of the boundary plasma on the production of impurities; (2) impurity transport in the boundary plasma and impurity flow into the main plasma; and (3) influences of accumulated impurities on the main and the boundary plasma. All of these processes and impurity control are deeply connected to the "boundary plasmas". Therefore, it is very important to understand the boundary plasma. The possible controls on those processes are also shown in the figure with important parameters in boundary plasma: temperature and density of the boundary plasma (T_b and n_b), particle flow velocity, v_f , and electric field, $E_{||}$, parallel to the magnetic field lines and the perpendicular particle diffusion coefficient, D_{\perp} .

The plasma interacts with the surrounding first walls, including limiter/divertor-neutralizer-plates, in various ways, e.g. sputtering by ions and charge-exchange neutrals and arcing. These processes strongly depend on the boundary plasma, i.e. limiter or divertor scrape-off plasmas. In this section we summarize the characteristics of the boundary plasmas.

Boundary plasma parameters are related to the main plasma through energy and particle balance. The energy balance in the stationary phase of a tokamak discharge is as follows. Total input power, P_{IN} , is balanced with these loss processes such as radiation and charge-exchange, P_R and P_{CX} , to the entire wall, and conduction-convection loss, P_{CC} , mainly onto the limiter/divertor neutralizer plate. Therefore, it can be expressed as,

$$P_S = P_{IN} - P_R - P_{CX} = P_{CC} \quad (1)$$

Here the power loss onto the surface, P_S , is the integral of local heat flux, q , as $P_S = \int q ds$. Then, the problem is how to evaluate q .

From a normal sheath theory the heat flux is given by the following equation[6]:

$$q = \gamma f_p T_e, \quad (2)$$

where f_p is the particle flux density onto the material surface and γ is the heat transmission rate across the sheath including the effects of the sheath potential, αT_e , secondary electron emission coefficient, δ , and the correction to the distribution function, F and F' . That is:

$$\gamma = \left\{ 2 \left(\frac{1}{1-\delta} + 1 \right) + \alpha \right\} F, \quad (3)$$

$$\alpha = - \ln \frac{\xi \sqrt{m/M}}{1-\delta} \cdot F', \quad (4)$$

where ξ is the ratio of the electron to ion saturation currents, and m and M are the electron and ion masses, respectively. The value F exceeds 10 in a runaway discharge, but is around unity in a normal discharge. F' is also around unity in a normal discharge. The maximum value of δ is given by space charge limit[6] as $\delta_{max} = 1 - 8.3 \sqrt{m/M}$ and is 0.81 for hydrogen and 0.86 for deuterium plasmas. Corresponding to this, γ varies between 6.7-13.5(H) and 7.0-17.0(D), respectively, in a normal discharge.

As long as the sheath is formed on the material surface, the total power loss onto the material surface is then deduced as:

$$P_S = \int q ds = F_p \gamma T_b \quad (5)$$

where $F_p = N_p / \bar{\tau}_p$ is the total particle outflux, $\bar{\tau}_p$ the overall particle confinement time, and \bar{T}_b the average boundary temperature. Then, the power balance, eq. (1), can be rewritten as

$$\begin{aligned} \gamma \frac{N_p}{\bar{\tau}_p} \bar{T}_b &= P_{IN} - P_R - P_{cx} \\ &= \frac{3}{2} \frac{N_p}{\bar{\tau}_E} (\bar{T}_i + \bar{T}_e) - P_R - P_{cx}, \end{aligned}$$

where \bar{T}_i and \bar{T}_e are the average ion and electron temperatures in the main plasma. From this, we can obtain the relation between the boundary temperature and the core temperature as

$$\bar{T}_b = \frac{3}{\gamma} \frac{\bar{\tau}_E}{\bar{\tau}_E} \left(1 - \frac{P_R + P_{cx}}{P_{IN}} \right) \bar{T}. \quad (6)$$

Other important parameters are the width of the scrape-off layer, d , average boundary density, \bar{n}_b , and particle flux density, f_p , as

$$d = \sqrt{D_{\perp} L / v_f}, \quad (7)$$

$$\bar{n}_b = \frac{1}{2} \frac{L}{v_f} \frac{a}{d} \frac{\bar{n}_e}{\bar{\tau}_p}, \quad (8)$$

$$f_p = v_f \bar{n}_b, \quad (9)$$

and the electric field, E . a is the plasma radius, D_{\perp} the perpendicular diffusion coefficient and L and v_f are the path length of the charged particles and parallel flow velocity along the field line in the scrape-off layer. Among these parameters, the essential parameters are γ , v_f , D_{\perp} , and E . These are reasonably obtained in DIVA tokamak: $\gamma \approx 7$, $v_f \approx 0.3 C_s$, $D_{\perp} \approx 0.1 D_B$ and $E \approx T_e / L$ where C_s is ion sound velocity, D_B the Bohm diffusion coefficient.

1.2 Model Calculations [1, 7, 8]

In order to understand impurity transport, computer simulations based on the physical model obtained above were performed. In the background scrape-off plasma, characterized by T_e , T_i , n_e , v_f and E , a number of test particles (impurities) are traced under the following processes by the Monte-Carlo method: (1) free motion of sputtered impurity atoms, (2) ionization in the background plasma, (3) Coulomb scattering, (4) charge exchange, and (5) perpendicular diffusion of ions.

The results of the simulation with the observed boundary plasma parameters give reasonable values on average ionic charge and the mean energy of the carbon ions in the burial chamber, as shown in Fig. 2. Moreover, the temporal impurity behaviour of each charge state through CII to CV is shown to be well simulated by this calculation, as shown in the figure.

From these results the calculation can be applied to a large device. The boundary plasma condition was investigated for JT-60. For the main plasma the parameters are given. Ion sputtering on the limiter/divertor-neutralizer-plate is added to the aforementioned Monte-Carlo calculation.

The formulae for the sputtering yields were given by Sigmund [9]. These values are, however, several times higher than the experimental data for other heavy ions [10, 11]; we have, therefore, divided Sigmund's sputtering yield by two for this calculation, S_0 . The energy and the angular distributions of sputtered impurity atoms have been obtained experimentally [12, 13]. We formalize those distributions as [8]:

$$S(E) = \frac{S_0}{(U_0/\theta)^{\beta+1}} E^{\beta} \exp(-\beta E/U_0) \frac{1}{\Gamma(\beta+1)} \quad (10)$$

$$S(\theta, \varphi) = \frac{S_0}{\pi} \cos \theta \quad (11)$$

where U_0 is the surface binding energy, sublimation energy, β is the fitting constant, $\Gamma(n)$ is the Gamma function and θ is the angle from the normal direction of the sputtered material's surface. Integrals of eqs. (10) and (11)

over E and θ are normalized to S_0 , respectively[8]. For simplicity, β is taken to be unity.

Assumed typical parameters are as follows, $\bar{\tau}_p = \bar{\tau}_E = 0.7s$, $T_{e0} = T_{i0} = 7keV$, $n_{e0} = n_{i0} = 7 \times 10^{13}/cm^3$ and $B_T = 4T$. The limiter/neutralizer plates are assumed to be made of molybdenum. Sputtered molybdenum is the only assumed impurity source.

The results are as follows. The average ionic charge of the molybdenum ions $\langle Z_I \rangle$, near the material surface is around 5 in the case with the divertor, and becomes up to 10 without the divertor. These tend to saturate because the sputtered molybdenum ions are forced to return in a shorter time as the temperatures increase (Fig.3(a)). The average energy of the impinging molybdenum ions, $\langle E_I \rangle$, is reduced by a factor of 2 by employing the divertor corresponding to the decrease of ionic charge, as $\langle E_I \rangle = \alpha \langle Z_I \rangle T_b + T_I$, where T_I is the temperature of the molybdenum ions (Fig.3(b)). The stagnation on $\langle E_I \rangle$ is due to the effect of secondary electron emission. If we neglect this effect, the result becomes much different. Impurity growth rates are shown in Fig.3(c). The growth rate is defined by a ratio $N_I(t+\Delta t)/N_I(t)$, where Δt is the impurity recycling characteristic time. Molybdenum impurities continue to increase when the boundary temperature is above 160 eV without the divertor. Owing to radiation cooling, the boundary temperature is in equilibrium at 80-160eV.

In the case without the divertor, we must lose a large portion of the input power, e.g. 80-90%, by radiation and charge-exchange losses (Fig.3(d)). In opposition to this, the molybdenum impurities continue to decrease if the divertor is employed and thus the boundary temperature is not determined by ion sputtering. The boundary temperature increases up to a few hundred eV when radiation and charge-exchange losses are greatly reduced.

1.3 Dense and Cold Divertor Plasma[14]

Dense and cold divertor plasmas with electron density and temperatures of $n_e \gtrsim 5 \times 10^{13} cm^{-3}$ and $T_e \lesssim 7eV$ have been observed previously in Joule-heated Doublet III discharges[15]. Such a dense and cold divertor plasma provides the following advantages:

(a) Because of strong density buildup, the divertor plasma can radiate considerably high power, which leads to a reduction of the heat load onto the divertor plate without deleterious effects to the main plasma.

(b) This sort of divertor is capable of effective particle exhaust, i.e. the exhaust of unused fuel particles, helium ash and other impurities.

(c) Because of a sufficiently low temperature, the erosion of the divertor plates caused by ion sputtering becomes negligibly small.

In this divertor experiment, deuterium plasma is heated for 200ms with a neutral beam injection power of $P_{NB} \approx 1.2MW$. The toroidal field is $B_T = 2T$ and the plasma current is $I_p = 290kA$. The range of the line-averaged electron density of the main plasma is $\bar{n}_e = (1.0-3.4) \times 10^{13} cm^{-3}$ and the central electron temperature is $T_e(0) = 1.2-0.7keV$, at 100ms after the start of beam injection ($t = 700ms$) when most of the measurements were taken.

The separatrix surface intersects the inconel divertor plate on the inner wall of the vacuum vessel. An array of 21 Langmuir probes and 28 thermocouples are installed in the divertor plate in order to measure the vertical profiles of the plasma parameters.

The electron density n_{ed} and temperature T_{ed} at the peak of the density profile on the lower divertor channel are shown in Fig.4 as strong functions of \bar{n}_e or gas puffing ($n_{ed} \propto \bar{n}_e^3$). The electron density n_{ed} increases nonlinearly from $6 \times 10^{12} cm^{-3}$ to $2.8 \times 10^{14} cm^{-3}$, with \bar{n}_e increasing only by a factor of 3.4. At the same time, T_{ed} has cooled down from 30 eV to 3.5eV. The two points profile measurements by the Langmuir probes near the divertor plate show that the temperature gradient along the magnetic field line is found to be very steep ($T_e = 36eV$ in front of divertor plate and $T_e = 8eV$ at the divertor plate). The connection length between these two points is 380cm(poloidal

projection length $\approx 16\text{cm}$). This result (shown with error bars) is well simulated by self consistent fluid model[16] as shown in Fig.5. The total particle flux across the first point of the profile measurement, which is deduced from the ion saturation-current profile, is $\Gamma_{\text{mi}}^{\text{mi}} \approx (3.5-7) \times 10^{21}$ particles/s (the flow velocity is assumed to be $v_f = (0.3-0.6)C_s$). The total particle flux onto the divertor plate is $\Gamma_{\text{p}}^{\text{d}} \approx 1.6 \times 10^{22}$ particles/s at $\bar{n}_e = 3 \times 10^{13} \text{cm}^{-3}$.

If the divertor plasma in a fusion reactor can be made dense and cold, analogous to the divertor plasma investigated here, the erosion of the divertor plate due to ion sputtering would be negligibly small because of sufficiently low T_{ed} and thus low sheath potential. The threshold energy for ion sputtering is approximately several tens of electron volts for materials such as titanium, iron, nickel, carbon[10].

2. IMPROVEMENT OF ENERGY CONFINEMENT CHARACTERISTICS BY IMPURITY CONTROL[17]

Low-Z materials are attractive for the first wall in a reactor because of the following reasons.

(a) Radiation loss from low-Z impurities is rather small in a high temperature plasma.

(b) The thermal properties of some low-Z material, e.g. carbon, are as good as those of copper or molybdenum.

(c) The self-sputtering yield, which is most closely related to the impurity origin, is smaller than that of the high-Z materials such as Mo. Therefore, the wall erosion is rather low.

Here we show an example of improvement of energy confinement time with controlling impurity by means of applying carbon wall.

Figure 6 shows the profiles of electron temperature and density for (a) carbon wall and (b) Ti-flushed wall. For carbon wall case, $P_{\text{R}} + P_{\text{CX}}$ that dominated by carbon line radiation is shown to be increased and concentrated more in plasma periphery compared with Ti wall case. Consequently, the boundary electron temperature is cooled down due to increase of $P_{\text{R}} + P_{\text{CX}}$ obeying eq.(6). As the result, the effective radius of plasma pressure profile increases and thus the energy confinement time is improved by a factor of 2 by employing carbon wall with divertor as shown in Fig.7. The effect of the impurity control by a divertor on improvement of energy confinement time is also shown in the figure.

Chemical sputtering is shown to be easily suppressed by prebombardment of hydrogenic ions at the substratum temperature above 500°C .

3. IMPROVEMENT OF ENERGY CONFINEMENT CHARACTERISTICS BY FUEL PARTICLE CONTROL

The good confinement discharge with divertor beam-heated plasma, so called H-mode, can be created by optimized gas fueling in Doublet III[18] as shown in Fig.8. Increasing edge recycling ($H_{\alpha\text{LIM}}$) leads to degradation of confinement characteristics. This implies that the control of fuel particle is responsible to the improvement of confinement properties.

Pellet injection is shown to be effective to reduce edge fueling and be able to improve confinement characteristics especially in high density region in both Joule- and beam-heated discharges[19,20].

In gas-fueled divertor ohmic discharges, the recycling and the neutral pressure both at the edge and the divertor region, increase nonlinearly as the density is raised above $4 \times 10^{13} \text{cm}^{-3}$. The energy confinement time saturates around 60ms (Fig.9). In contrast to that, the pellet fueled confinement time continue to improve with increased density. This is probably due to the fact that in the pellet fueled discharges both the edge pressure and the limiter recycling light are maintained at relatively low levels (Fig.9) and/or the successful density rise at the plasma center which has good

confinement properties. Preliminary analysis with 1-D tokamak code shows good agreement with experimental results, i.e. low edge recycling, peaked density profile and proportional increase of τ_E with \bar{n}_e , with assuming no change in ion transport characteristics before and after pellet injection[21] which is in contrast to the result from ALCATOR-C[22].

During continuous neutral beam heating of very high density plasmas, the confinement times remain near the improved ohmic level for the first ≈ 60 ms but then rapidly deteriorate corresponding to the increase of edge ablation. Figure 10 shows the successful central electron density rise due to pellet fueling during Joule-heating phase of a limiter discharge. But in the NB-heating phase, the edge density and the edge recycling start to increase when the fast ions from neutral beam build up.

A scheme was tested to enhance pellet penetration and reduce pellet ablation at plasma edge by briefly interrupting the neutral beams just before each pellet was injected. This is based on the relatively fast slowing-down time of fast ions in the edge plasma which is less than 10ms, and the expected dependence of the ablation on the fast ion population[23]. The energy confinement time and pellet penetration are improved over the continuous beam case for delay times not less than 8ms. Further delay shows little additional improvement (Fig.11).

A comparison of pellet ablation profiles for continuous vs. interrupted beam (Fig.12) shows that there is no significant difference in pellet penetration. However, the pellet ablation in the outer 10cm of the plasma is reduced by interrupting the beam. The reduction in the edge density and slower central density decay time as measured by the visible bremsstrahlung array. This reduction of edge ablation may account for the maintained improvement of the energy confinement time keeping low edge recycling (Fig.11-b)).

The combination of the improved confinement and the high densities has produced a significant extension of the \bar{n}_e, τ_E^* diagram (Fig.13) for Doublet III. The Lawson product $n_e(0) \cdot \tau_E^*$ is increased by a factor of 3 to 4 in both limiter and divertor discharges. The neutron production rate has been improved by a factor of 10 over limiter beam-heated plasmas of comparable gas fuelled discharges. These results are very encouraging for large nondivertor tokamaks that will rely heavily on neutral beam heating to produce energy breakeven conditions.

4. DISCUSSION AND CONCLUSION

Physical models of divertor/boundary plasmas and the divertor functions about impurity control are empirically obtained. It is shown that the active controls of both impurity and fuel particles are highly responsible to improve the plasma confinement characteristics.

The control flow-chart of plasma-surface interactions is presented in Fig.14. It is demonstrated that the control (decreasing) of plasma-surface interaction can improve energy confinement time.

For more precise modeling or understanding of such a system, following atomic data base are required:

- (1) Cross sections or rate coefficients of following various processes in the back ground plasmas for the parameter ranges $T_e = 4-200$ eV and $n_e = 10^{12}-10^{14}$ cm⁻³:

- ° ionization
- ° charge exchange
- ° radiative cooling rate (especially at several tens eV)
- ° recycling rate for various materials
- ° dissociation

- (2) Pellet ablation model with high energy ions

The methods of controlling of the recycling rate (e.g. control the wall temperature etc.) and of optimized impurity radiative cooling should also be investigated.

References

- [1]S. SENGOKU and H. OHTSUKA, J. Nucl. Mat. 93/94(1980)75.
- [2]Y. SHIMOMURA et al., Japan Atomic Energy Research Inst. Rep., JAERI-M 7457 (1979).
- [3]DIVA Group, Nucl. Fusion 18(1978)1619.
- [4]H. KIMURA et al., Nucl. Fusion 18(1978)1195.
- [5]Y. SHIMOMURA and H. MAEDA, J. Nucl. Mat. 76/77(1978)45.
- [6]G.D. HOBBS and J.A. WESSON, Culham Lab. Rep. CLM-R61(1966).
- [7]S. SENGOKU et al., Japan Atomic Energy Research Inst. Rep. JAERI-M 7918 (1978).
- [8]S. SENGOKU et al., Nucl. Fusion 19(1979)1327.
- [9]P. SIGMUND, Phys. Rev. 184(1969)383.
- [10]B.M.U. SCHEZER et al., in Plasma Wall Interaction(Proc. Int. Symp. Jülich, 1976) Pergamon Press, Oxford (1977)353.
- [11]C.F. BARNET et al., Oak Ridge Nat. Lab. Rep. ORNL -5207(1977)D.1.30.
- [12]P. HUCKS et al., J. Nucl. Mat. 76/77(1978)136.
R.V. STUART et al., J. App. Phys. 40(1969)803.
- [13]M. KAMINSKY, "Atomic and Ionic Impact Phenomena on Metal Surface", Springer Verlag(1965)Berlin, p.169.
- [14]S. SENGOKU et al., Nucl. Fusion 24(1984)415.
- [15]M. SHIMADA et al., Nucl. Fusion 22(1982)643.
- [16]S. SAITO et al., J. Nucl. Mat. 128/129(1984)131.
- [17]S. SENGOKU et al., J. Nucl. Mat.93/94(1980)178.
- [18]M. NAGAMI et al., Nucl. Fusion 24(1984)183.
- [19]S. SENGOKU et al., in Plasma Phys. Controlled Nucl. Fusion Res. (Proc. 10th Int. Conf., London, 1984)Vol.1, IAEA, Vienna (1985)405.
- [20]S. SENGOKU et al., "Improvement of Energy Confinement Time by Continuous Pellet Fueling in Beam Heated Doublet III Limiter Discharges", Nucl. Fusion (1985) in press.
- [21]S. SENGOKU, Japan Atomic Energy Research Inst. Rep. JAERI-M 85-102 (1985).
- [22]M. GREENWALD et al., in Plasma Phys. and Controlled Nucl. Fusion Res. (Pro. 10th Int. Conf., London, 1984) IAEA,Vienna, paper IAEA-CN-44/A-I-3.
- [23]S.L. MILORA, Oak Ridge National Lab. Rep. ORNL/TM-8616 (1983).

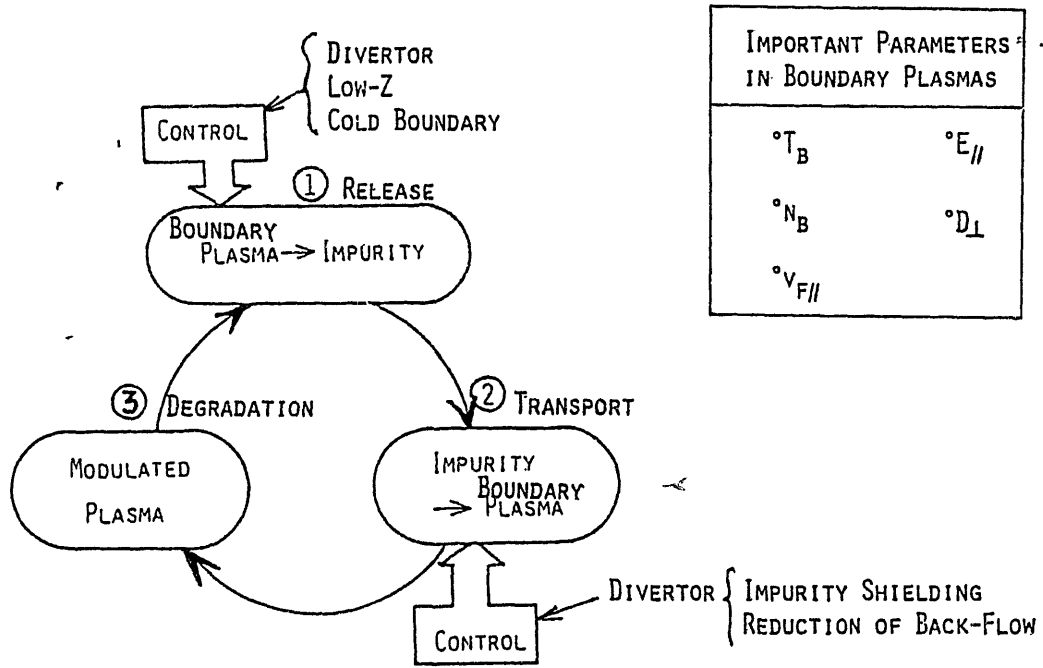


Fig. 1. Cyclic process of plasma-surface interaction.

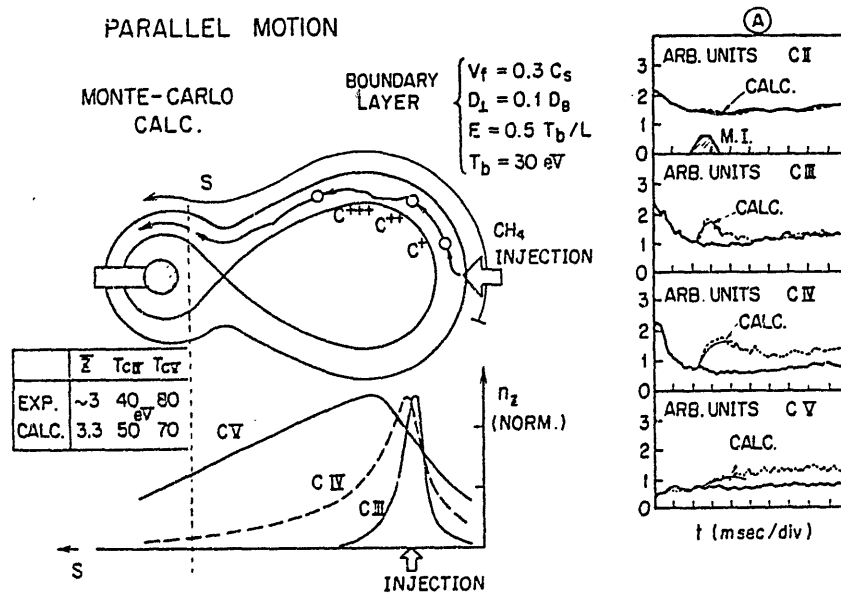


Fig. 2. Result of Monte-Carlo calculation of CH_4 injection experiment. Temporal behaviour (A), average charge state, \bar{z} , and average energies of carbon ions, T_{CIV} and T_{CV} , are shown. These are in good agreement with the experiment.

MONTE-CARLO CALCULATION

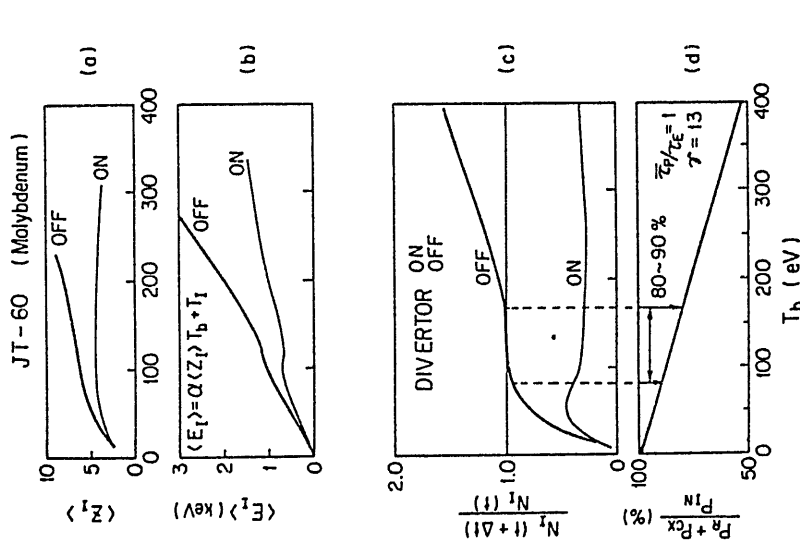


Fig. 3. Results of the simulation for molybdenum impurity recycling in JT-60: (a) average charge states, $\langle Z \rangle$; (b) average sputtering energies, $\langle E_s \rangle$; (c) impurity growth rate, $N_p(t) + \Delta t)/N_i(t)$; and (d) the ratio of radiation and charge-exchange power losses to input power, as functions of the electron temperature in the boundary plasma, T_b .

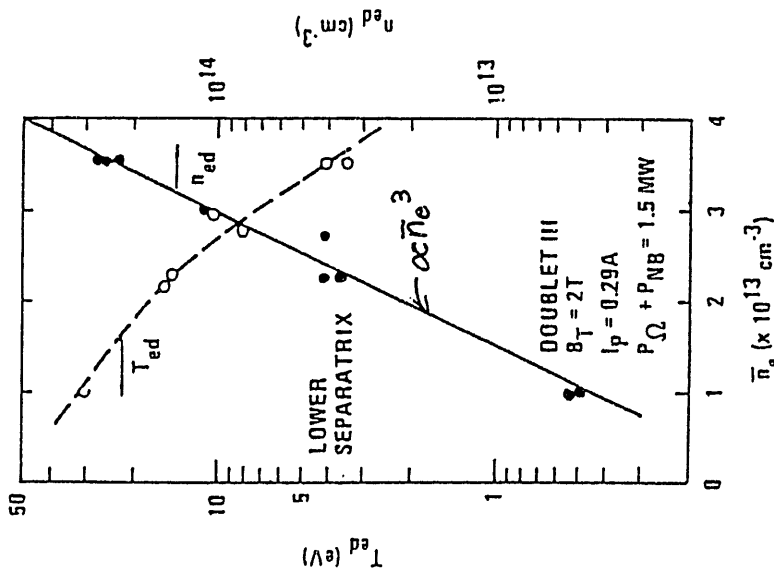


Fig. 4. Electron density, n_{ed} (—●—), and temperature, T_{ed} (—○—), at the peaks of the density profile on the divertor plate as a function of the average electron density of the main plasma \bar{n}_e ($t = 700$ ms).

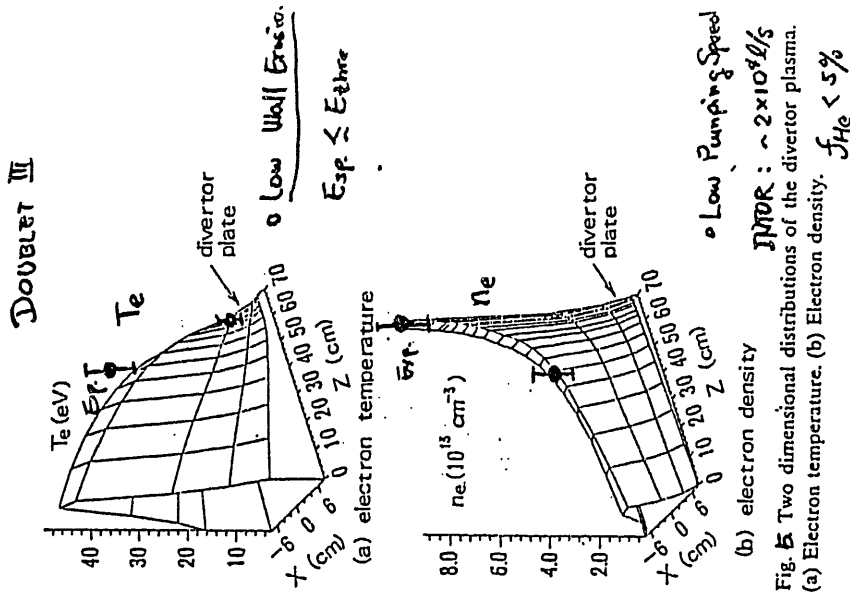


Fig. 5. Two dimensional distributions of the divertor plasma.

(a) Electron temperature. (b) Electron density.

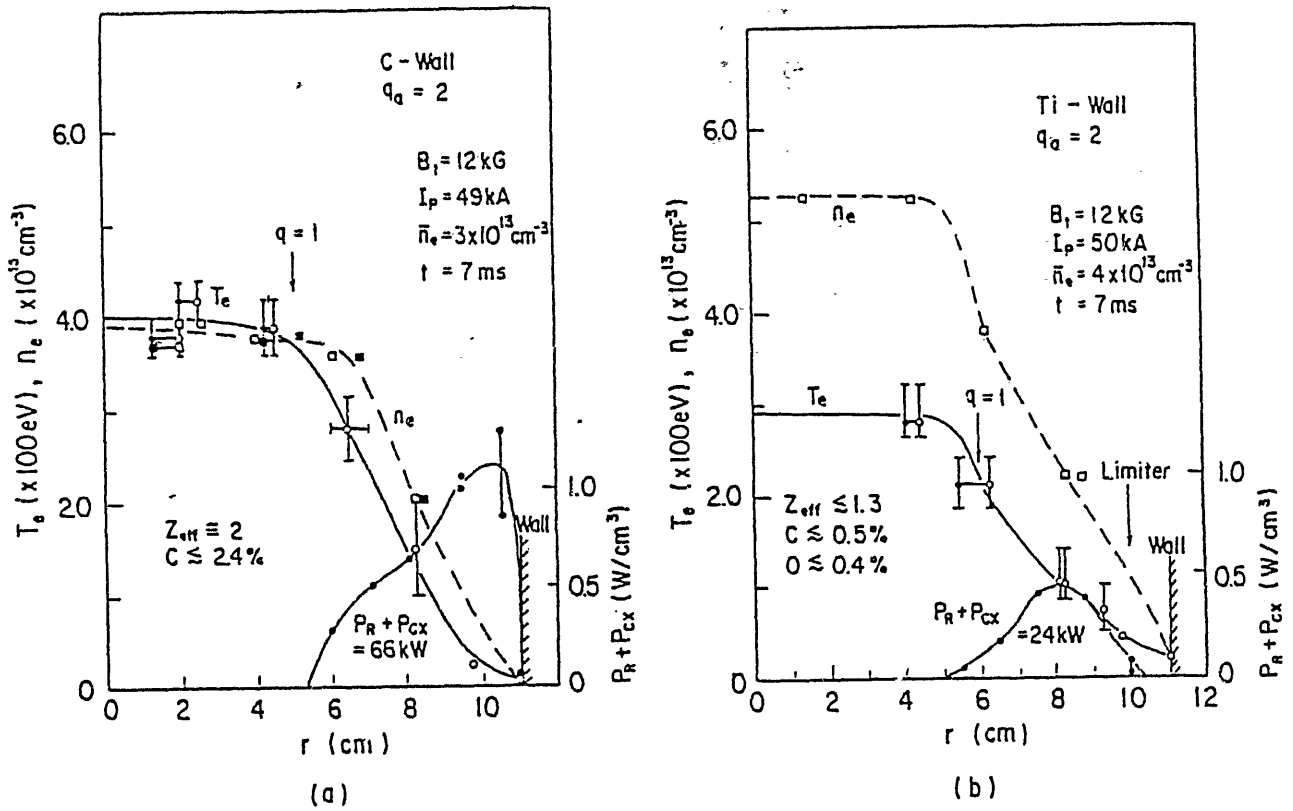


Fig. 6. Spatial distributions of electron temperature (T_e), density (n_e) and radiation and charge exchange loss power (P_R+P_{CX}) for (a) carbon and (b) titanium walls.

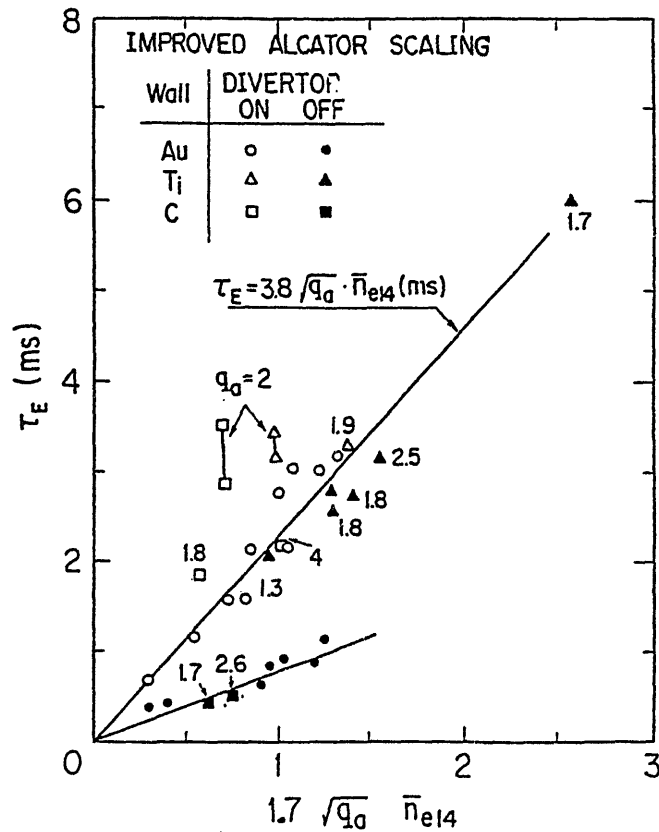


Fig. 7. τ_E vs. $1.7\sqrt{q}\bar{n}_{e14}$, where \bar{n}_e is the line-averaged density in 10^{14} cm^{-3} and τ_E is in ms. Au wall (○, ●), Ti wall (△, ▲) and C wall (□, ■) are investigated with divertor (○, △, □) and without divertor (●, ▲, ■).

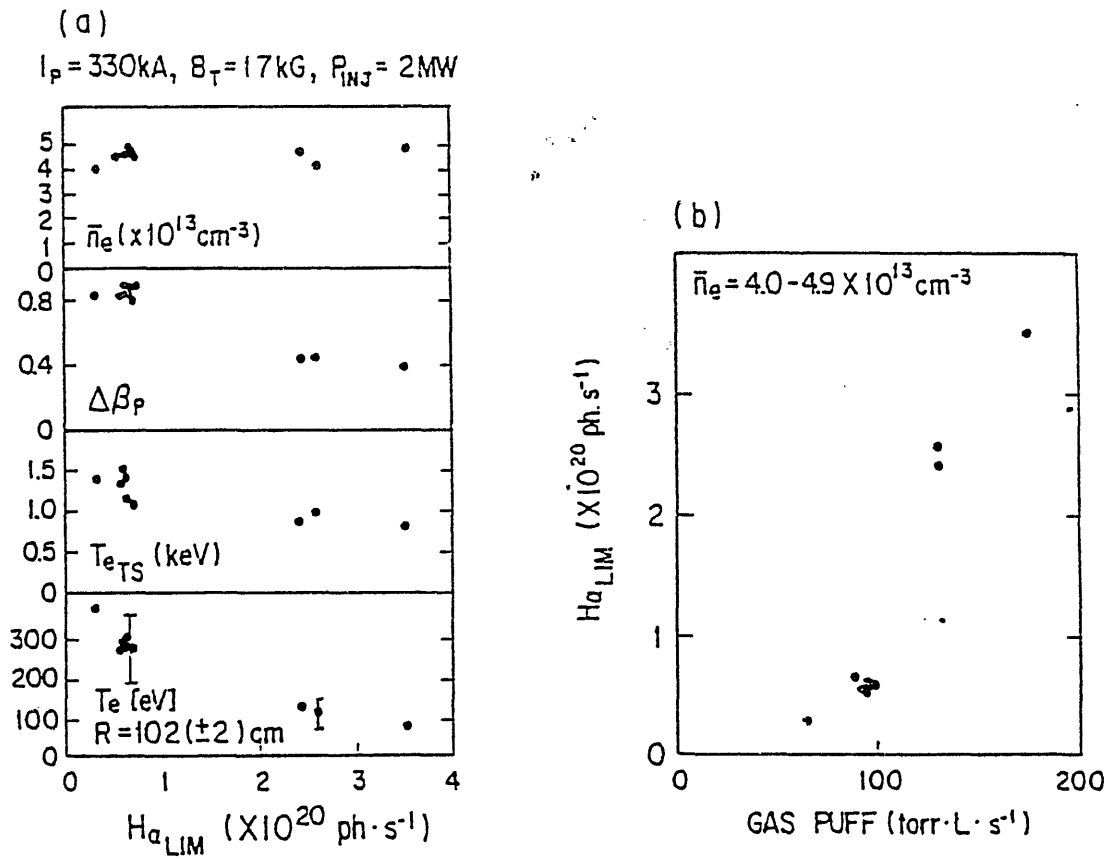


Fig. 8. (a) $\Delta\beta_p$, T_{eTS} , and electron temperature near the main separatrix magnetic surface versus $H_{\alpha LIM}$ for discharges with similar \bar{n}_e [$(4-4.9) \times 10^{13} \text{ cm}^{-3}$]. Only the intensity of the cold-gas puff was changed during the beam injection for these discharges; (b) $H_{\alpha LIM}$ versus gas puff intensity.

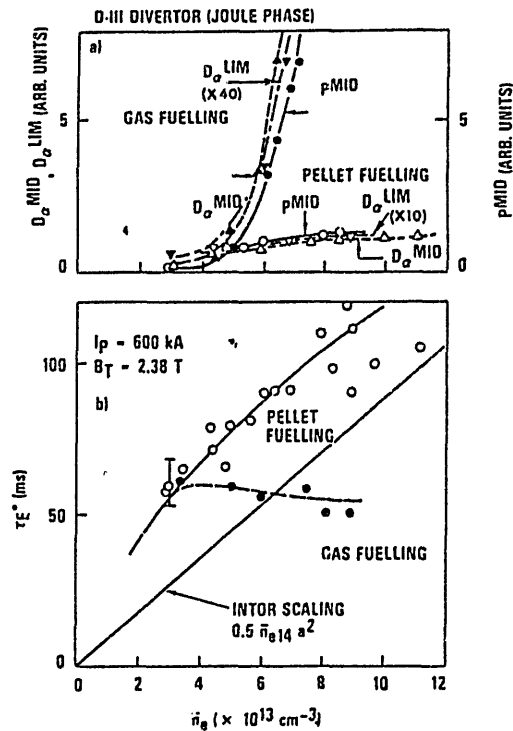


FIG. 9. Comparison of a) particle recycling at limiter and divertor regions as inferred from $D_{\alpha LIM}$ and $D_{\alpha MID}$ and neutral pressure at divertor region and b) the energy confinement time between gas- and pellet-fueled discharges as functions of \bar{n}_e . Open symbols denote pellet-fueled, and solid symbols gas-fueled discharges.

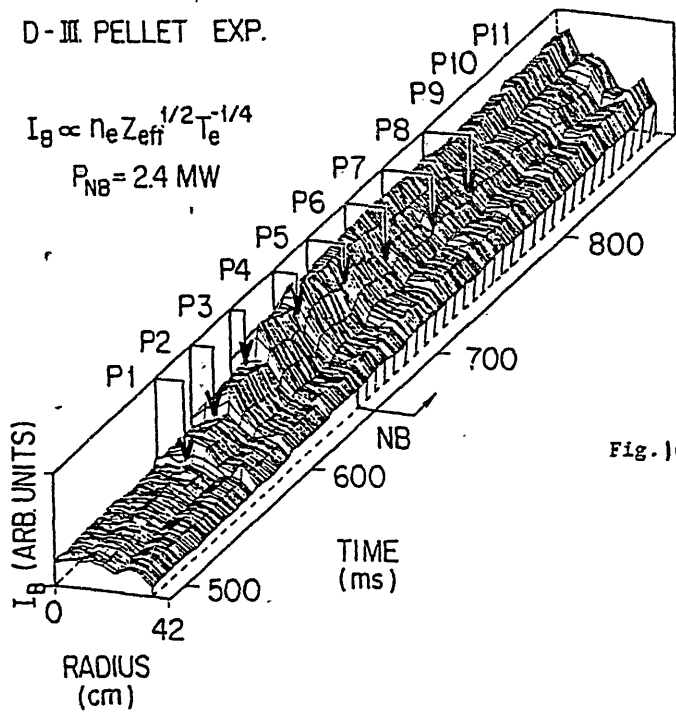


Fig. 10. Temporal and spatial evolution of Abel inverted square root of Bremsstrahlung emission as a relative density profile evolution ($I_B \propto n_e Z_{eff}^{1/2} T_e^{-1/4}$) for the pellet fueled discharge. Signals are filtered by 500 Hz low-pass filter and sliced in every 1 ms. The pellet penetration for pellet numbers 1-8 (P1-P8) are shown by arrows. The neutral beam injection period is shown by the hatched area.

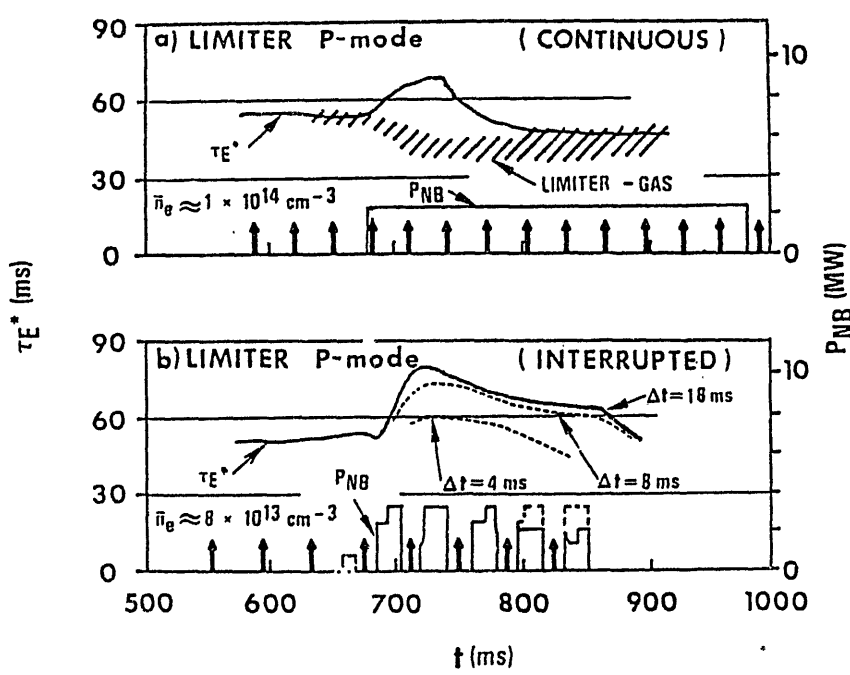


Fig. 11. Comparison of temporal deviation of average energy confinement time for a) continuous beam case and b) interrupted beam case for $\Delta t = 4, 8$ and 18 ms . Pellet injection timings are shown by arrows except for $\Delta t = 4$ and 18 ms .

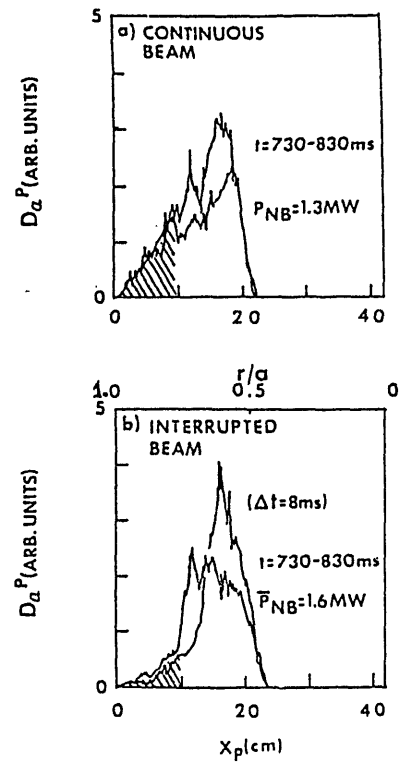


Fig. 12. D_α^P signals coming from pellets to 90° filtered photodiode (D_α^P) as the pellet ablation profiles: a) for continuous 1.3 MW beam heating and b) for interrupted beam heating (averaged beam power of 1.6 MW), in Fig. 11 ($\Delta t = 8 \text{ ms}$). Penetration is measured from the limiter surface, X_p , deduced from measured pellet velocity (800 m/s). Those pellets are injected between $t = 730 \text{ ms}$ and 830 ms in both cases.

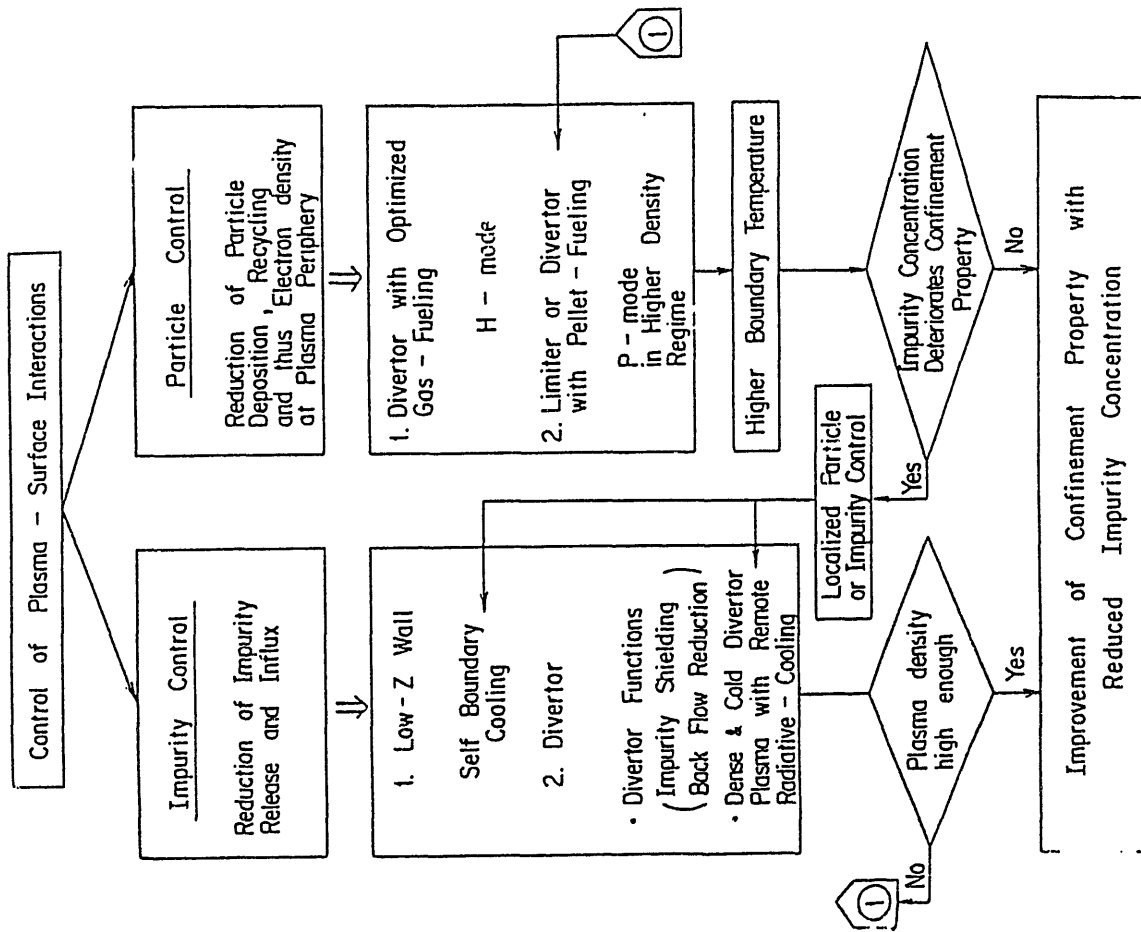


Fig. 14. Control flow-chart of plasma-surface interaction.

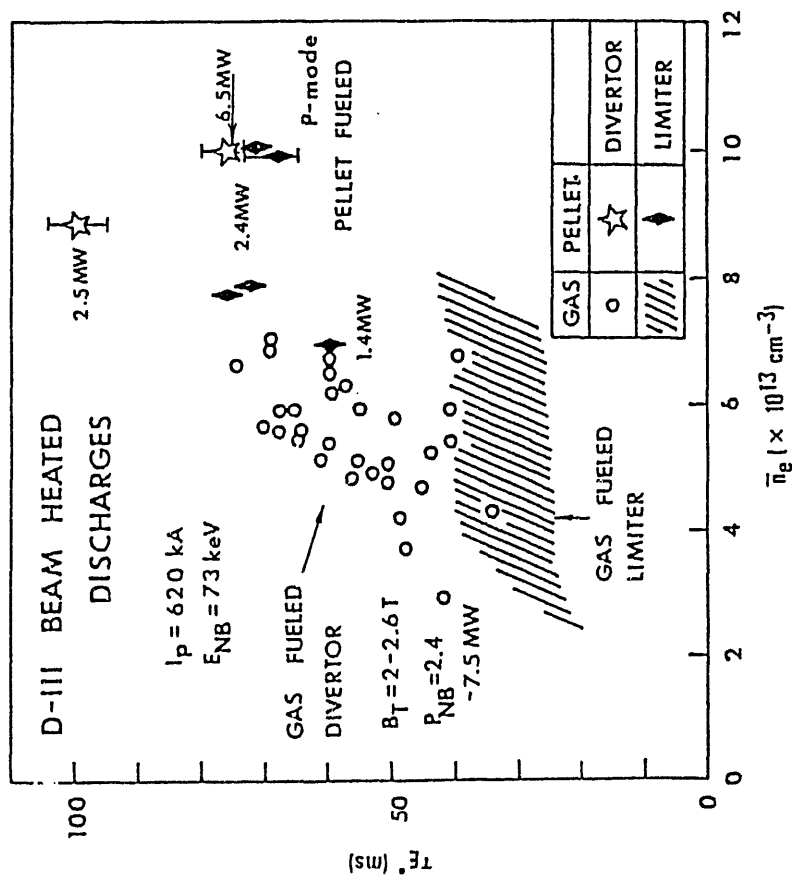


Fig. 13. Comparison of \bar{n}_e , τ_E^* plot between pellet and gas fueled discharges for both limiter and divertor configurations with continuous beams. The upper envelope of open circles corresponds to D-III H-mode discharges. For gas fueled discharges, τ_E^* is calculated when $dW/dt = 0$.

A comment from a plasma spectroscopist --- Ionizing plasma and recombining plasma

Takashi Fujimoto

Department of Engineering Science, Kyoto University, Kyoto 606, Japan

Most generally, a population of an excited ion $n(p)$ immersed in a plasma consists of two components: the contribution which is proportional to the ground-state population $n(1)$ of the ion concerned and that which is proportional to the ion density of the next-ionized stage. If the first contribution is dominant in all of the $n(p)$'s, this situation is called the ionizing phase for the ion species concerned or simply the ionizing plasma. On the other hand, if the second is dominant the plasma is called to be in the recombining phase.¹⁾

Figure 1 shows the "map" of the excited-state populations for the ionizing plasma and the recombining plasma; Griem's boundary divides the low-density regions and the high-density regions, while Byron's boundary divides the low-lying levels and the high-lying levels. The ordinate p is understood to be the principal quantum number of the level, Griem's boundary derives from the dominating depopulation mechanism of levels; for lower density than the boundary or for the lower-lying levels than the boundary level, the dominant depopulation mechanism is the radiative decay, while for the higher density or for the higher-lying levels it is the collisional depopulation. Numerically the critical level is approximated as

$$p_G \simeq 95 (n_e/z)^{7/17}, \quad (1)$$

where n_e is in cm^{-3} and z is the core charge acting on the running electron. Byron's boundary is given from the comparison of the collisional excitation and deexcitation from the level: for levels lying above the boundary the collisional excitation is more probable than deexcitation, while for lower-lying levels the dominant collisional depopulation is deexcitation to still lower-lying levels. The critical level is approximated as

$$p_B \simeq (z^2 R / 3kT_e)^{1/2} \quad (2)$$

where R is one Rydberg (13.6 eV).

Let us consider as an example the Alcator plasma with $T_e \simeq 1.5 \times 10^7$ K and $n_e \simeq 3 \times 10^{14} \text{ cm}^{-3}$ at the center. Argon was mixed as an impurity, and a spectrum of the resonance-series lines ($1^1S - n^1P$) was observed of the helium-like argon (Ar^{16+}).²⁾ The reduced electron density is $n_e/z^7 \simeq 10^6 \text{ cm}^{-3}$, the electron temperature is $T_e/z^2 \simeq 5 \times 10^4$ K, and Griem's boundary is $p_G \simeq 19$. Therefore, the lower-lying levels of $p \lesssim 19$ are expected to be in the corona phase if the plasma is ionizing, while they are in the capture-radiative-cascade phase if the plasma is recombining. Figure 1 shows that the population-density distribution $n(p)/g(p)$ is almost independent of p ($\propto p^{-0.5}$) for both the cases since the reduced temperature is sufficiently high. Thus, the observed intensity distribution of $\propto p^{-3}$ can be ascribed either to the ionizing phase or the recombining phase. Actually the helium-like argon is found to be ionizing or equilibrium at the center, and in the outer regions it is in the recombining phase. Thus, in the central region the emission-line intensities are proportional to the ground-state argon ion density, $n(\text{Ar}^{16+})$, while they are proportional to the hydrogen-like argon density, $n(\text{Ar}^{17+})$ in the outer regions.

The information whether the plasma is ionizing or recombining is derived from the intensity ratio between the singlet resonance line ($1^1S - 2^1P$, denoted as "w") and the triplet lines ($1^1S - 2^3S$, "z", and $1^1S - 2^3P_{1,2}$, "y" and "x"); in the ionizing plasma the ratio $(x+y+z)/w$ is about 1, while in the recombining plasma the ratio is about 3 - 5, depending on the temperature.³⁾

Now let us turn to the neutral hydrogen present in the Alcator plasma. Since T_e is several orders larger than the ionization potential, hydrogen is expected to be in the ionizing plasma phase. Griem's boundary, eq.(1), is $p_G \simeq 2$, and Byron's boundary, eq.(2), is $p_B \ll 2$; then, all of the excited levels $p \gtrsim 2$ are in the saturation phase and the ladder-like excitation mechanism is established among these levels. The sketch of the population flows among the levels is shown in Fig. 2. The population balance is described roughly by

$$n(p-1)C(p-1,p)n_e = n(p)C(p,p+1)n_e = \dots = (\text{independent of } p), \quad (3)$$

where $C(q,p)$ denotes the excitation rate coefficient by electron collisions.

Since the excitation rate coefficient $C(p,p+1)$ is proportional to p^4 the population density is proportional to p^{-4} , or $n(p)/g(p) \propto p^{-6}$. The numerically computed population-density distribution is shown in Fig. 3. For the helium-like argon the enhancement of the populations $n(n^1P)$ with $n = 9$ and 10, and with $20 \lesssim n \lesssim 40$ has been observed in the outer regions and attributed to the charge exchange population from the ground-state hydrogen for the former and the excited-state hydrogen for the latter.²⁾ In analyzing the line intensities from these levels, the excited-state hydrogen populations according to $n(p)/g(p) \propto p^{-6}$ should be taken into account.

It has been shown that the concepts of the ionizing plasma and recombining plasma, and those of the reduced density and temperature are useful in interpreting the plasma spectroscopy data in terms of atomic processes. It is emphasized that the population characteristics in dense plasmas (Figs. 2 and 3) are different from those in low-density plasmas as shown in Figs. 3 and 4. For instance, among the populating mechanisms of a level, say level 5, the direct excitation from the ground state is 80 % in the low-density plasma, while it is only about 2 % in the dense plasma. Figure 5 depicts the characteristics of the populating and depopulating mechanisms for level 5 of ionizing hydrogen: the blank areas denote the collisional transitions and the shaded areas denote the radiative transitions. Percentage contributions from various levels from which level 5 is populated (a), and to which level 5 is depopulated (b) are shown. The corona phase for low densities (Fig. 4) and the ladder-like excitation mechanism (Fig. 2) for high densities are seen, and the transition between these two phases takes place at about n_e at which $p_G = 5$, or $n_e/z^7 \simeq 10^{11} \text{ cm}^{-3}$.

References

- 1) T. Fujimoto, J. Phys. Soc. Jpn. 47, 265 (1979), 47, 273 (1979), 49, 1561 (1981), 49, 1569 (1981), 54, 2905 (1985).
- 2) J.E. Rice, E.S. Marmor, J.L. Terry, E. Källne and J. Källne, (private communication).
- 3) T. Fujimoto and T. Kato, Astrophys. J. 246, 994 (1981).

Figure captions

Fig. 1. "Map" of excited-level populations of ionizing (a), and recombining (b), hydrogen-like ions immersed in a plasma. Griem's boundary and Byron's boundary are given by eqs. (1) and (2), respectively. For each phase name, [population mechanism] with its sketch, and population-density distribution are given. In the CRC phase of the recombining plasma $n(p)/g(p) \propto p^{-0.5}$ if T_e/z^2 is high.

Fig. 2. Dominant flows of electrons in the energy-level diagram, for $n_e/z^7 = 10^{16} \text{ cm}^{-3}$ and $T_e/z^2 = 1.28 \times 10^5 \text{ K}$ (of neutral hydrogen). "c" denotes the continuum state. The width of an arrow indicates the magnitude of the flow. Flows to and from level 5 are given in some detail. The net ionization flow, $S_{CR} n(1) n_e$, is given on the right. All of the transitions except for that from $p = 2$ to $p = 1$ are collisional. The ladder-like excitation mechanism is established over all of the levels.

Fig. 3. The population-density distribution over the excited levels of hydrogen for several values of n_e/z^7 . T_e/z^2 is $1.28 \times 10^5 \text{ K}$ and $n(1) = 1 \times 10^{16} \text{ cm}^{-3}$ is assumed. Griem's boundary, eq. (1), for the transition between the corona and saturation phases is given by the dash-dotted line.

Fig. 4. Dominant flows of electrons in the energy-level diagram of hydrogen for $n_e/z^7 = 10^6 \text{ cm}^{-3}$ and $T_e/z^2 = 1.28 \times 10^5 \text{ K}$. The hatched arrows indicate radiative transitions. Flows to and from the level $p = 5$ are given in some detail. All of the excited levels are in the corona phase.

Fig. 5. Percentage contributions from various processes to (a) populating to, (b) depopulating from, the level $p = 5$ as a function of $n_e/z^7 \text{ (cm}^{-3}\text{)}$. The hatched areas correspond to radiative transitions. "S" denotes ionization.

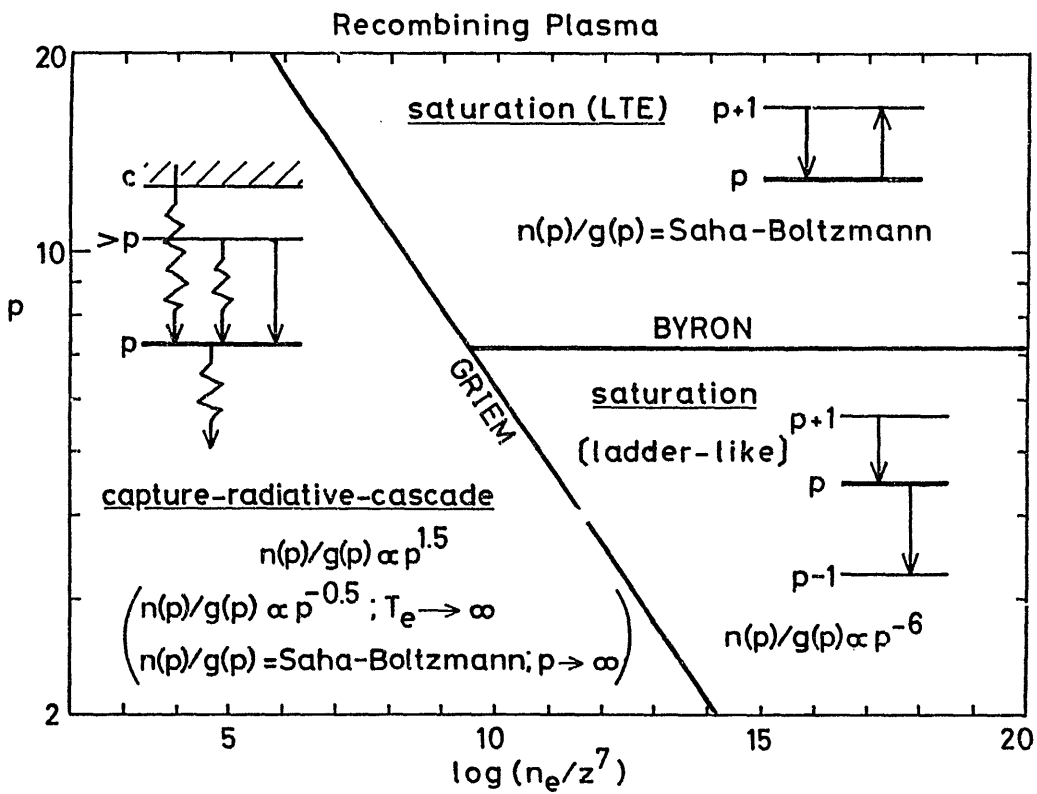
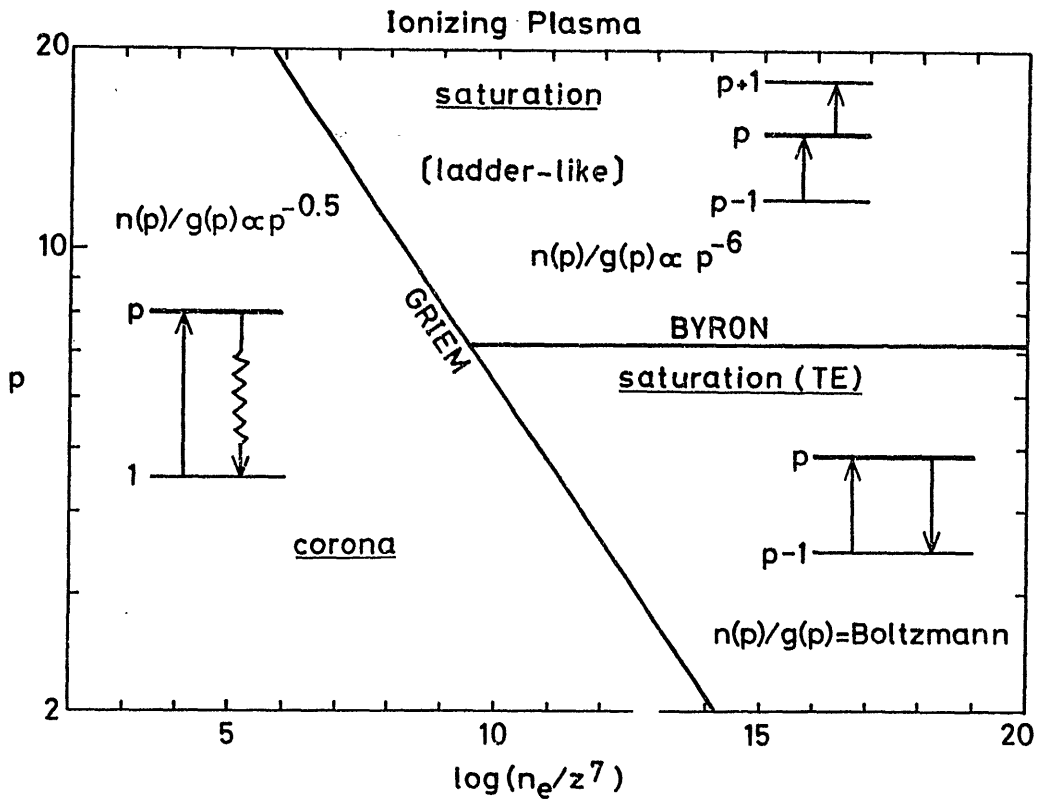


Fig. 1

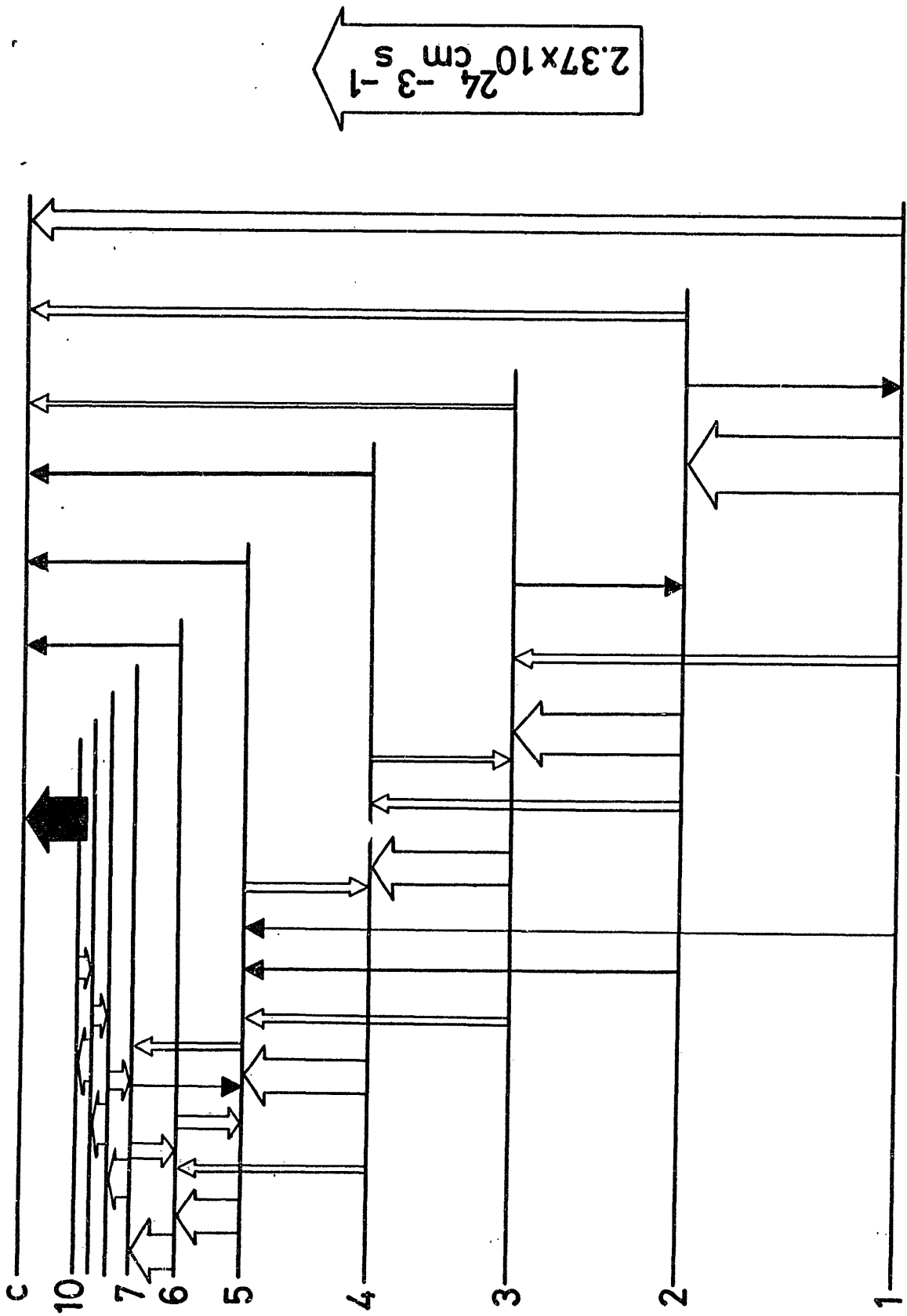


Fig. 2

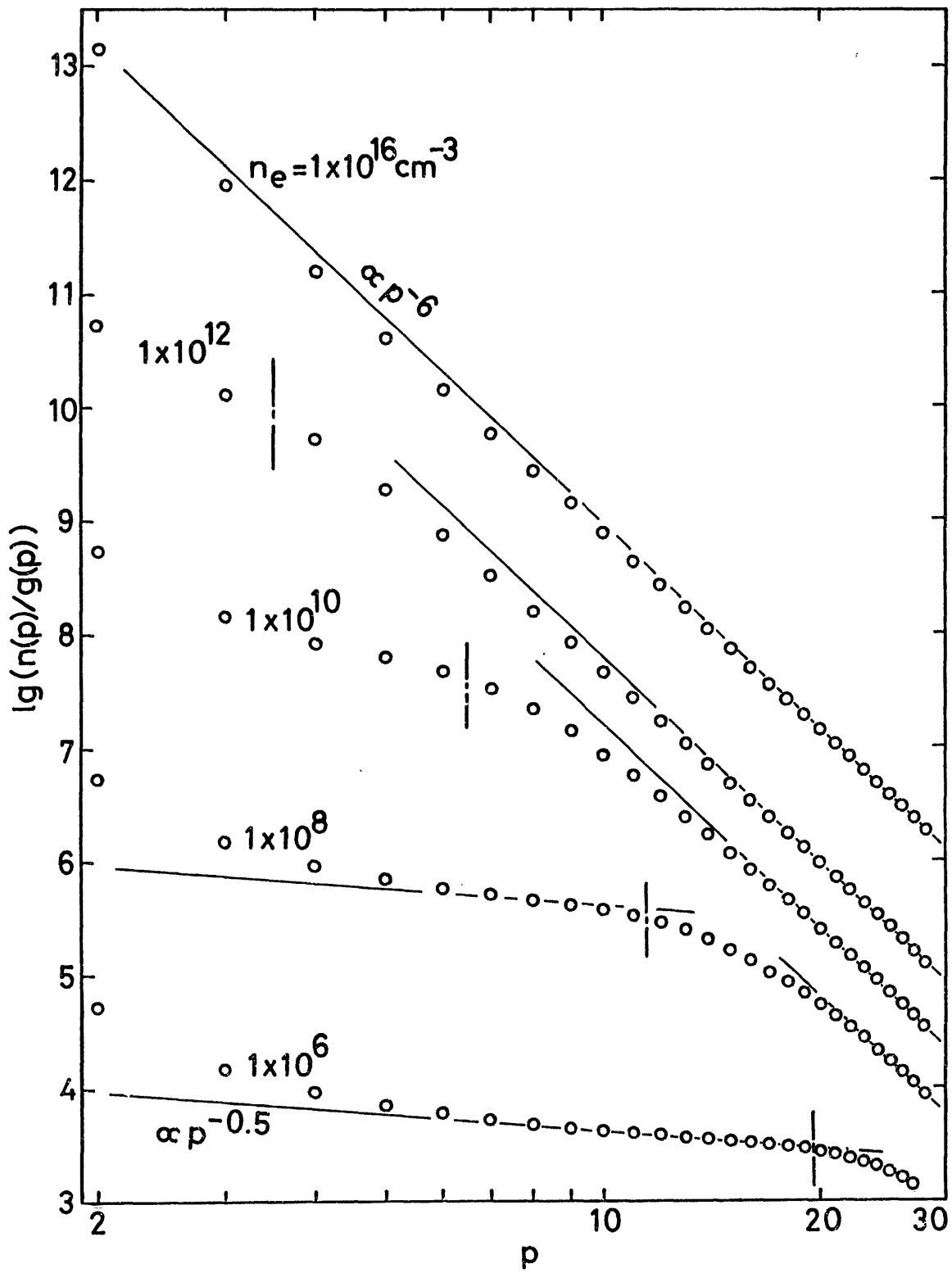


Fig. 3

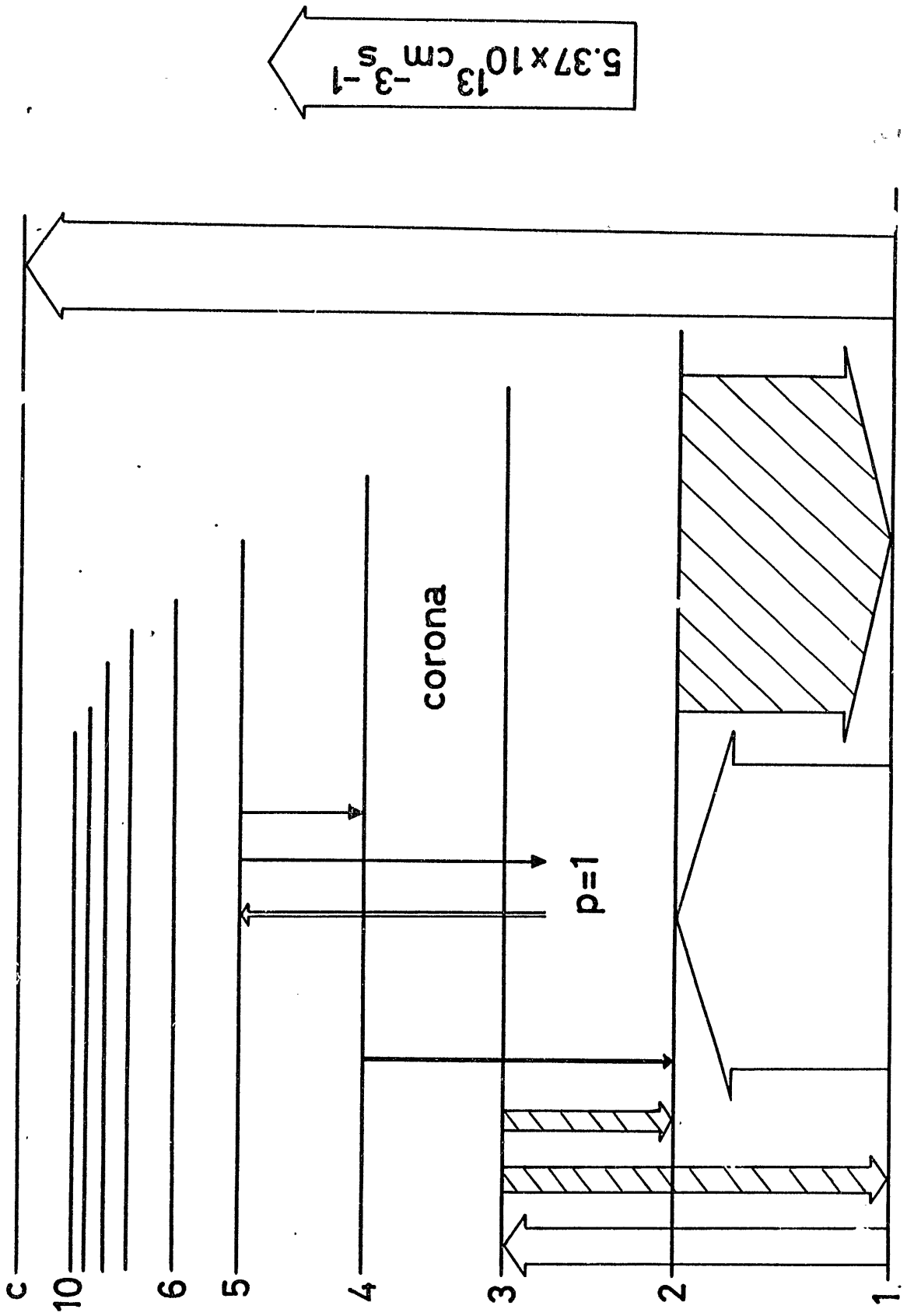


Fig. 4

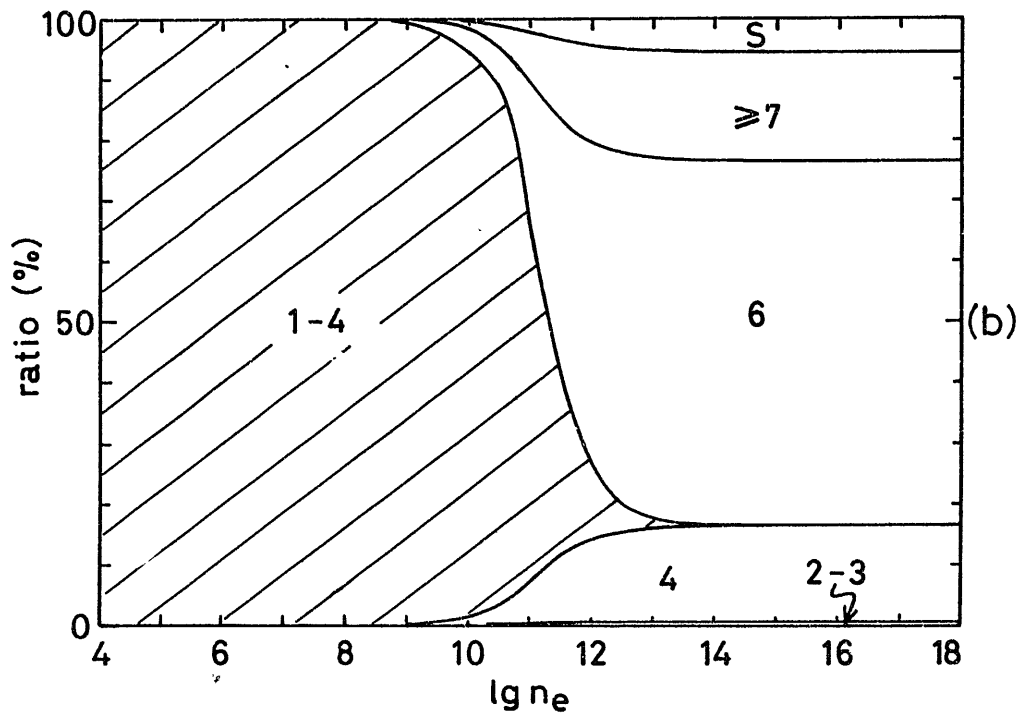
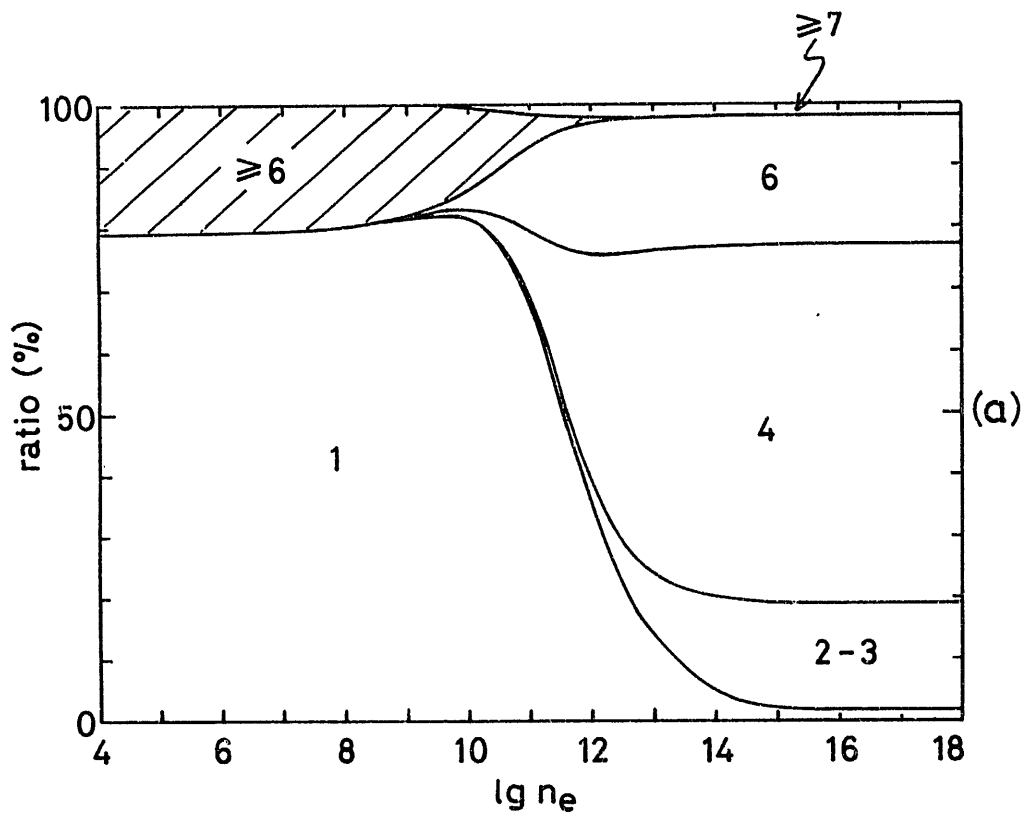


Fig. 5

Effects of Accuracy of Atomic Data on Tokamak Impurity Transport Modelling⁺

Takaichi KAWAMURA, Tadayoshi ONO* and Akira MIYAHARA
Institute of Plasma Physics, Nagoya University
Nagoya 464, Japan

Abstract

The effects of accuracy of atomic data on the impurity transport modelling based on a one-dimensional tokamak model are discussed. As an example the difference between the results using two different formulas for the dielectronic recombination rate coefficients is analyzed, and it is concluded that in order to draw out reliable evidence of anomalous impurity transport considerably accurate atomic data should be needed.

§1. Introduction

Plasma modellings are widely recognized as a procedure necessary for analyses of experimental results obtained from existing machines as well as for the design and operation of new devices. A plasma modelling includes theoretical calculations and numerical simulations, where knowledge on atomic processes is indispensable in addition to the characteristic parameters of a plasma concerned. Especially many kinds of atomic processes should be taken into consideration for the calculations of impurity transport in plasma. Therefore, in view of a plasma modelling, it is very important to know how the accuracy of a reaction rate of each atomic process has an effect on the modelling results, from which we want to determine the experimental evidence of anomalous impurity transport.

In this paper we will report the results obtained from impurity transport analysis using a one-dimensional tokamak model, in which the anomalous diffusion and convection of impurities in host hydrogen plasma in

+ Presented at Advisory Group Meeting on Atomic and Molecular Data for Fusion Plasma Modelling, IAEA, Vienna, 18-20 September 1985.

* Permanent Address: Department of Physics, Nagoya University

steady state are assumed, and we will point out remarkable effects of the difference of the reaction rate data on the radial impurity distributions. The tokamak parameters adopted here are taken as those of JIPPT-IIU in IPP-Nagoya (torus major radius $R = 91$ cm, plasma minor radius $a = 22$ cm). Iron (Fe) is assumed as a representative impurity species. The computer code used here is basically developed by T. Amano.¹⁾

§2. Model of Impurity Transport

The impurity transport in a one-dimensional tokamak model is described by the following equations:

$$\frac{\partial n_k}{\partial t} = -\frac{1}{r} \frac{\partial}{\partial r} (r \Gamma_k) + I_k \quad (1)$$

where $n_k(r, t)$ is the radial density distribution of impurities of an ionization state k ($k = 1$ for neutrals) and I_k is a term which includes the ionization and recombination coefficients as

$$I_k = -n_e n_k (S_k + \alpha_{k-1}) + n_e n_{k-1} S_{k-1} + n_e n_{k+1} \alpha_k \quad (2)$$

where n_e is the electron density, S_k is the ionization rate coefficient ($k \rightarrow k+1$) and α_k is the recombination rate coefficient ($k+1 \rightarrow k$). The radial impurity flux Γ_k in eq.(1) is

$$\Gamma_k = -D_k \frac{\partial n_k}{\partial r} - V_k n_k \quad (3)$$

where D_k is the diffusion constant and V_k is the radial inward convection velocity. The diffusion constant of impurities D_k is given by

$$D_k = D_k^{nc} + D_A \quad (4)$$

where D_k^{nc} is the neoclassical term and D_A is the anomalous diffusion constant. The radial convection velocity V_k is taken as

$$V_k = V_k^E + \frac{r}{a} V_A \quad (5)$$

where v_k^E is the radial velocity due to the pinch effect caused by tokamak plasma current, and rV_A/a is the phenomenological anomalous convection velocity. In this study D_A and V_A are treated as free parameters which are given identical values for all charge states of the impurity ions.

In the following analysis we assume the stationary density and temperature profiles of the hydrogen plasma such as $n_e(r) = (n_c - n_w) (1 - r^2/a^2) + n_w$, $n_c = 1 \times 10^{14} \text{ cm}^{-3}$, $n_w = 5 \times 10^{12} \text{ cm}^{-3}$, $T_e(r) = (T_{ec} - T_{ew}) (1 - r^2/a^2) + T_{ew}$, $T_{ec} = 1000 \text{ eV}$, $T_{ew} = 30 \text{ eV}$ and only the impurity equations eq(1) ($k = 2, 3, \dots, 27$ for Fe) are numerically solved. The neutral impurity distribution $n_I(r)$ is assumed to have a form of

$$n_I(r) = (\Gamma_I(a) / v_I) \exp \left\{ - \frac{1}{v_I} \int_a^r dr n_e(r) S_I \right\} \quad (6)$$

where v_I is the thermal velocity of neutrals ($= 10 \text{ eV}$) and S_I is the ionization rate coefficient. The neutral impurity flux at the plasma boundary is taken as $\Gamma_I(a) = - \sum_{k>2} \Gamma_k(a)$ where the recycling coefficient is unity. The steady distribution of the impurity ions should be attained at a time sufficiently long compared with impurity confinement time ($\sim a^2/2D$) after the start of calculation, therefore we have examined here only the distributions at $t = 75 \text{ msec}$ after the start in the following analysis, where the particle confinement time for JIPPT-IIU is about 20 msec.

§3. Radial Impurity Distribution

In a static plasma the shape of the radial distribution of the impurities of each charge state, $n_k(r)$, may be decided by the electron temperature profile $T_e(r)$. However, the transport process of impurities modifies a radial distribution in such a manner as the diffusion may spread the width and as the convection may shift the maximum position.

The full width at half maximum d_k of the distribution of the k -th ionization state is approximately expressed as

$$\begin{aligned} d_k &= \sqrt{(d_k^T)^2 + (d_k^D)^2} \\ &\cong \sqrt{(d_k^T)^2 + 16 \ln 2 \cdot D_k t_k} \end{aligned} \quad (7)$$

where d_k^T is the width caused by a temperature profile and d_k^D is the one due to radial diffusion. The latter is determined by the diffusion constant D_k and the mean life-time t_k between creation and annihilation of an ion of the k -th ionization state which is estimated as $t_k = (n_e S_k)^{-1}$. In Eq.(7) it is worth while to point out that d_k^T depends on both of ionization and recombination while d_k^D depends principally on a ionization rate coefficient. The radial convection affects a mutual spacing, l_{kk} , between maximum positions of the distributions of the different charge states, k and k' . A maximum position of the distribution is also related to the competition between ionization and recombination. Then it is interesting to study how the accuracy of the data on ionization and recombination rate coefficients affects the characteristic parameters of impurity distribution such as d_k and l_{kk} .

§4. Rate Coefficients of Atomic Processes

We can calculate impurity distributions using various different rate coefficients in our computer code. However, as an example, we here report the effects of different dielectronic recombination rate coefficients because the dielectronic recombination has a leading effect on recombination process in the region of electron temperature concerned.

As a standard case our modelling code includes ionization and recombination rate coefficients which are prepared by Post et al.²⁾, where the ionization rate coefficients are electron impact ionization rates combined by them referring to Lotz³⁾ and others and the recombination rate coefficients are the sum of radiative recombination rates given by Seaton⁴⁾ and the dielectronic recombination rates in the basic scheme of Burgess⁵⁾.

In this report we have used another dielectronic recombination rate formula given by Shull & Van Steenberg⁶⁾ which is based on the empirical formula proposed by Aldrovandi and Pequignot⁷⁾. We have compared the calculated results of impurity (Fe) distributions using the above two different subroutines for dielectronic recombination rate coefficients when the anomalous diffusion and convection are taken into account. In the following we refer to the computation using standard data as Case A and to the case as Case B when only the dielectronic recombination rate coefficients are replaced by the ones given by Shull and Van Steenberg.

§5. Results and Discussions

For example we present the results of computations for the case when $D_A = 5 \times 10^3 \text{ cm}^2 \text{ sec}^{-1}$ and $V_A = 300 \text{ cm sec}^{-1}$ in Fig.1 and Fig.2. Fig.1a shows the result using standard data (the dielectronic recombination rate coefficients in the form by Burgess) and Fig.1b displays the one in which only the dielectronic recombination rate coefficients are replaced by the new ones shown by Shull and Van Steenberg. In Fig.2a and 2b we illustrate the differences between the two cases about the FeXVI and FeXVII distributions, respectively. From these results we can deduce strong dependence of distributions on the difference between the cases of different dielectronic recombination data.

In Fig.3 we plot the full widths at half maximum versus different D_A values ($V_A = 0$ is assumed) to clarify the difference between the two cases. These results show the fact that the change of d_k in the wide range of D_A values is buried under the change due to the different dielectronic recombination formulas. But the results in the two cases agree with each other for sufficiently large values of D_A , therefore, the qualitative tendency given by Eq.(7) seems to be confirmed, because we have here used same ionization rate coefficients S_k in the two cases.

The peak spacing, l_{kk} , between the radial distributions of different charge states should be related to convection velocity. In Fig.4, we illustrate the relation between the spacings $l_{IX, XIV}$ versus V_A ($D_A = 0$ is assumed) in the above two cases with the different dielectronic recombination data. This shows that the discrepancy due to the different dielectronic recombination data becomes larger for large V_A values.

The anomalous impurity transport is a very important problem in the nuclear fusion researches because it is related to radiation loss from the core plasma as well as plasma edge cooling. However, our results show that considerably accurate atomic data should be needed in order to draw out reliable values of anomalous impurity transport coefficients from the plasma modelling researches.

The authors are grateful to Prof. S. Hayakawa for his useful suggestions and also to Prof. T. Amano for his advices on a computer code. The computation has been performed at the Computer Center of the Institute of Plasma Physics, Nagoya University and we thank Dr. Y. Abe and the members of the Computer Center for their contributions to the code development and computation.

References

- 1) T. Amano, J. Mizuno and M. Kako, Research Report of Institute of Plasma Physics, Nagoya, IPPJ-616 Nov. 1982.
- 2) D. E. Post, R. V. Jensen, C. B. Tarter, W. H. Grasberger and W. A. Lokke, Atomic Data and Nuclear Data Tables, 20 (1977) 397.
- 3) W. Lotz, Astrophys. J. Suppl. 14 (1967) 207.
- 4) M. Seaton, Mon. Not. Roy. Astron. Soc., 119 (1959) 81.
- 5) A. Burgess, Astrophys. J. 141 (1965) 1588.
A. L. Mertz, R. D. Cowan and N. A. Magee, LASL Report, LA-6220-MS, Los Alamos (1976).
- 6) J. M. Shull and M. Van Steenberg, Astrophys. J. Suppl., 48 (1982) 95.
- 7) S. M. V. Aldrovandi and D. Pequignot, Astron. Astrophys. 25 (1973) 137.

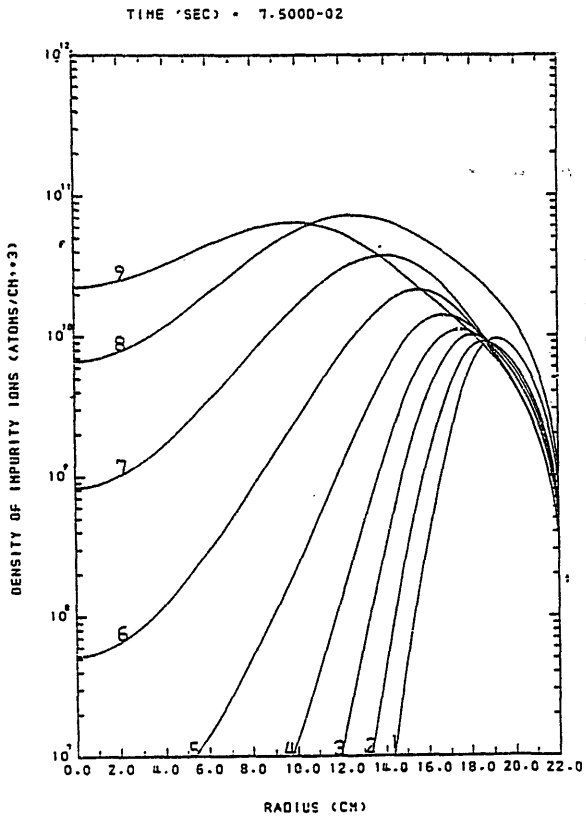
Figure Captions

- Fig.1 a) The radial distribution for FeK ($K = X \sim XVIII$) computed using the standard data²⁾ in which the dielectronic recombination rate coefficients are given in the form of Burgess. (Case A)
b) The results using the data in which only the dielectronic recombination rate coefficients are replaced by the rate coefficients given by Shull and Van Steenberg⁶⁾. (Case B)

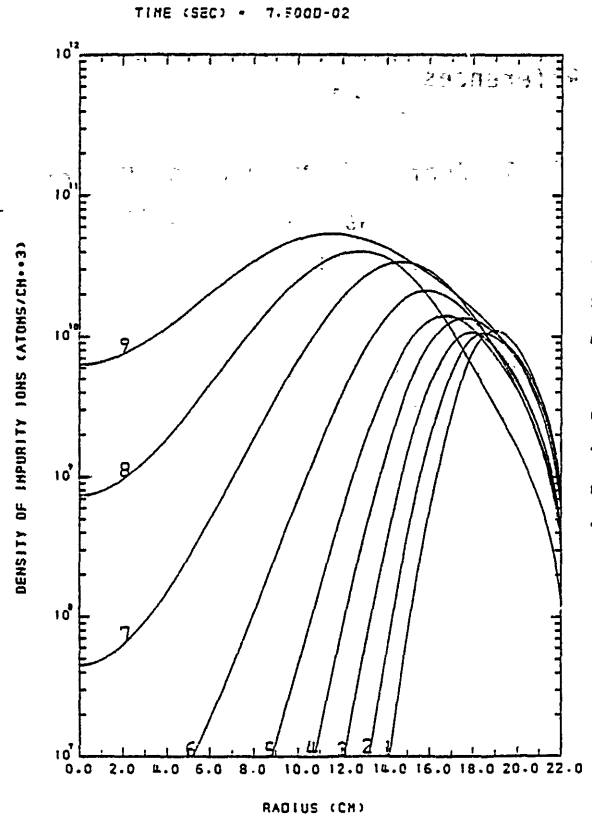
Fig.2 The comparison of Case A with Case B in Fig.1 for FeXVI (a) and FeXVII (b).

Fig.3 The full width at half maximum for FeXV plotted versus anomalous diffusion constant D_A ($V_A = 0$). \odot corresponds to Case A and \triangle to Case B in Fig.1.

Fig.4 The radial spacing between the peaks of distributions for FeIX and FeXIV plotted versus anomalous convection velocity constant V_A ($D_A = 0$). \odot corresponds to Case A and \triangle to Case B.

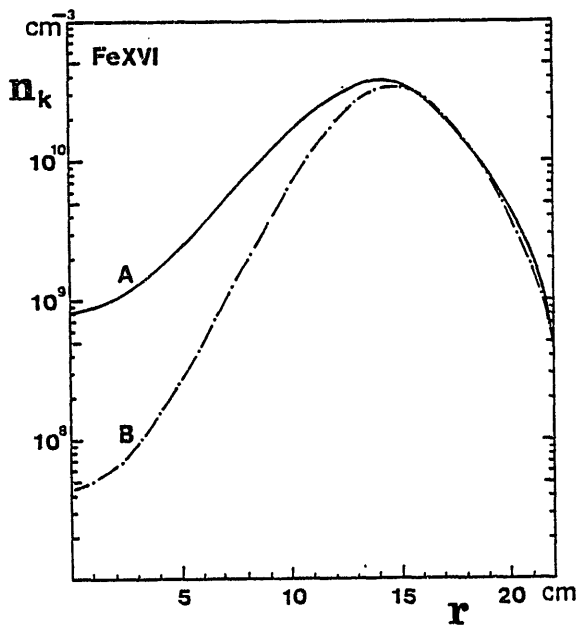


(a)

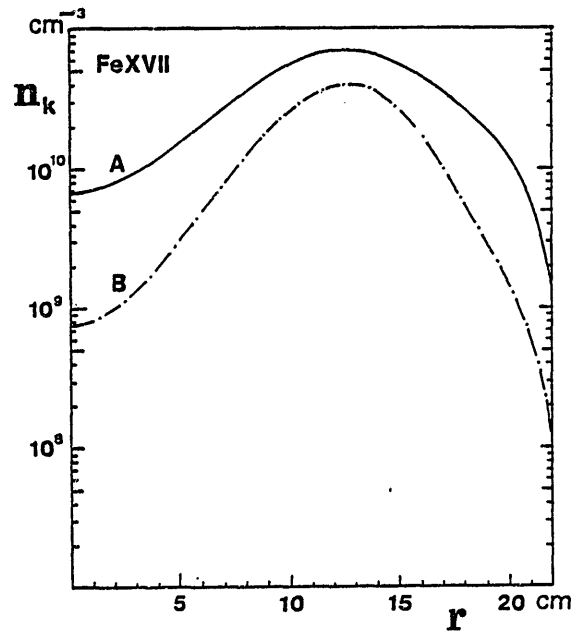


(b)

Fig. 1



(a)



(b)

Fig. 2

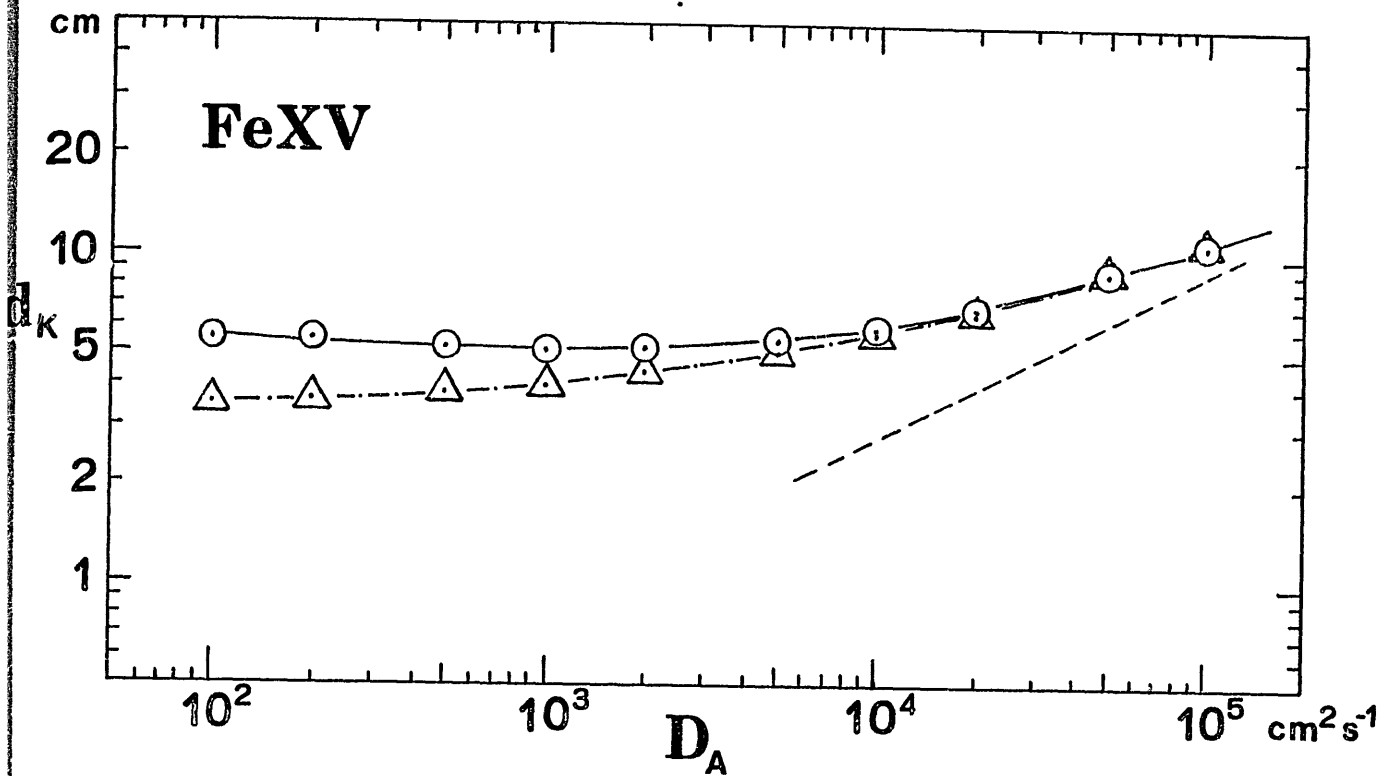


Fig. 3

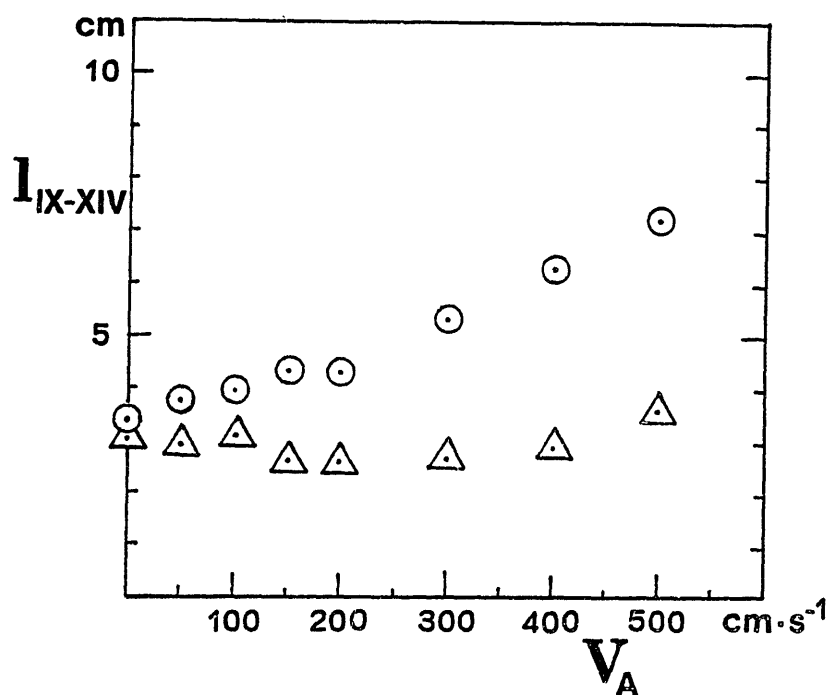


Fig. 4

Multistep ionization and K-shell ionization

for Plasma Modelling of Tokamaks

T. KATO and T. FUJIMOTO*

Institute of Plasma Physics, Nagoya University, Nagoya,

* Department of Engineering Science, Kyoto University, Kyoto,

Japan.

Among various atomic processes which take part in plasma modelling, the ionization process is very important to determine the distribution of ionic states and the radiation loss for energy balance. We describe here the effect of multistep ionization and K-shell ionization on the ion abundances and the rate of radiation loss necessary for plasma modelling of Tokamaks.

There are several ionization processes :

- a) direct ionization
 - b) excitation autoionization
 - c) ionization autoionization
 - d) inner-shell ionization
 - e) ionization from excited states
 - f) multistep ionization
- } K-shell ionization

a) and b) play major roles in any plasma and have been studied more extensively than the other processes. We would like to remark that the contributions of c) - f) on Tokamak plasmas become as important as those of a) and b) under some conditions, though they have been less studied so far.

1) Multistep ionization

i) Ion abundance

The mechanism of the multistep ionization has been discussed in several papers¹⁾ as the ladder like excitation-ionization process in the ionizing plasma.

The multistep ionization is effective when the rate for the collisional de-populating process is larger than the spontaneous transition probability $A_r(n, m)$. This process makes the collisional radiative ionization rate S_{CR} large because the stepwise excitation-ionization become dominant.

The critical level n_t for the collisional process $\sum_m C(n_t, m) n_e \geq \sum_1 A_r(n_t, 1)$ is given for hydrogenic ions as 1)

$$n_t = (1.8 \times 10^{17} Z^6 T^{1/2} (\text{eV}) / n_e (\text{cm}^{-3}))^{2/17} \quad (1)$$

For ions with the ground state with the principle quantum number $n_0 = 2$, $\sum_1 A_r(n, 1) \propto n^{-3.1}$ for $n < 6$ in contrast to $\sum_1 A_r(n, 1) \propto n^{-4.5}$ which is derived for hydrogenic ions.

The error of applying the hydrogenic approximation for determining the value n_t for L-shell ions is estimated to be small.

The ionization potential of the level n_t can be calculated using the hydrogenic approximation,

$$I_t = z^2 I_H / n_t^2 \quad (2)$$

Then the effective ionization energy I'_z for the ion of charge z can be given as :

$$I'_z = I_z - I_t, \quad (3)$$

where I_z is the ionization potential at low density limit. We calculate the collisional radiative ionization rate S_{CR} with the use of Lotz formula²⁾.

$$S_{CR} = 6.7 \times 10^7 \sum_{j=1}^n \frac{a_j \xi_j}{T_e^{3/2} (\text{eV})} \frac{1}{X_j} E_1(X_j) \quad (4)$$

Where T_e is the electron temperature, ξ_j is the number of the equivalent electron of j-the shell,

$$X_j = I'_{zj}/k T_e, \quad a_j = 4.5 \times 10^{-14} \text{ and}$$

$$E_1(X) = \int_x^\infty \exp(-t)/t dt.$$

$$S_{CR} = C_R \quad (5)$$

is assumed for the value of $n_t < 2$, where C_R is the excitation rate coefficient of the resonance line.

We have studied the multistep ionization for oxygen ions in a Tokamak plasma. The collisional radiative ionization rate coefficient S_{CR} are shown in Fig.1 for several degree of ions with a function of density. This process is important for low ionized ions. S_{CR} increases at $n_e > 10^{13} \text{ cm}^{-3}$ as seen in Fig.1. In Fig.2, the calculated spatial distributions of neutral oxygen and ions in a Tokamak are shown. The solid line indicates the result with the multistep ionization included, the dashed line shows the result without multistep ionization. The spatial distribution of the electron density n_e and electron temperature T_e were taken as JIPPT-II Tokamak which is shown in Fig.3²⁾. For Fe ions,

this effect would be more significant than for O ions, because the excitation energies of low ionized Fe ions are smaller. This process is particularly important for the low ionized ions which have small excitation energies in a periphery region. The existence of the metastable states also changes the distributions ³⁾. In our calculation, important excited states of n=2 are also included.

ii) Recombination rate

Generally in a Tokamak plasma, impurity ions are in an ionizing phase. So the recombination process is not so important for attaining an ionization state. The role of recombination becomes important in the case where highly ionized ions produced in a plasma center diffuse out to periphery where the electron temperature is low, or they stay long near the plasma center where the diffusion is slow and the ionization is almost in equilibrium.

The dielectronic recombination is important in high temperature plasmas, compared to the radiative recombination and this is affected very much by the collisional process in highly excited levels, because electrons are often captured in highly excited levels. The rate decreases due to the density effect.

Post et al ³⁾ gave the empirical formulae for the density effect of the dielectronic recombination based on the data

of Ca⁺¹) and He-like ions⁵⁾. These formulae give too large suppression especially for $\Delta n=0$ transitions. Summers⁶⁾ has calculated the ion abundances for a large number of elements using the collisional radiative model, and shown S_{CR} and α_{CR} in graphs in his paper. On the other hand, Jacobs et al⁴⁾ calculated the dielectronic recombination rate coefficient α_d including the autoionization to excited levels at low density limit. We compare the dielectronic recombination rates by Summers and Jacobs for MgX in Fig.4. A very large discrepancy is found especially in high temperature ranges. We calculated the suppression of α_d for $n_e = 10^{16} \text{ cm}^{-3}$ by the use of Post³⁾'s formula and compared with the Summer's calculation. The value by Post's formula is one order of magnitude smaller than that by Summers. There is obviously more to investigate about α_d . α_d for H and He-like high Z elements are smaller than the radiative recombination rates α_r , where α_d is much larger than α_r for L-shell ions.

iii) Radiation Loss

The radiation loss by impurities are one of the most serious energy loss in Tokamak plasmas. The radiation loss including the multistep ionization L_{CR} is studied for an ionizing plasma of hydrogen. L_{CR} is given as

$$L_{CR} = \sum_p \sum_g n(p) A(p,g) \Delta E (p,g) \quad (5)$$

Where $A(p,g)$ is the transition probability and ΔE is the energy between the level p and g .

The ionization loss I_{CR} is expressed as

$$I_{CR} = S_{CR} n(l) n_e \text{ Ryd.} \quad (6)$$

I_{CR} increases as the density increases, whereas the radiation loss decreases due to the decrease of the population density of highly excited states by multistep ionization. The total energy loss by both radiation and ionization $(L_{CR} + I_{CR})/n_e n(l)$ is shown in Fig.5. The total energy loss does not change so much for the increase of the electron density. The radiation loss L_{CR} decreases very rapidly at $n_e > 10^{14} \text{ cm}^{-3}$. When the temperature is low, L_{CR} is much higher than I_{CR} at low densities, but I_{CR} increases steeply until the same level of L_{CR} at high densities. The total energy loss is nearly constant at any densities.

When the plasma is in the equilibrium or recombining phase, the contribution from the ions of the next-ionized stage should be included.

2) K-shell ionization

i) ionization autoionization

This process results in the double ionization through autoionization :

ii) Suprathermal electrons

We don't know how strong are superthermal electrons in a Tokamak plasma. We have tried to see the effect of K-shell ionization by suprathermal electrons. As the ionization rate coefficient of L-shell is more than one order of magnitude larger than that of K-shell, the effect on the L-shell ion distribution would be very small. In Fig.7, is shown the contribution of suprathermal electron of 30 KeV for the assumed density of $0.1 \times n_e(r)$. The effect of double ionization caused by K-shell ionization is negligibly small. Only the small increase of ionization by suprathermal electron for OVII appears.

iii) K - X rays

The K-shell ionization processes followed by radiative decays produce fluorescent K-lines for the ions with L-shell electrons. The fluorescent yield for oxygen ions is very small ($\omega_k \sim 0.007$), and the contribution to the radiation loss is expected negligible. For iron ions, $\omega_k \sim 0.3$, but still ineffective since the direct excitation rate is about two orders of magnitude larger than that of the K-shell ionization rate as seen in Fig.6.

But the K-shell ionization process of the Li-like ions is different from others. The process $1s^2 2s + e \rightarrow 1s 2s$ ($^1, ^3S$) + $2e$ increases the population of the metastable states $1s 2s$ (3S) state from the ground state of the He-like

ions is not large due to the spin exchange transition, whereas the K-shell ionization rate is sufficiently large. From Fig.6, we can see the K-shell ionization rate is almost the same as that for the excitation rate of resonance in the high temperature range. The forbidden line intensity $1s2s$ (3S) - $1s^2(^1S)$ considerably increases by the K-shell ionization of Li-like ions, and accordingly the radiation loss due to the forbidden line emission increases. This process is very important for plasma diagnostics. Dubau and Loulergue ¹¹⁾ and Mewe ¹²⁾ have calculated these effects. The contribution from K - X rays are larger than that from direct excitation if $n(\text{He}) \sim n(\text{Li})$ at $T_e > 5 \text{ KeV}$ as shown in Fig.6b.

REFERENCES

1) for example

- D.R. Bates, A.E. Kingston and R.W.P. McWhirter, Proc. Roy. Soc. (1962) 267, 297
- T. Fujimoto, J. Phys. Soc. Jap. (1979) 47, 273
- 2) T. Kato, M. Kako, T. Amano, Y. Nomura and S. Hayakawa, (1981), IPPJ-544
- 3) D.E. Post, R.V. Jensen, C.B. Tarter, W.H. Grasberger and W.A. Lokke. (1977), ADNDT, 20, 397
- 4) A. Burges and H.P. Summers (1969), Ap. J. 157, 1007
- 5) B.W. Shore (1975) Lawrence Livermore Internal Report UCIR-854.
- 6) H.P. Summers (1974) Mon. Not. R. Astron. Soc. 169, 663
- 7) V.L. Jacobs, J. Davis, P.C. Kepple and M. Blaha (1977) Ap. J. 215, 690
- 8) T. Kato, K. Masai and J. Mizuno, (1983) J. Phys. Soc. Japan 52, 3019.
- 9) T. Fujimoto, I. Sugiyama and K. Fukuda (1972), Memoirs of the Faculty of Engineering, Kyoto Univ. Vol. XXXIV 249.
- 10) W. Lotz (1968), Zeitschrift für Physik, 216, 241
- 11) J. Dubau and M. Loulergue (1981) Phys. Scripta 23, 136
- 12) R. Mewe, E.H.B.M. Gronenschild (1981) Astron. Astrophys. Suppl. 45, 11.

Figure Captions

- Fig. 1 The collisional radiative ionization rate coefficients S_{CR} for oxygen ions as a function of the electron density. Dotted lines indicate the level of the thermal limit n_e . The electron temperature T_e is 20 eV.
- Fig. 2 The calculated spatial distributions of the oxygen ions in a JIPP-II Tokamak plasma. The solid lines indicate the result with multistep ionization, whereas the dashed lines show the result without multistep ionization.
- a) neutral oxygen
b) ionized oxygen
- Fig. 3 The spatial distribution of the electron temperature T_e and the electron density n_e in JIPPT-II Tokamak, which data were used for the calculation of the distribution of the oxygen ions in Fig. 2.
- Fig. 4 The dielectronic recombination rate coefficient α_d calculated by Summers⁶⁾ (solid lines) and Jacoby et al⁷⁾ (dashed line) for MgX ions. Dotted-dashed line shows the suppressed values calculated by Post's formula³⁾ for $n_e = 10^{16} \text{ cm}^{-3}$ on Summers values ($n_e = 10^4 \text{ cm}^{-3}$).

- Fig. 5 The radiation loss L_{CR} and the ionization loss I_{CR} as-a function of electron density.
- Fig. 6 (a) Ionization rate coefficients for oxygen ions. Solid lines indicates the direct ionization, dotted lines the K-shell ionization, dott-dashed lines the excitation rate coefficient of the resonance line (R) and the forbidden line (F) and the satellite line (q). The recombination rate coefficient are also shown by thin lines for the comparison.
- (b) Ionization rate coefficients for iron ions.
- Fig. 7 The calculated spatial distribution of oxygen ions in JIPP-II Tokamak with 30 KeV suprathemal electrons with a number density 10% of thermal electrons (solid lines) and without suparthermal electrons (dotted lines).

Ionisation rate (Ionising plasma)

$T_e = 20 \text{ eV}$

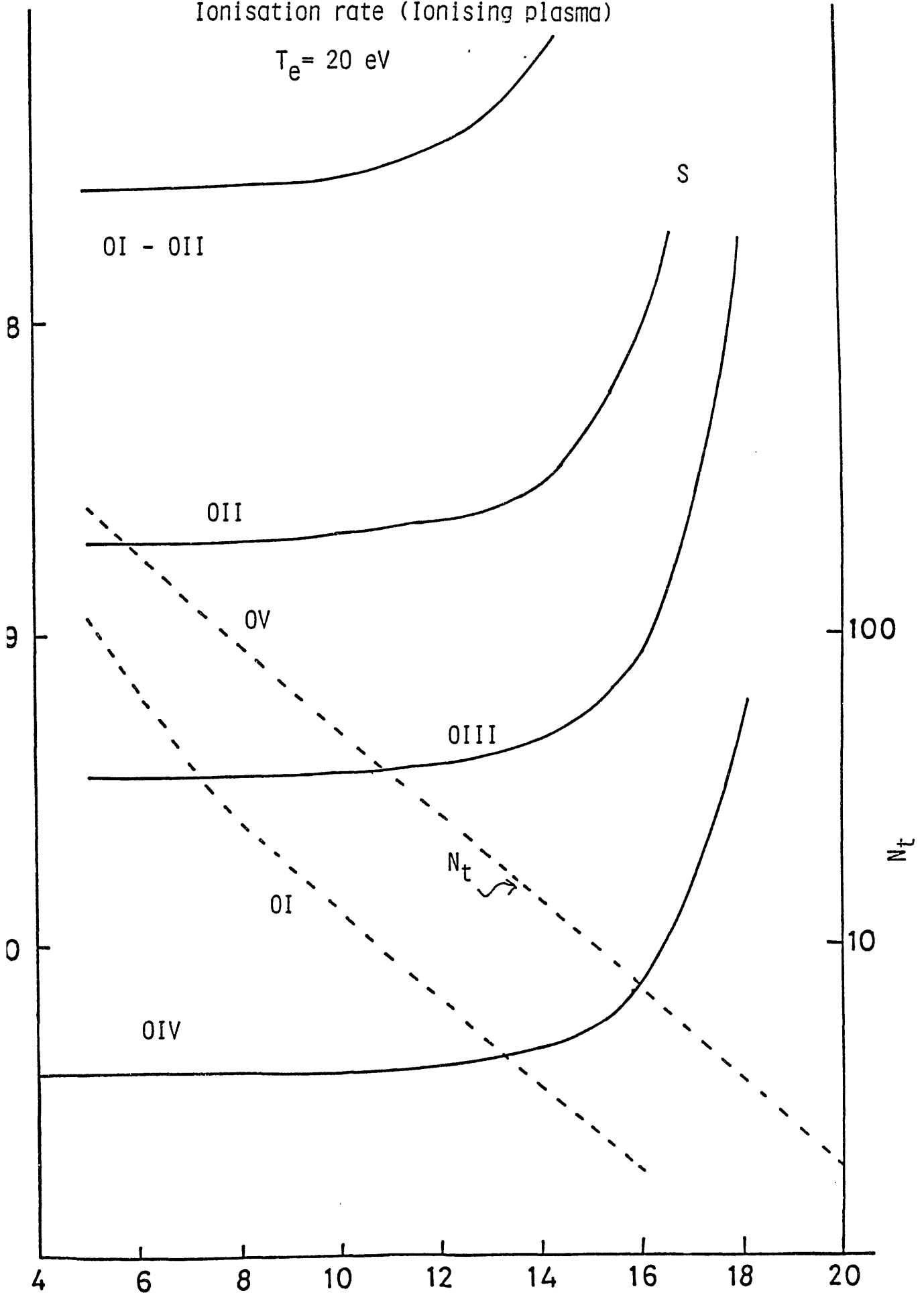
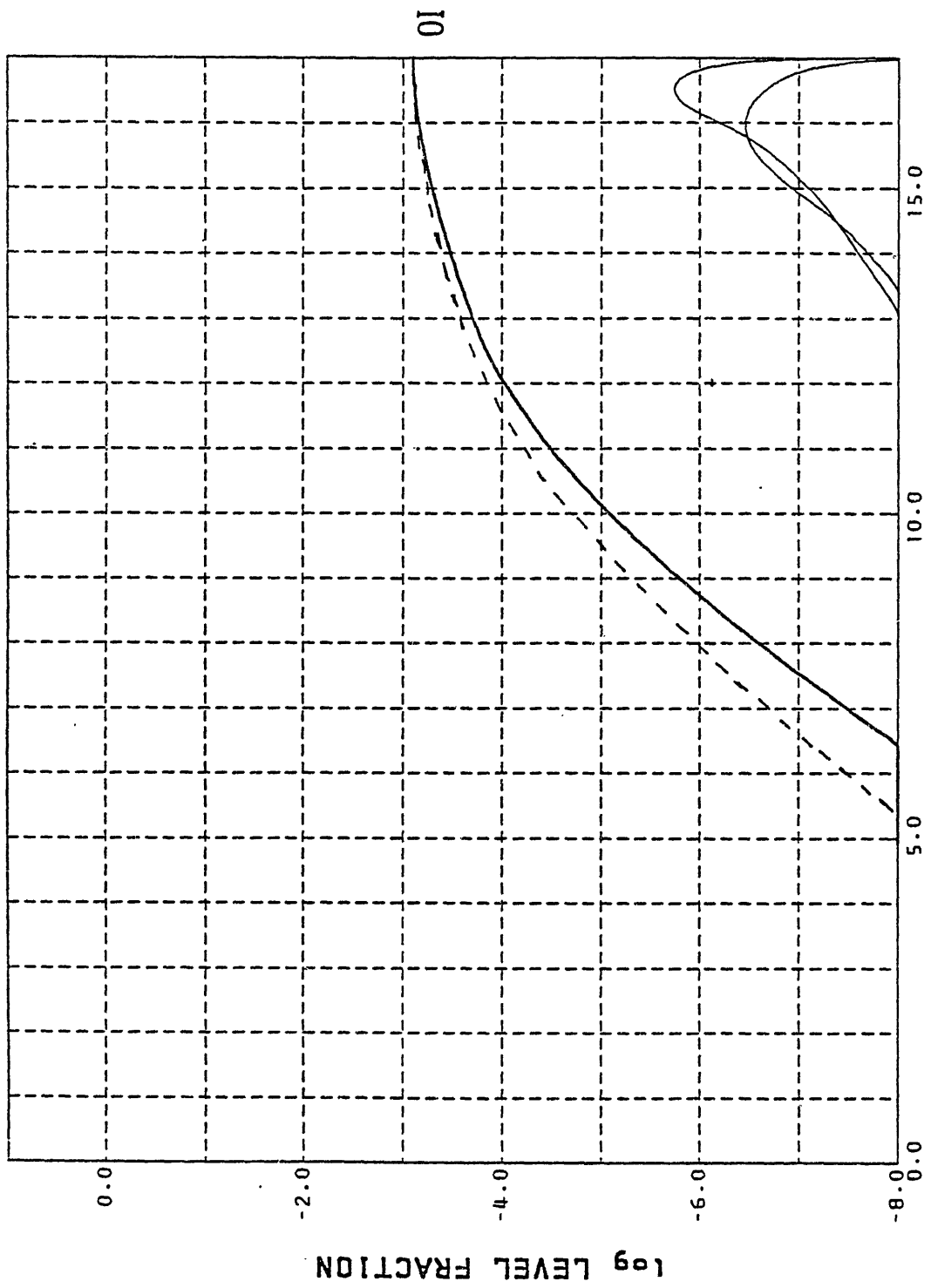
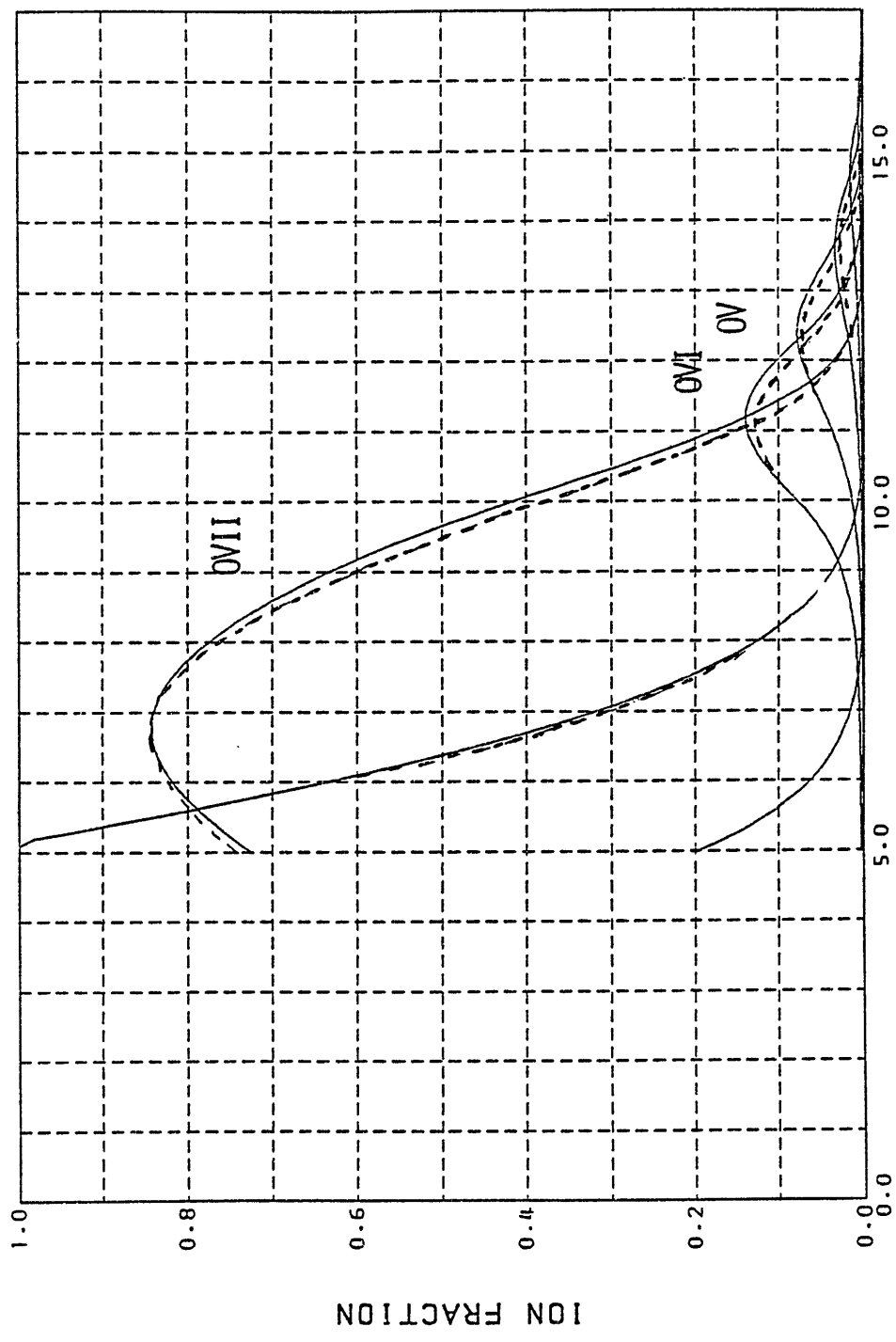


Fig. 1



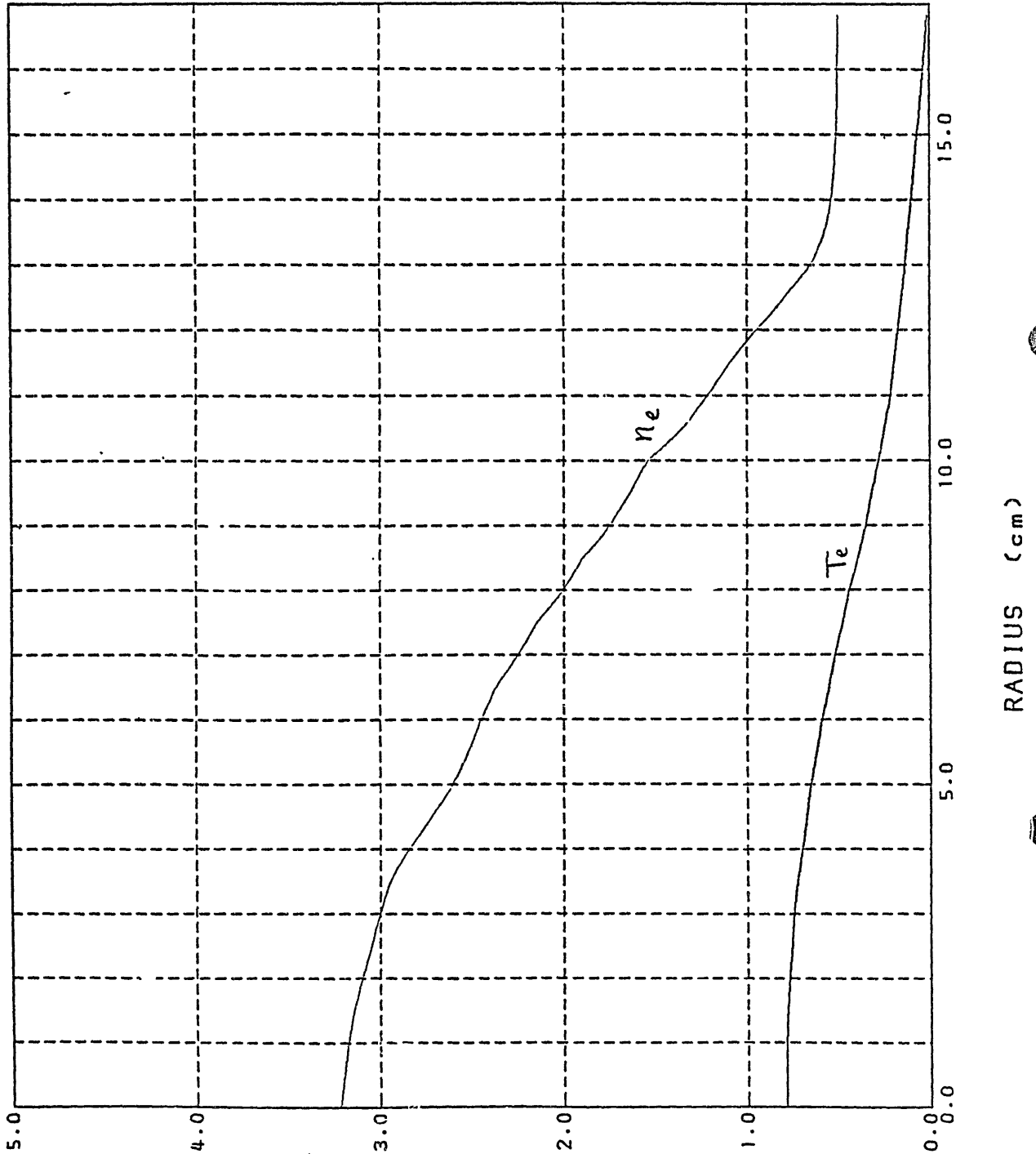
RADIUS (CM)

Fig. 2(a)

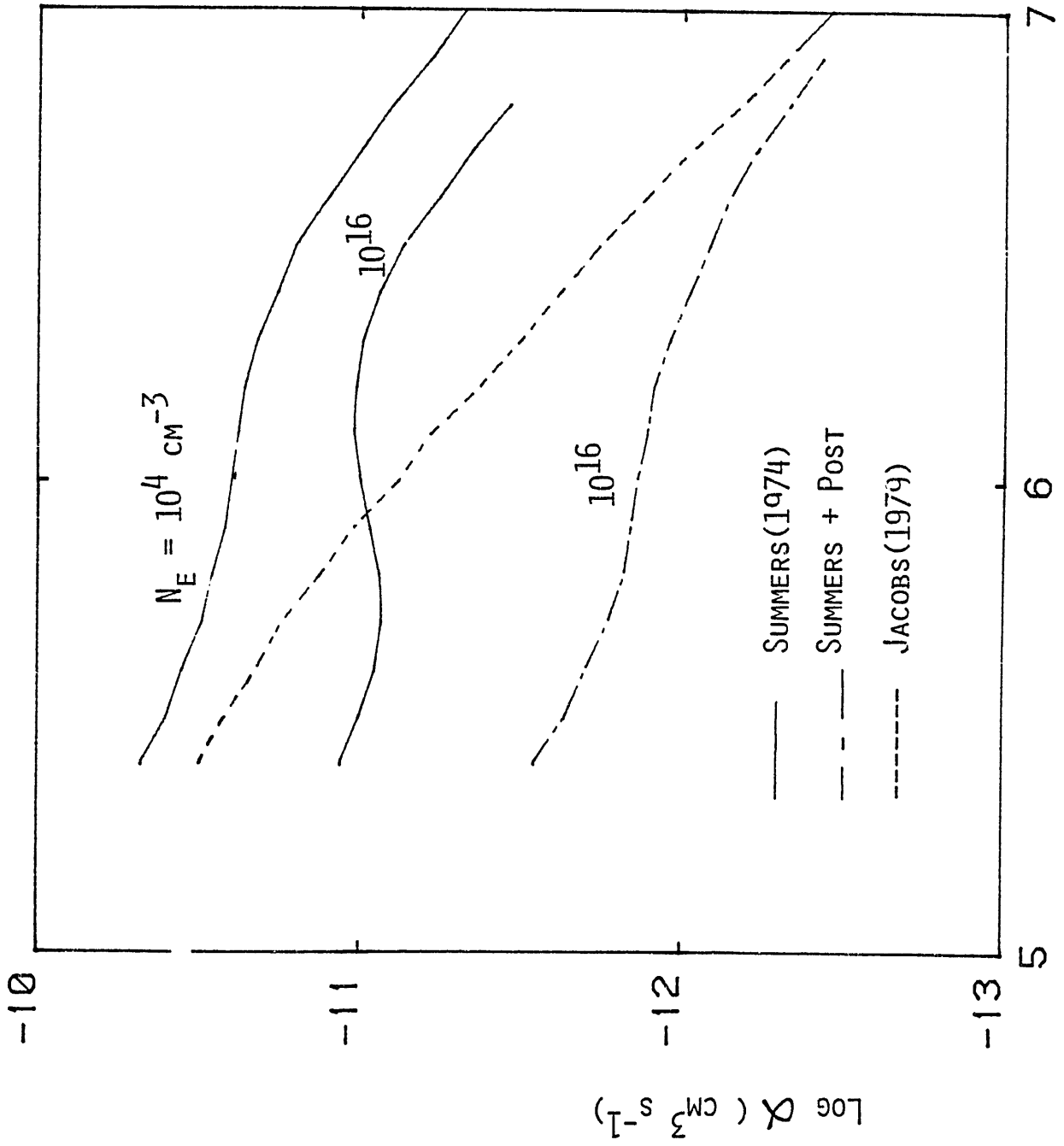


RADIUS (cm)
Fig. 2(b)

ELECTRON DENSITY ($\times 10^{13} \text{ cm}^{-3}$)



ELECTRON TEMPERATURE (keV)



Log T_e (K) Fig. 4

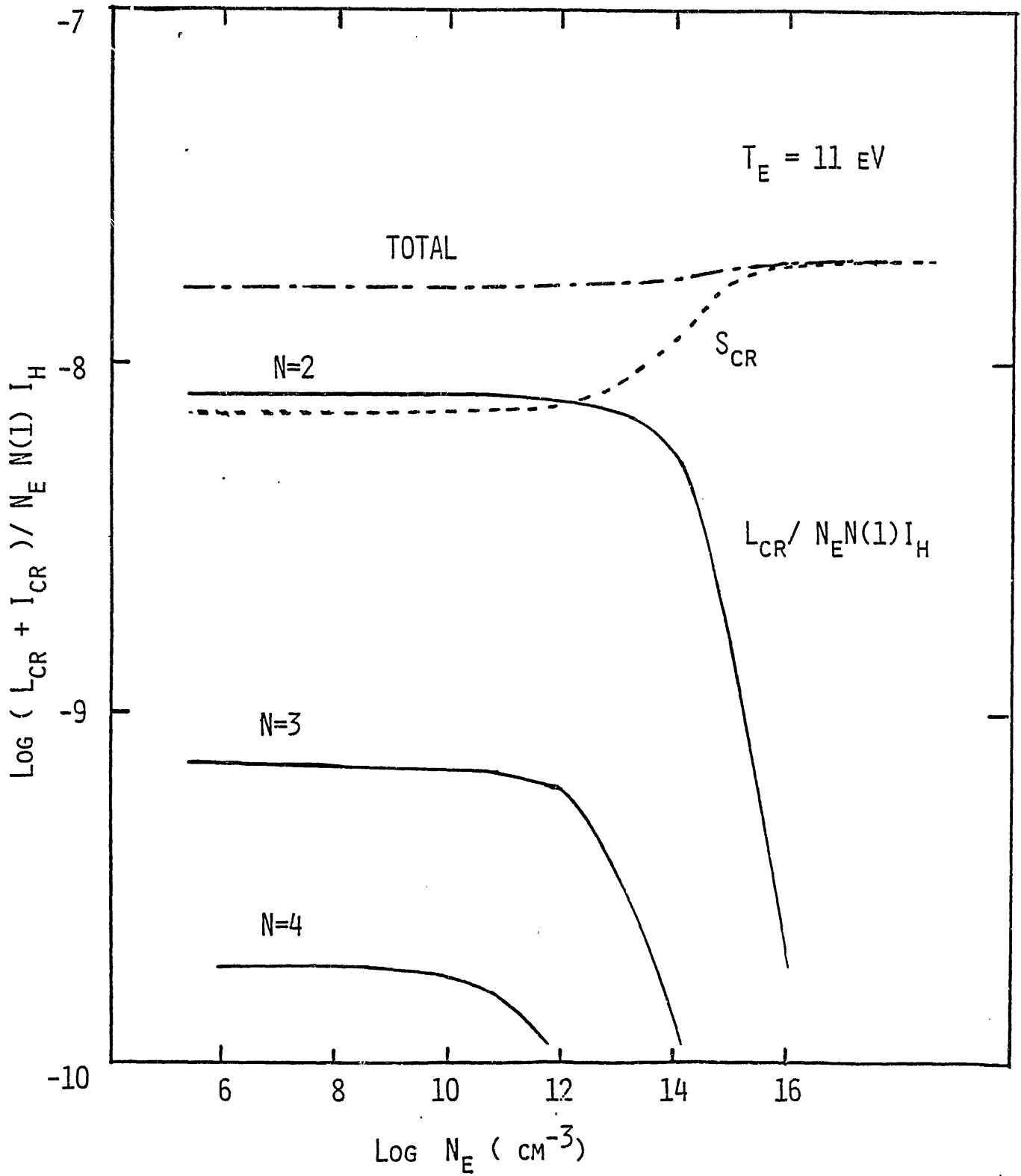


Fig. 5

OXYGEN

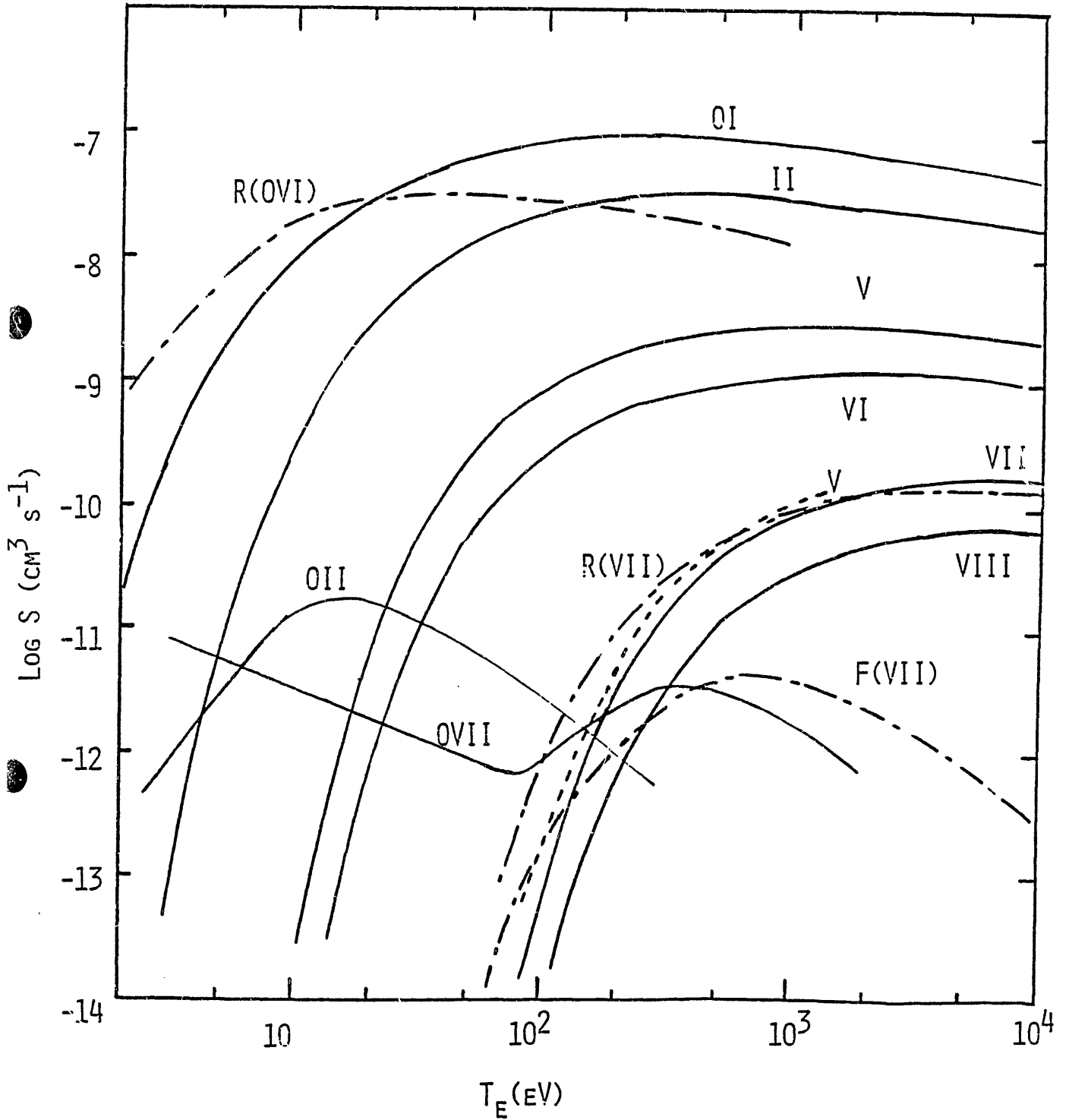
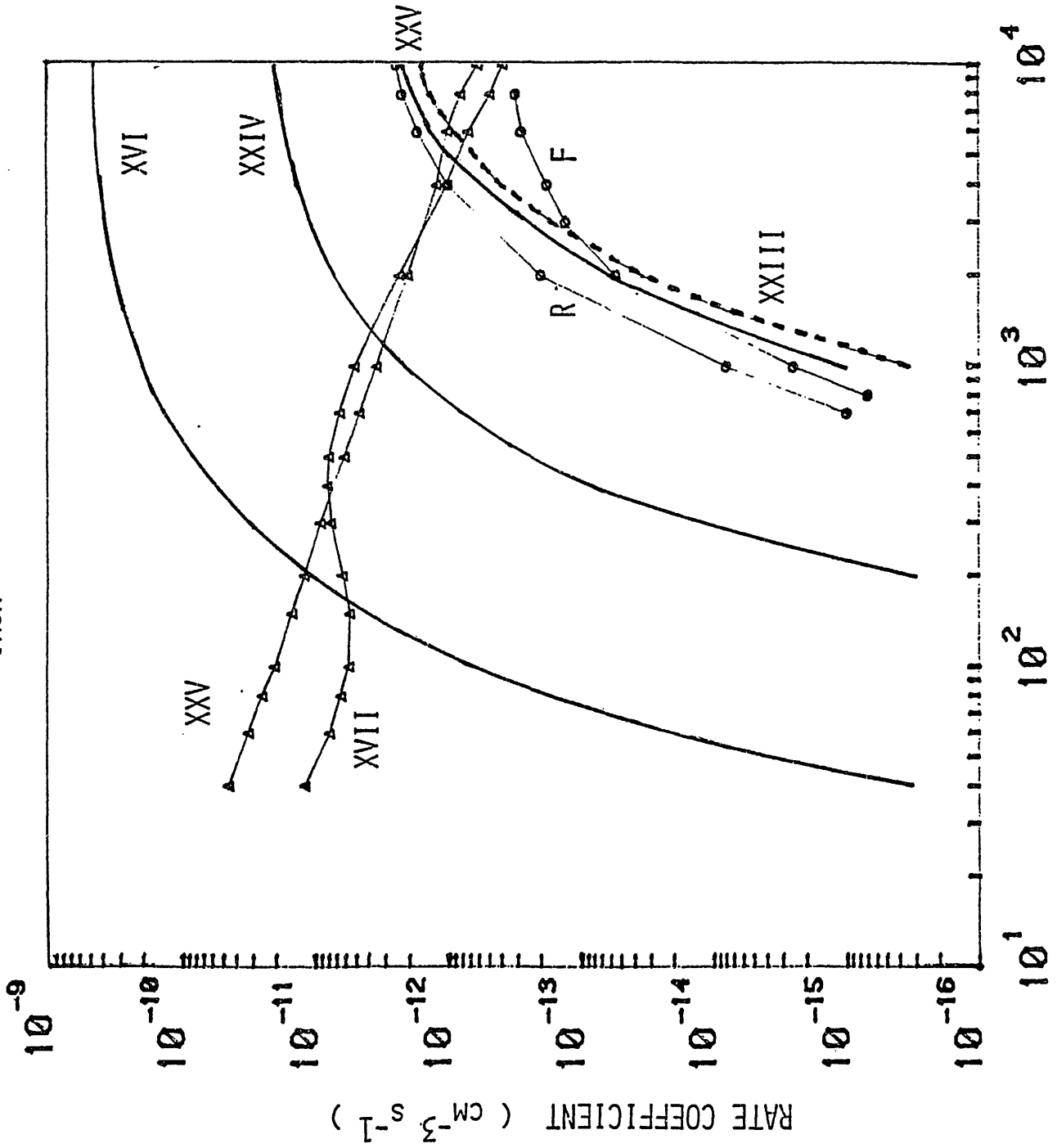


Fig. 6(a)

IRON



T_E (eV) Fig. 6(b)

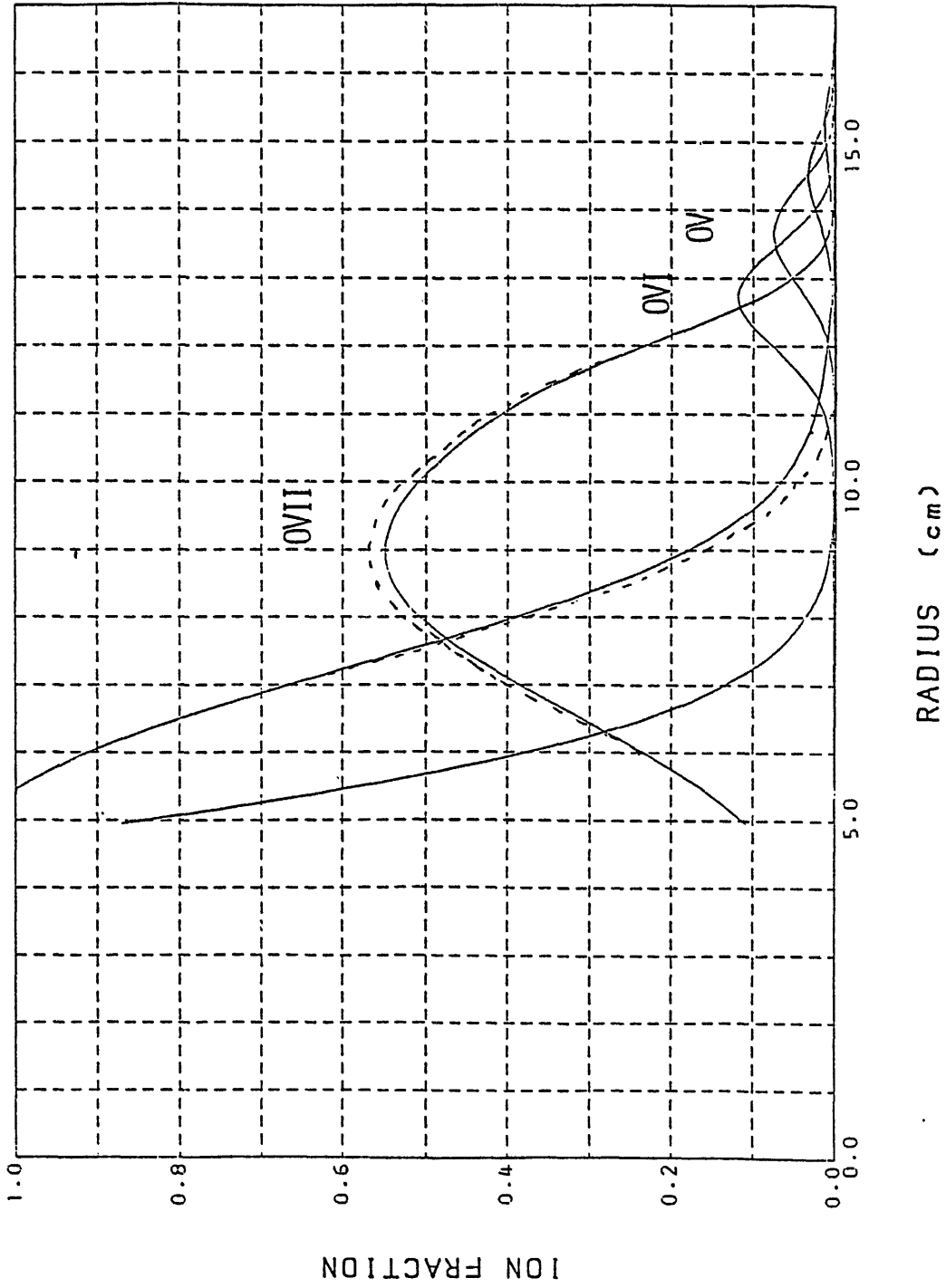


Fig. 7

Plasma Spectroscopy for Plasma Modelling

--- VUV and X-ray Spectroscopy of JIPP-T-IIU Tokamak Plasma ---

T. Kato, K. Masai and S. Morita

Institute of Plasma Physics, Nagoya University, Nagoya, Japan

In order to make a plasma modelling and to check the validity of a plasma modelling, it is necessary to measure the plasma parameters and the distribution of impurities. Plasma spectroscopy has been used as a powerful tool for diagnostics of high temperature plasmas.

We present here the spectroscopic measurement performed for JIPP-T-II Tokamak plasma and discuss the correlation with the plasma modelling as well as the atomic data. In the first section, the basic concepts for the analysis of the spectroscopic data are mentioned and the experimental results are discussed in the next section.

§1. Diagnostics by plasma spectroscopy

To study the behavior of impurities in plasmas, information on the electron temperature T_e and the electron density n_e is of primary importance. T_e and n_e are usually measured independently by different methods, such as Thompson scattering, but such methods become often inapplicable in the peripheral region where n_e is low. Besides it is not generally easy to measure the spatial distribution of each ions. Therefore, it is very helpful if we know T_e and n_e from the line emission itself.

i) Plasma phase

Generally a population of a hydrogenic ion in a plasma is described by superposition of two terms which represent the population formation from the ground state $n_i(1)$ and from the next ionized stage n_{i+1}

$$n(p) = Z(p)r_0(p)n_{i+1}n_e + \{Z(p)/Z(1)\}r_1(p)n_i(1) \quad (1)$$

The first two terms in the right hand side are called the recombining and ionizing terms, respectively. For non hydrogenic ions, the ionization, from the lower ionized stage n_{i-1} and the recombination from the upper ionized stage n_{i+1} should be included ;

$$n(p) = Z(p)r_0(p)n_{i+1}n_e + \{Z(p)/Z(1)\}r_1(p)n_i(1) + S(p)n_{i-1}n_e + \alpha(p)n_{i+1}n_e \quad (2)$$

where $S(p)$ and $\alpha(p)$ are the ionization and recombination rate coefficient to the level p of ion n_i .

In a Tokamak plasma, the ionizing term is dominant for low ionized ions, because the temperature is high compared with that giving equilibrium ion abundances due to the inward transport of ions. The ionization term $S(p)$ is expected to be large and this was confirmed by the spectroscopic measurement of OIV and OV lines²⁾ which will be discussed in §2. The ionizing term is also important for highly ionized ions in the central region.

On the other hand, if highly ionized ions diffuse out of the center to the periphery regions, the recombining term dominates. We always have to pay attention to the distinction between these plasma phases, whether ions under consideration are in the ionizing or recombining phase.

From the line intensities of the resonance series, we can see whether the plasma is ionizing or recombining. The line intensities of resonance series of helium like Fe ions in two plasma phases (ionizing phase and recombining phase) are shown in Fig. 1. The line intensities decrease rapidly for ionizing phase and slowly for recombining phase³⁾. This is also possible by the observation of the intensity ratio between the singlet resonance line ($1^1S - 2^1P$, referred to as w) and the triplet

line ($1^1S - 2^3S$, z and $1^1S - 2^3P_{1,2}$, y and x). This is illustrated in Fig. 2. Note that the ratio is very high ~ 5 in the recombining phase at low temperature. The contribution of recombining phase have been studied on the spectroscopic data of ions from the solar corona⁴⁾ and Al ions from laser produced plasmas³⁾.

ii) Temperature

It is well known that the line intensity ratio for different principal quantum members n shows an electron temperature dependence due to a large difference between the excitation energies of two lines. For example the intensity ratio of $I(3p-2s)/I(2p-2s)$ for Li-like ions can be used to measure the electron temperature. Resonance series lines are suitable for this purpose. The temperature dependence of the intensity ratio I_t/I_r of OV and OIV ions are shown in Fig. 3 as an example (see Table I).

iii) Density

The density measurement can be performed with use of the line intensity ratio of the line produced by excitation from/to a metastable state to the resonance line. The famous lines to be used are 2^3S-1^1S and 2^3P-1^1S of He like ions. The line intensity ratios of OVII and Fe XXV are shown in Fig. 4 as a function of n_e for a equilibrium plasma. In an equilibrium plasma, the intensity ratios at low density are decided by the excitation processes. The forbidden line z decreases and the intercombination line (x+y) increases by the excitation from the 2^3S to the 2^3P state when n_e increases. But the excitation from 2^3P to 2^1P state and the ionization from 2^3P make (x+y) decrease, and only the resonance line w can be observed at very high density as shown in Fig. 4. The contribution of the recombination from the hydrogenic ions are shown by dotted lines in the figure. In a recombining plasma,

the recombination rates determine the line intensity at low densities. But the line intensities of triplet states decreases due to the excitation from the triplet states to the singlet states and to the ionization at high densities. The line intensity ratio $(x+y)/w$ for AlXII ions in the recombining phase are shown in Fig. 5 as an example.

The intensity ratios of Be-like, B-like and C-like ions have been studied for oxygen ions⁶⁾ and are applied to Tokamak plasmas²⁾. The energy level diagram for these ions are shown in Fig. 6. The two successive excitation processes makes the line intensity ratio density dependent. For example the $2p^3(^3p)$ level is mainly populated by the excitation from the metastable state $2s2p(^3p)$ while the $2s2p(^1p)$ is populated from the ground state. Then the population density of $2p^3(^3p)$ has a quadratic dependence on n_e , while the $2s2p(^1p)$ for the resonance line is directly populated from the ground state. Therefore the intensity ratio $I_j(2p^3(^3p)-2s2p(^3p))/I_r(2s2p(^1p)-2p^2(^1s))$ is proportional to n_e at low densities⁶⁾. We have to be careful for the inner subshell ionization by which the metastable states populate very much²⁾. In Fig. 7 we show the density dependence of the line intensity ratios of OIV and OV ions with and without the inner subshell ionization.

iv) Satellite lines

Satellite lines of Li-like ions have been studied extensively by Bely-Dubau et al^{7),8)}. These lines can be used to know both temperature and density. In a density region of Tokamak, satellite lines are used to know the electron temperature and the ion abundance, whereas they can be used as the density measurement at higher densities such as laser produced plasmas.

Satellite lines are produced by dielectronic capture and also inner shell excitation/ionization. The satellite line caused by die-

dielectronic recombination gives the electron temperature, whereas those produced by inner shell excitation or ionization the ion abundance. When the plasma is in the recombining phase, the intensity of the resonance line I_r is proportional to the ion density of the upper ionized stage. For example, the intensity of the dielectronic satellite line of Li-like ions $I_s(\text{Li})$ should be compared to that of the resonance line of the Li-like ions $I_r(\text{Li})$ instead of the He-like ions to know the electron temperature. In Fig. 8 satellite line ratios are shown for ionizing⁷⁾ and recombining plasma³⁾ respectively.

v) Ion distribution

The spatial distribution of ions in Tokamak is important for plasma modelling. The distribution of the degree of ionization deviates from that in the corona equilibrium due to the transport of ions. The neutral impurities are ejected with a velocity V_0 from the wall, and they enter into the plasma and are ionized successively. The ion distributions are determined by V_0 , the diffusion coefficient D , and the convection velocity V as well as n_e and T_e distributions. The comparison of the oxygen ion distribution for $V_0 = 0.025$ eV and 10 eV are shown in Fig. 9 for a JIPPT-II Tokamak plasma. The distribution of neutral atoms greatly affects the distribution of ions. A deviation from the corona equilibrium gives the information on the drift of ions and the shell width gives that on the diffusion.

§2. VUV and X-ray Spectroscopy of JIPPT-IIU Tokamak

i) VUV Measurement

The lines of OIV and OV ions were measured by VUV grazing incident monochromator. The measured lines are listed in Table I. The intensity ratio I_i/I_r is a density indicator whereas I_t/I_r gives the temperature as discussed in §1. One set of data for OV ions are shown in Fig. 10. From the ratio I_t/I_r , the electron temperature decreases

very rapidly at 120 ms by gas puffing and by RF heating and increase gradually after finishing RF. The temperature obtained from the intensity ratio are indicated in Fig. 10(a). On the contrary the ratio I_i/I_r shows small enhancement. The observed values I_i/I_r are indicated in Fig. 7(a) by the arrows with T_e values derived from I_t/I_r . When we take into account the temperature dependence of I_i/I_r including the inner subshell ionization with $n(OV)/n(OIV) = 1.5$, the density is found not increasing ^{so much} and staying around several times 10^{12} cm^{-3} ; I_i/I_r increases due to the energy dependence of the excitation cross section to the metastable state when the electron temperature decreases. Hence, the I_i/I_r in Fig. 10(b) implies that n_e in the region where OV is most abundant does not change very much. This may be understood as follows ; after n_e is increased, OV is abundant in the outer region compared to the ohmic heating phase < 120 ms. However the other possibility that the electron density outside do not change very much by puffing or RF heating, remains. The time evolution of the mean electron density measured by Thompson scattering is shown in Fig. 10(c). The intensity ratios of OVI and OIV ions also show the very clear temperature variation as OV ions. These lines are found to be useful for the diagnostics in the periphery of plasma. I_i and I_r from Fe XXII ions (Table I) have been also observed as shown in Fig. 11. It can be clearly seen that n_e stays constant in the case (a) whereas n_e increases after gas puffing in the case (b). These lines are approved to be good indicators of n_e .

ii) X-ray Measurement

a) TiXXI (He-like) lines

A high resolution spectrum of TiXXI ions was measured by means of a Bragg curved crystal spectrometer from JIPPT-IU Tokamak in a Ne

gas (30 %) discharge. Fig. 12 shows the spectra from 2.60 to 2.65 Å. The most prominent peaks are identified as the He-like lines w, x, y and z, the Li-like n = 2 satellites q, j and k and Be-like line β. The key letters refer to Gabriel's notation⁹⁾.

T_e is derived from the observed values j/w and k/w with the use of the theoretical calculation⁷⁾ and the results are shown in Fig. 13. We take into account the intensity increase of the resonance lines due to unresolved dielectronic satellite with $n \geq 3$. T_e increases from 1 keV (40 ~ 60 ms) to 1.5 keV (60 ~ 80 ms) as the time advances and decreases to 1.3 KeV in the period of 80 ~ 100 ms as seen in Fig. 13. We calculate the ion abundances $n(\text{Li})/n(\text{He})$ from q/w and $n(\text{Be})/n(\text{He})$ from β/w using T_e values derived from satellite lines. Both the densities of Li-like ions and Be-like ions decrease very rapidly from the first period (40 ~ 60 ms) to the second period (60 ~ 80 ms), but increase a little towards the third period (80 ~ 100 ms). This is interpreted that the plasma is in the ionizing phase in the first period but the ionization stops and reaches equilibrium at the second period. The recombination phase may begins at the third period, because g/w and β/w show a little increase.

We have studied the line intensity ratios $G = (x+y+z)/w$, x/w , y/w and z/w . The observed points of G are plotted in Fig. 2. They are too high to be in the ionizing phase or the equilibrium phase. The contribution of recombination suspected in the third and fourth periods. The contribution of H-like ions are shown in Fig. 2 by dott-dashed lines for $n(\text{H})/n(\text{He}) = 10^{-2}$ and 5×10^{-2} . The ratios x/w , y/w and z/w are plotted and the theoretical values in the equilibrium phase are indicated by solid lines for y/w and z/w in Fig. 13. Large discrepancy from ionizing/equilibrium phase is observed especially for x and y.

The dotted lines for z/w is the values including the inner shell ionization of Li-like ions. The contribution of suprathermal electrons to w is found small in this Ne discharge. The collisional radiative model developed for the population analysis of He-like ions¹⁰⁾ is used for the spectral analysis of w , x , y and z lines.

b) K X-rays

Broad band spectra of K-lines of several ions were obtained as shown in Fig. 14 during the LHCD operation. The time dependence during the LHCD operation of the total emission in all the wavelength range are observed. Although the electron temperature decreases very rapidly after the gas puffing at 100 msec, the K X-rays emission still remains. This indicates the contribution of suprathermal electrons. The suprathermal component is obtained from these data.

c) The wavelength of K X-rays of low ionized ions

K X-rays spectra of low ionized ions of Ti and Fe ions are measured, as shown in Fig. 15 as an example. The available data of the wavelengths of low ionized ions for K X-rays are very poor, but are important for plasma modelling which uses the K X-rays as diagnostics. We can obtain the ionization stage by measuring K X-rays. From the precision measurement of the wavelength, it would be possible to verify the QED theory by extracting the Lamb shift.

The precise wavelengths would be available from our measurement.

References

- 1) T. Fujimoto (1979), J. Phys. Soc. Japan 47, 265.
- 2) T. Kato, K. Masai and K. Sato (1985), Physics Letters A 108, 259.
- 3) T. Fujimoto and T. Kato, J. Phys. D 14, 439 (1981).
- 4) T. Fujimoto and T. Kato, Ap. J. 246, 994 (1981).
- 5) A.H. Gabriel and C. Jordan (1972) "Case Studies in Atomic Collision Physics", Vol. 2 (North-Holland Publ., Amsterdam) 211.
- 6) T. Kato, K. Masai and J. Mizuno, J. Phys. Soc. Japan (1981), 52, 3019 (1983).
- 7) F. Bely-Dubau, P. Faucher and L. Steenman-Clark (1982) Phys. Rev. A 26, 3459.
- 8) F. Bely-Dubau, A. Gabriel and S. Volonté (1979) M.N.R.A.S. 186, 405.
F. Bely-Dubau, A. Gabriel and S. Volonté (1979) M.N.R.A.S. 189, 801.
F. Bely-Dubau, J. Dubau, P. Faucher and A.H. Gabriel (1982) M.N.R.A.S. 198, 239.
- 9) A.H. Gabriel (1972) M.N.R.A.S. 160, 99.
- 10) T. Fujimoto and T. Kato (1984) Phys. Rev. A 30, 379.

Table I
Observed lines

Ion	Line	Transition	W. L. (Å)
OV	I _r	$2s2p(^1P_1) - 2s^2(^1S_0)$	629.73
	I _i	$2p^2(^3P_2) - 2s2p(^3P_2)$	760.445
	I _t	$2s3p(^1P_1) - 2s^2(^1S_0)$	172.17
OIV	I _r	$2s2p^2(^2D_{3/2,5/2}) - 2s^22p(^2P_{3/2})$	790.1,.2
	I _i	$2p^3(^4S_{3/2}) - 2s2p^2(^4P_{5/2})$	625.85
	I _t	$2s^23d(^2D_{5/2,3/2}) - 2s^22p(^2P_{3/2})$	238.57
FeXXII	I _r	$2s2p^2(^2S_{1/2}) - 2s^22p(^2P_{1/2})$	117.12
	I _i	$2s2p^2(^2P_{3/2}) - 2s^22p(^2P_{3/2})$	114.39

Figure Captions

Fig. 1. The intensities of resonance series lines of FeXXIV for Ionizing phase and Recombing phase in the plasma at $T_e = 1$ keV and $n_e = 2 \times 10^{13} \text{ cm}^{-3}$.

Fig. 2. The intensity ratio $G = (x+y+z)/w$ for He-like TiXXI ions as a function of electron temperature. The solid lines indicate the ratio for an equilibrium phase and a recombining phase, and dotted lines for an ionizing phase, respectively. The contribution from H-like ions are shown by dott-dashed lines for $n(\text{H})/n(\text{He}) = 10^{-2}$ and 5×10^{-2} .

Fig. 3. The intensity ratio I_t/I_r (see Table I) for OIV and OV ions as a function of electron temperature.

Fig. 4. The intensity ratio of He-like ions as a function of n_e .

(a) For OVII ions in the equilibrium plasma at $T_e = 2 \times 10^6$ K.

Dotted lines indicate the contributions of the recombination from the upper ionized ions.

Dott-dashed lines are the results by Gabriel and Jordan⁵⁾.

(b) For FeXXV ions in the equilibrium plasma at

$$T_e = 5.8 \times 10^2 \text{ K.}$$

Fig. 5. The intensity ratio of $(x+y)/w$

for AlXII ions in the recombining phase at $T_e = 10^6$ K, 3×10^6 K and 10^7 K³⁾.

Intercombination line $(x+y)$ decreases due to the excitation from the 2^3P to the 2^1P state as the n_e increases.

Fig. 6. A schematic energy level diagram for OIII, OIV and OV ions.

Fig. 7. Intensity ratio I_i/I_r for a) OV and b) OIV ions.

Fig. 8. a) The intensity ratio of the satellite intensity $I_j(\text{Li})$ of Li-like ions to the resonance line $I_w(\text{He})$ of He-like ions as a function of temperature for the ionizing Ti plasma.

b) The intensity ratio of the satellite line $I_s(\text{He})$ to the resonance line $I_w(\text{He})$ of the He-like Al ions in the recombining plasma.

Fig. 9. The calculated spatial distribution of oxygen ions in a JIPPT-II Tokamak. a) $V_0 = 0.025$ eV, b) $V_0 = 10$ eV.

Fig.10. a) The observed line intensities I_r , I_t and I_t/I_r of OV ions as a function of time.

b) The observed line intensities I_r , I_i and I_i/I_r of OV ions as a function of time.

c) The time variation of the mean electron density.

Fig.11. The observed line intensities I_i , I_r and the intensity ratios I_i/I_r of FeXXII lines as a function of time.

Fig.12. Experimental spectra of TiXXI in the four period ;
1 (40 ~ 60 ms), 2 (60 ~ 80 ms), 3 (80 ~ 100 ms) and
4 (100 ~ 120 ms).

Fig.13. The observed line intensity ratios j/w , k/w , q/w , z/w , x/w and y/w as a function of time. T_e derived from j/w and k/w , $n(\text{Li})/n(\text{He})$ from q/w and $n(\text{Be})/n(\text{He})$ from β/w are also shown.

Fig.14. Broad band spectrum of K X-rays of Fe ions. Solid line is the spectra obtained during the LHCD operation and dashed line during the ohmic discharge, respectively.

Fig. 15. K X-ray spectra of low ionized ions of Fe ~~ions~~.

FE XXIV

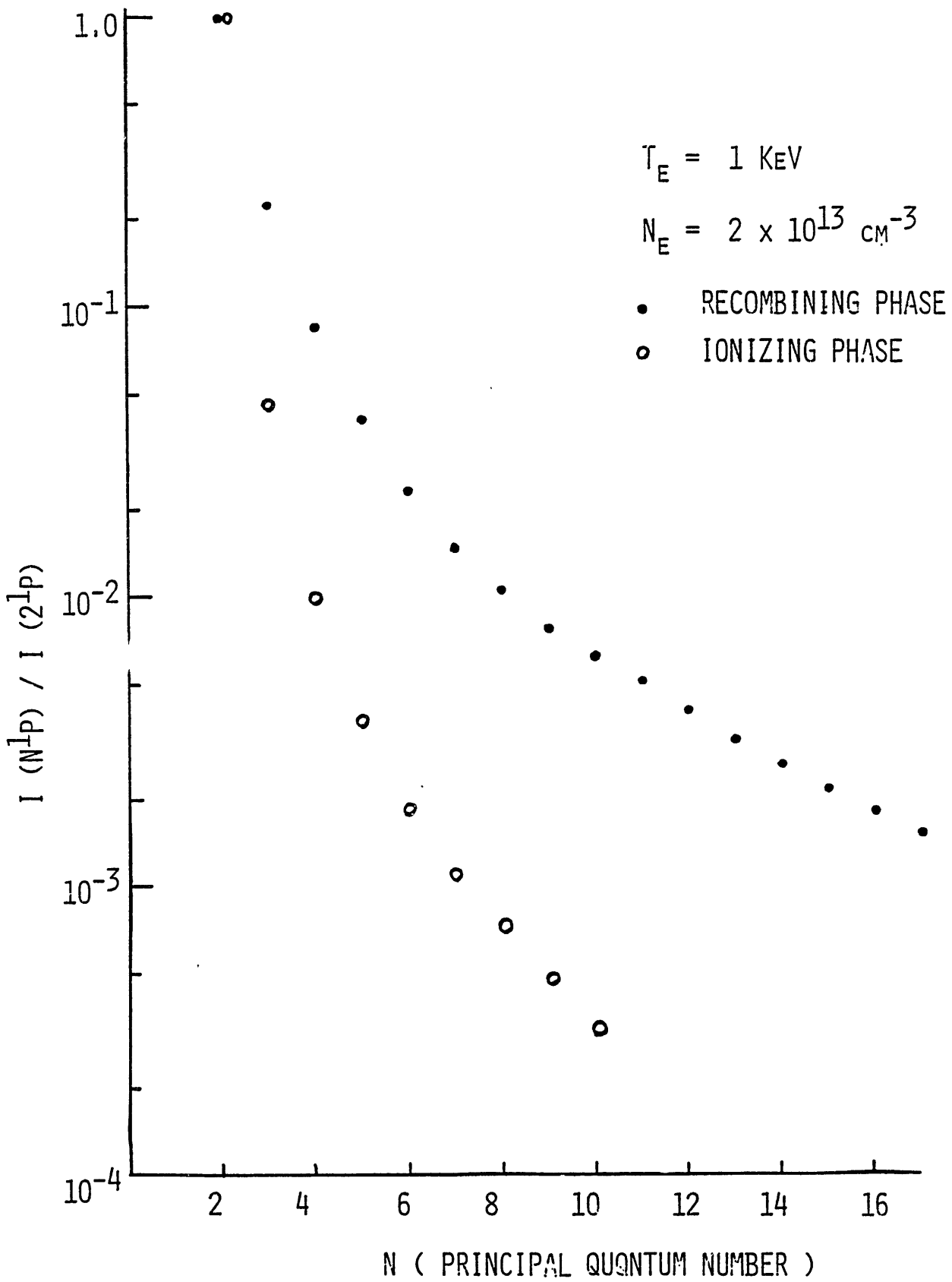


Fig. 1

$$G = (x + y + z) / w$$

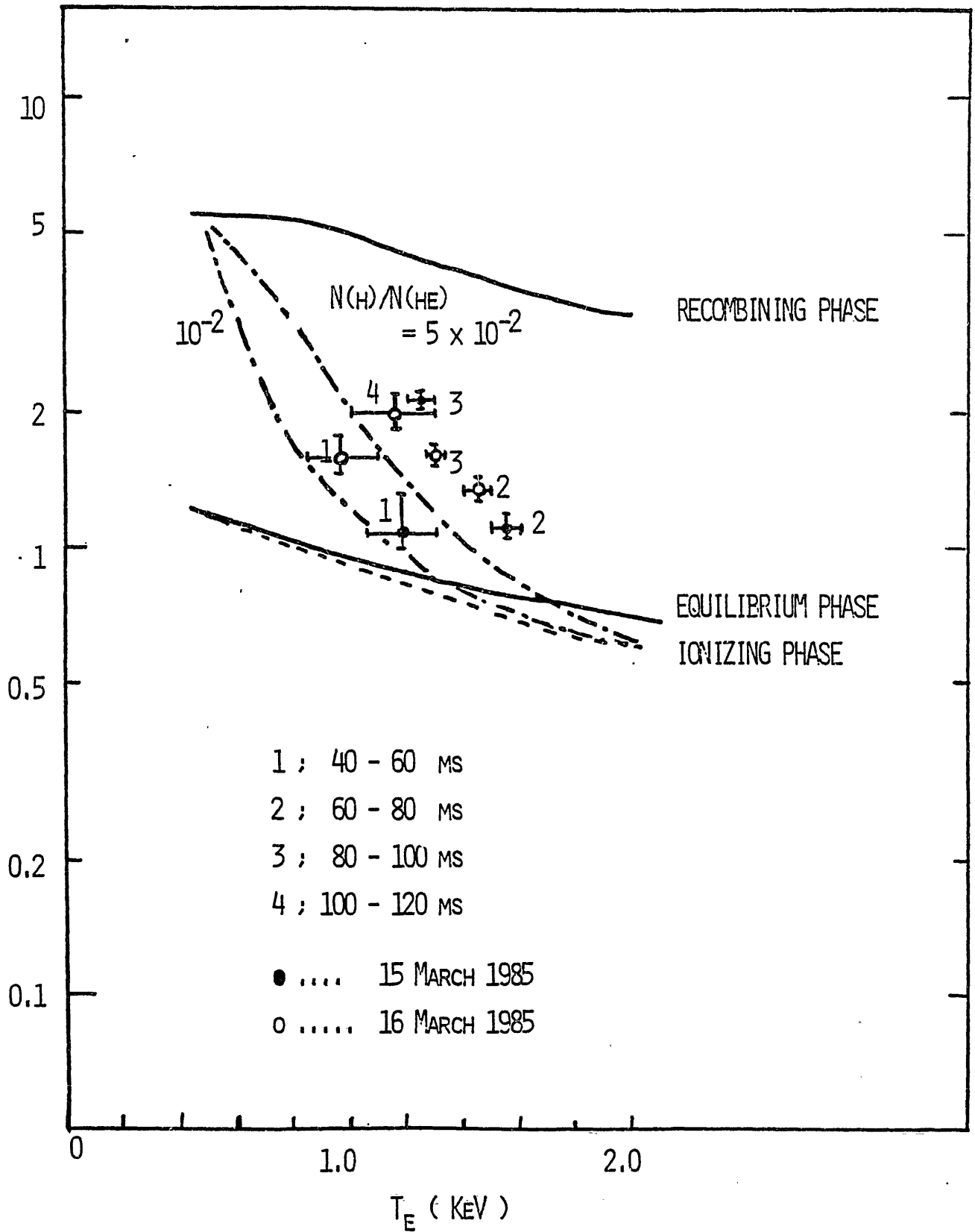


Fig. 2

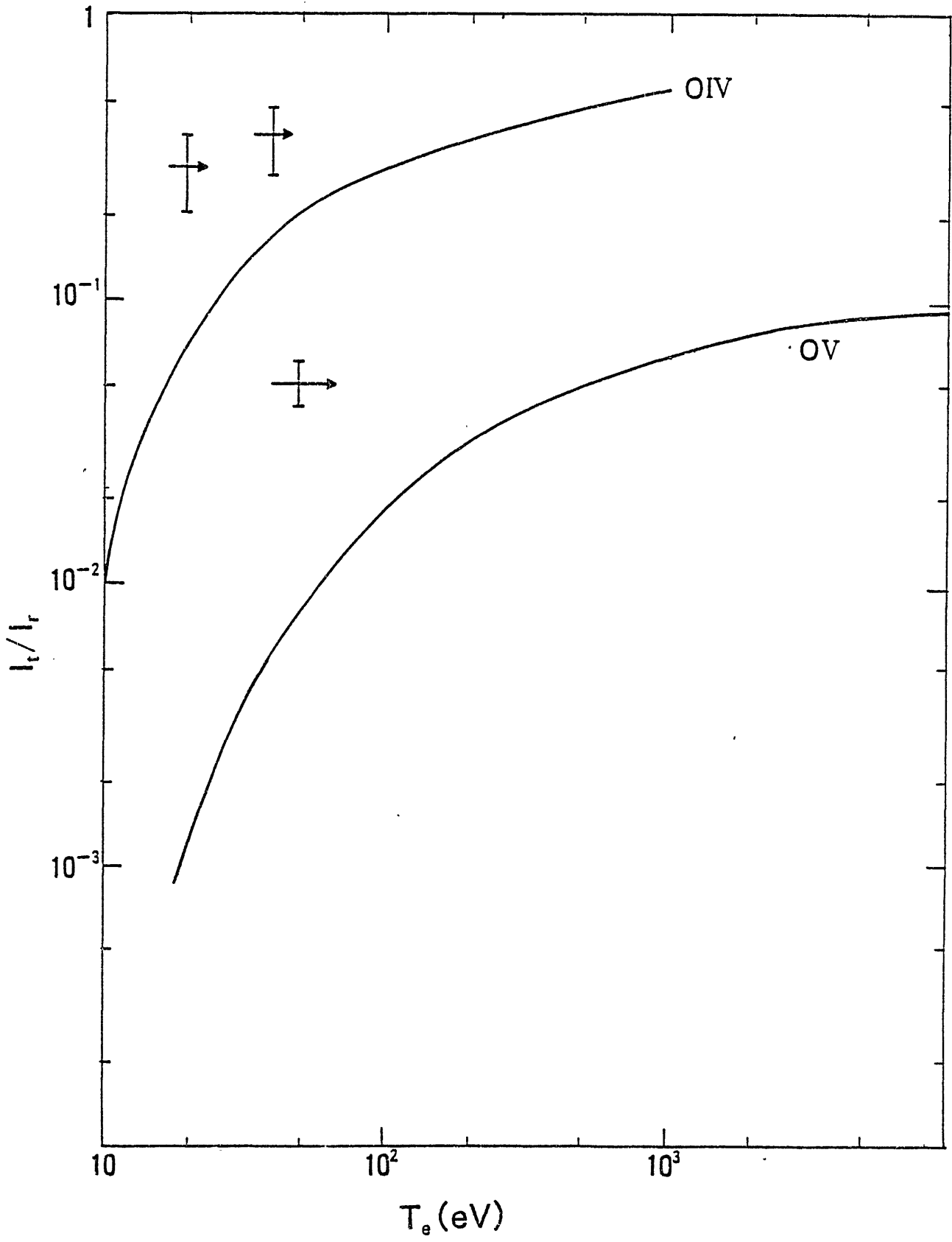


Fig. 3

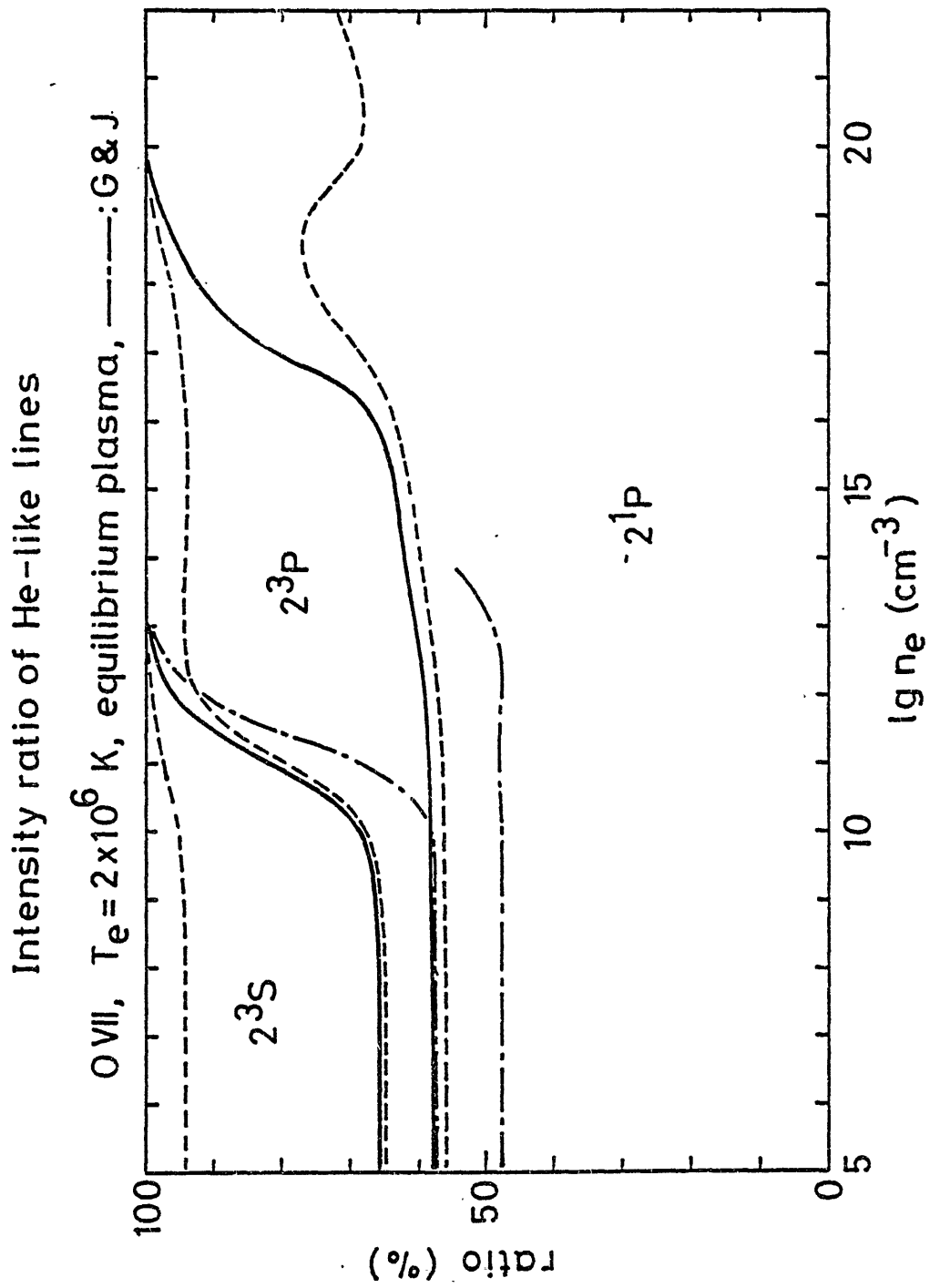


Fig. 4(a)

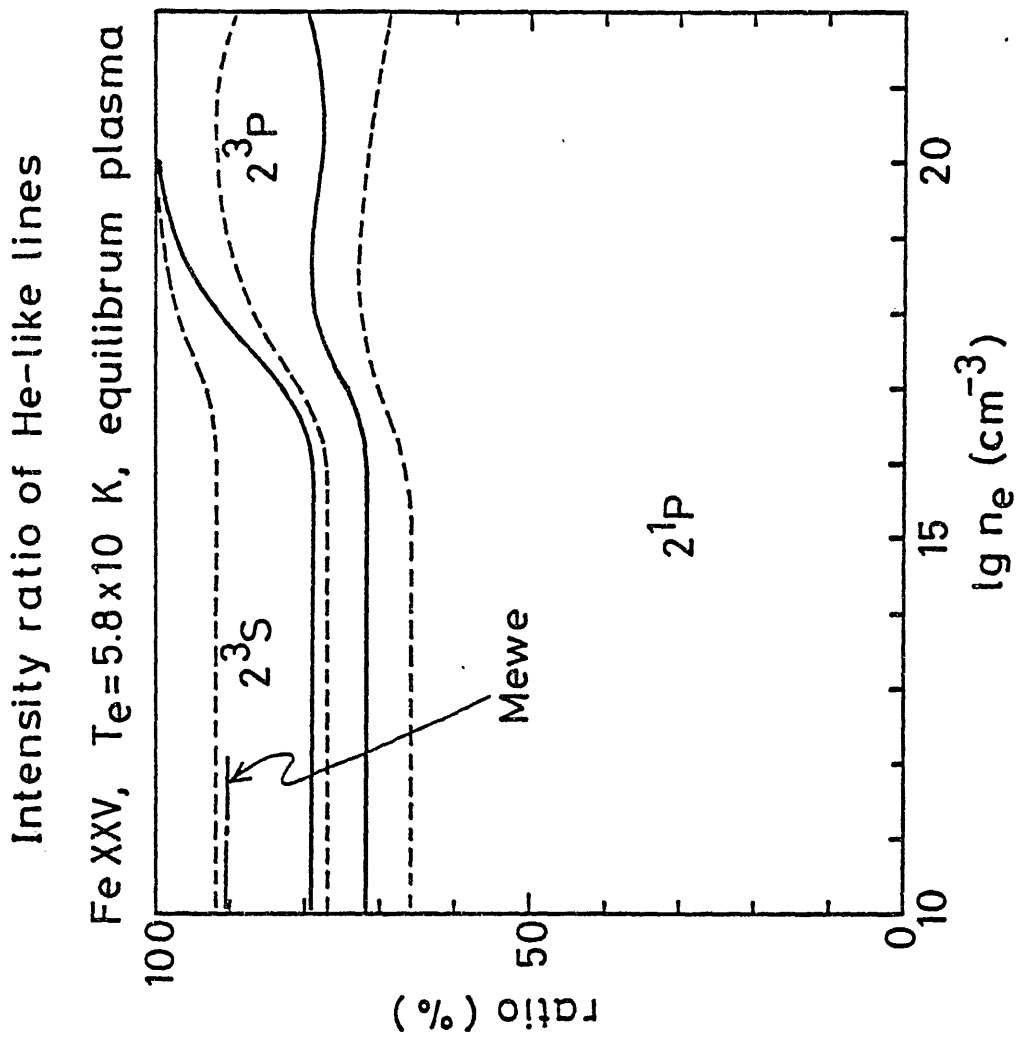


Fig. 4(b)

Recombining phase

Al XII

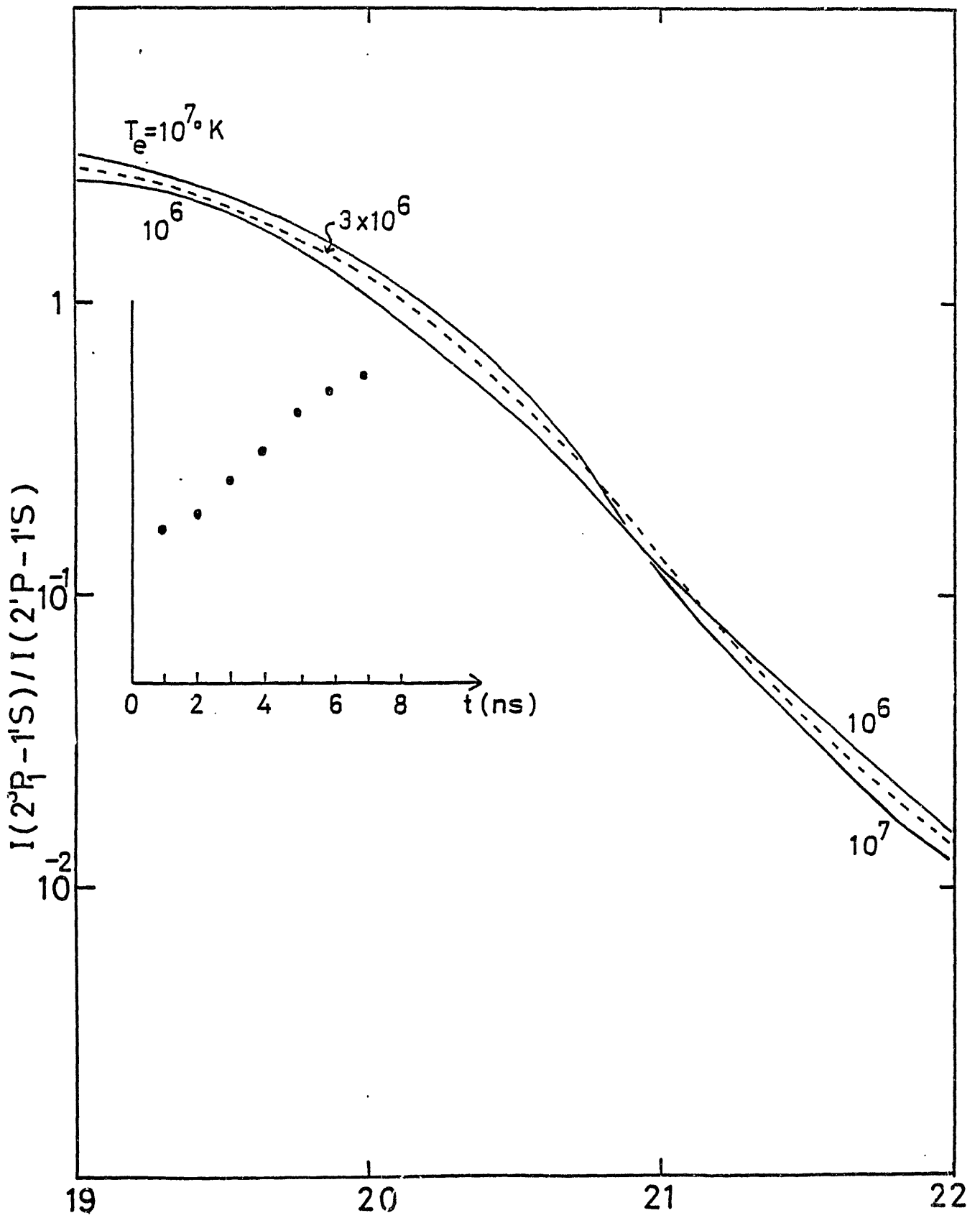


Fig.5

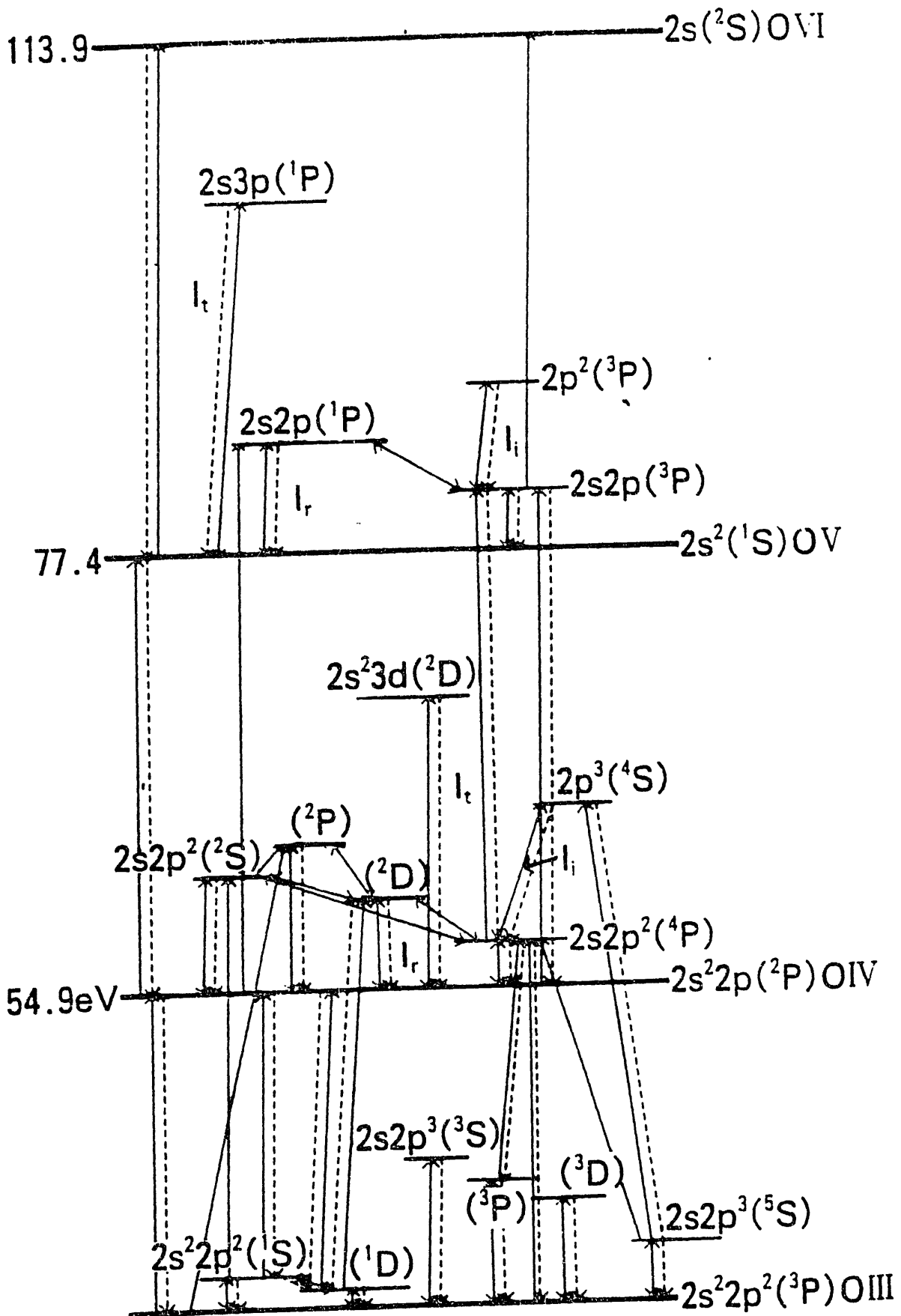


Fig. 6

OV

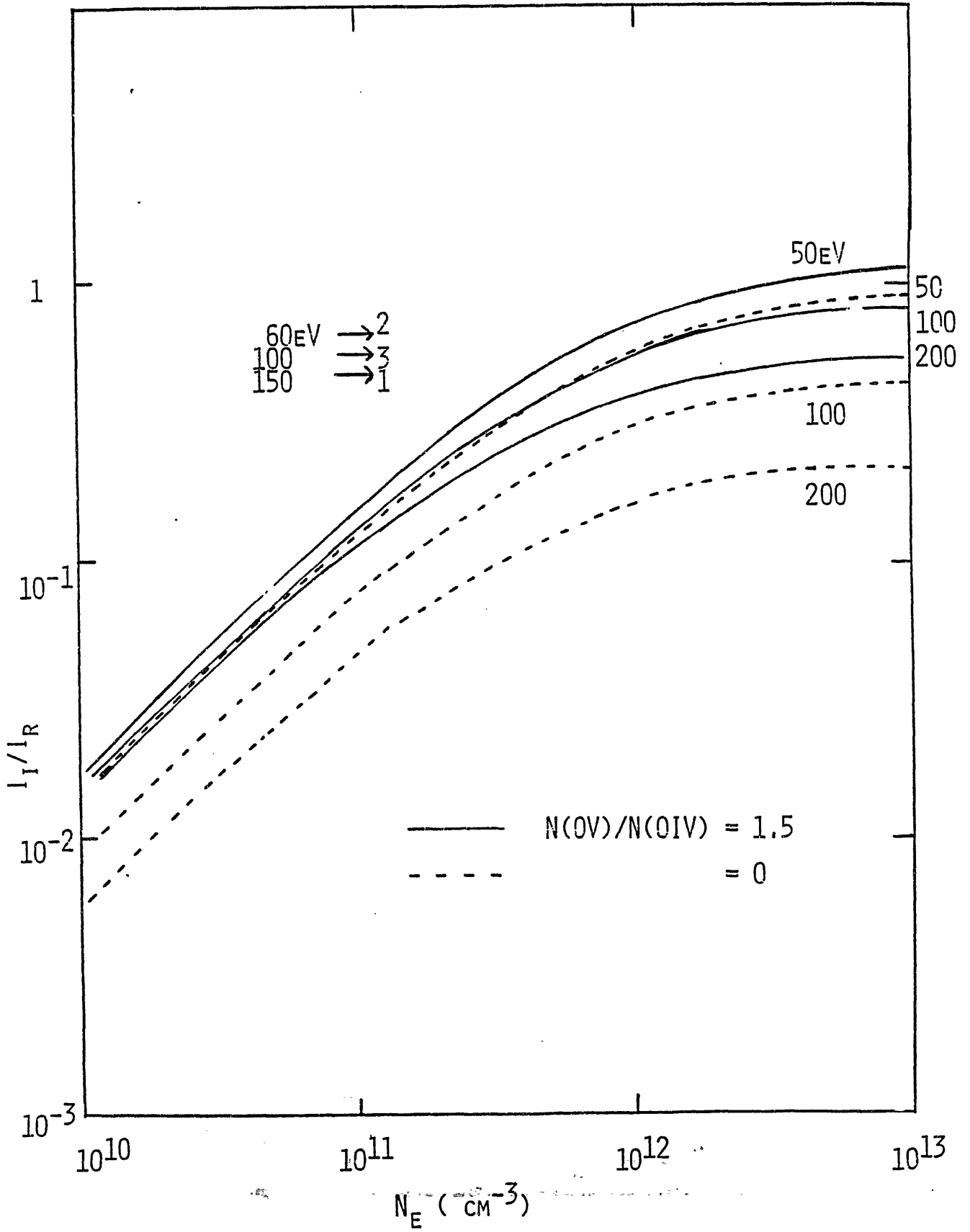


Fig. 7(a)

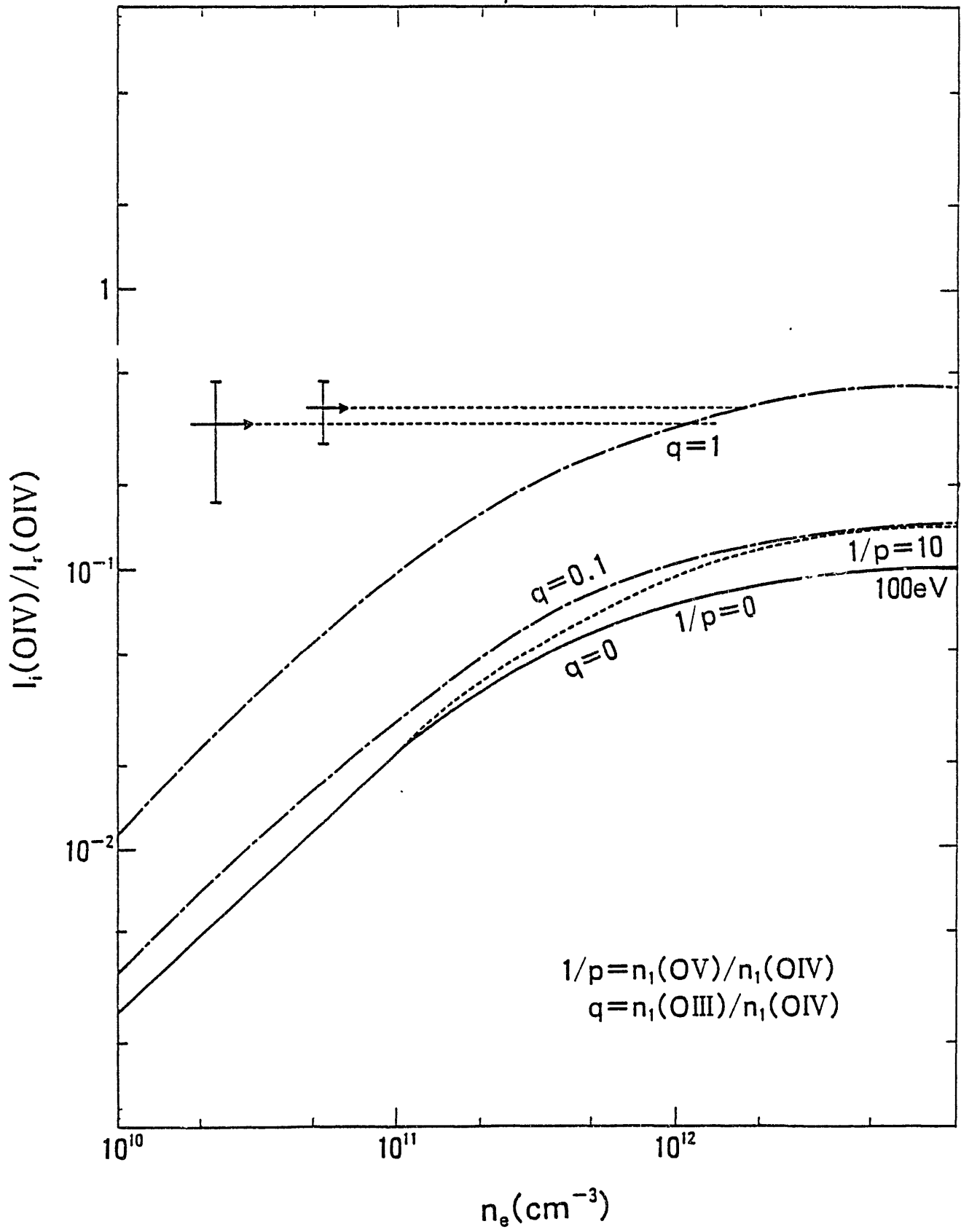


Fig. 7(b)

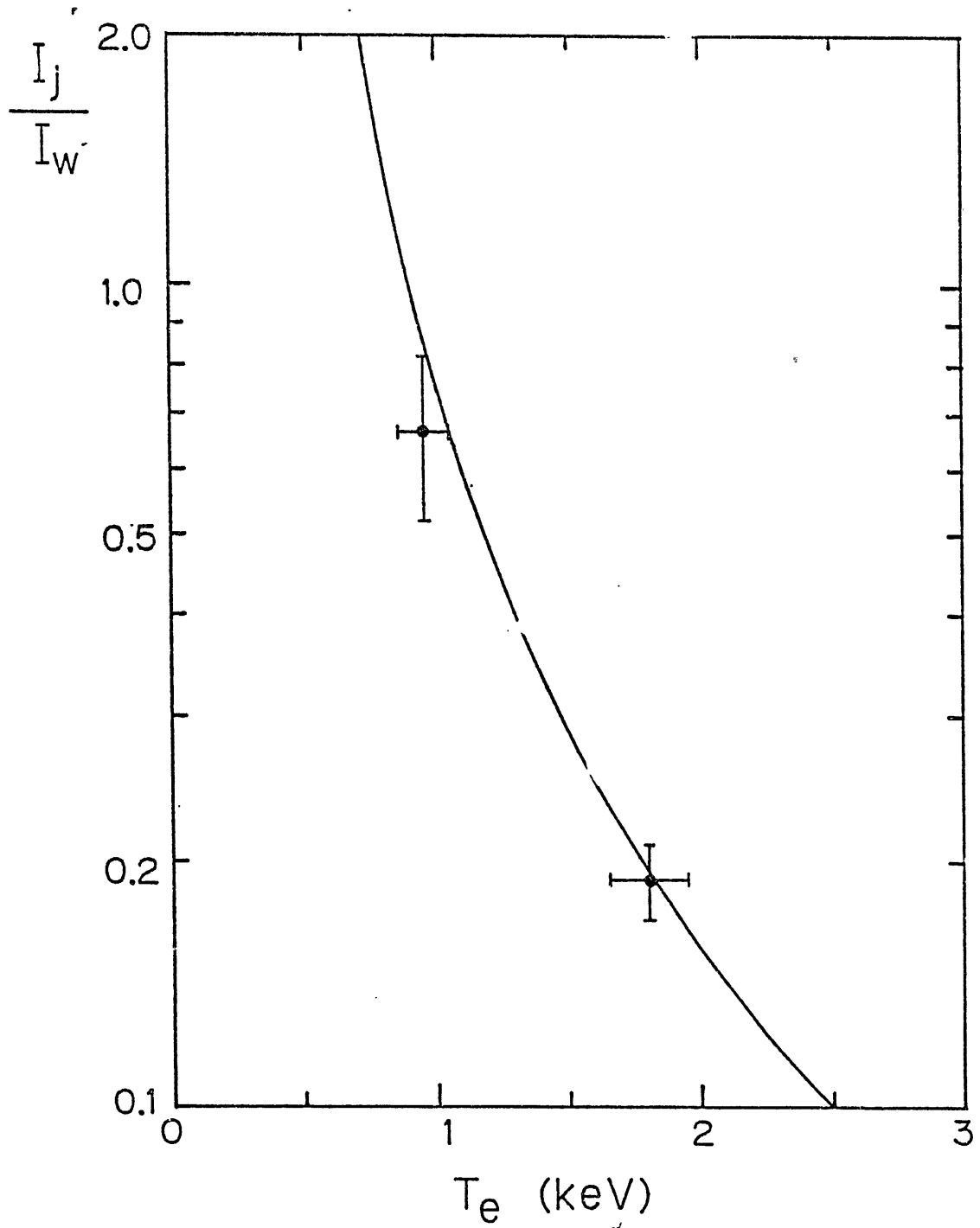


Fig. 8(a)

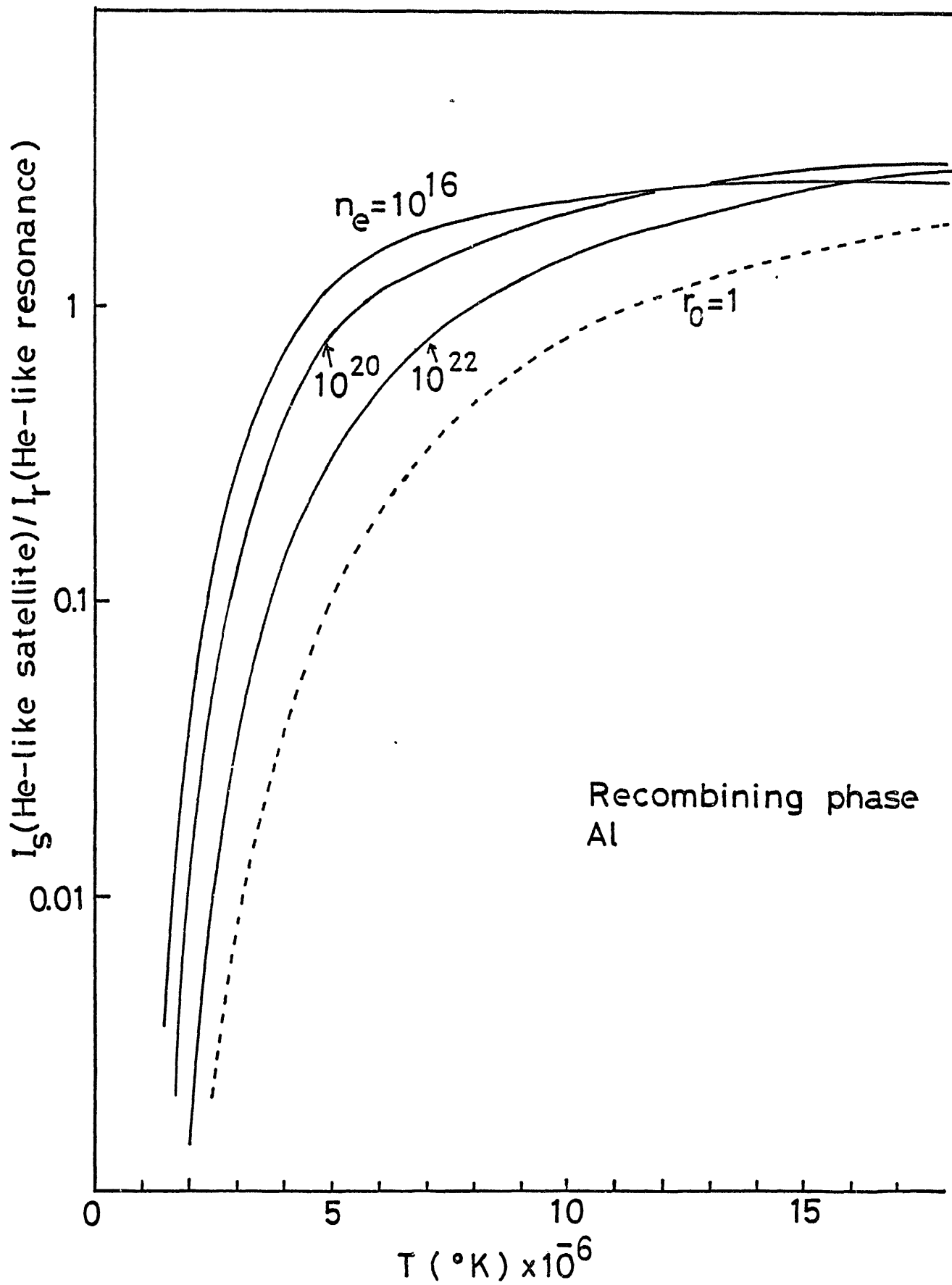


Fig. 8(b)

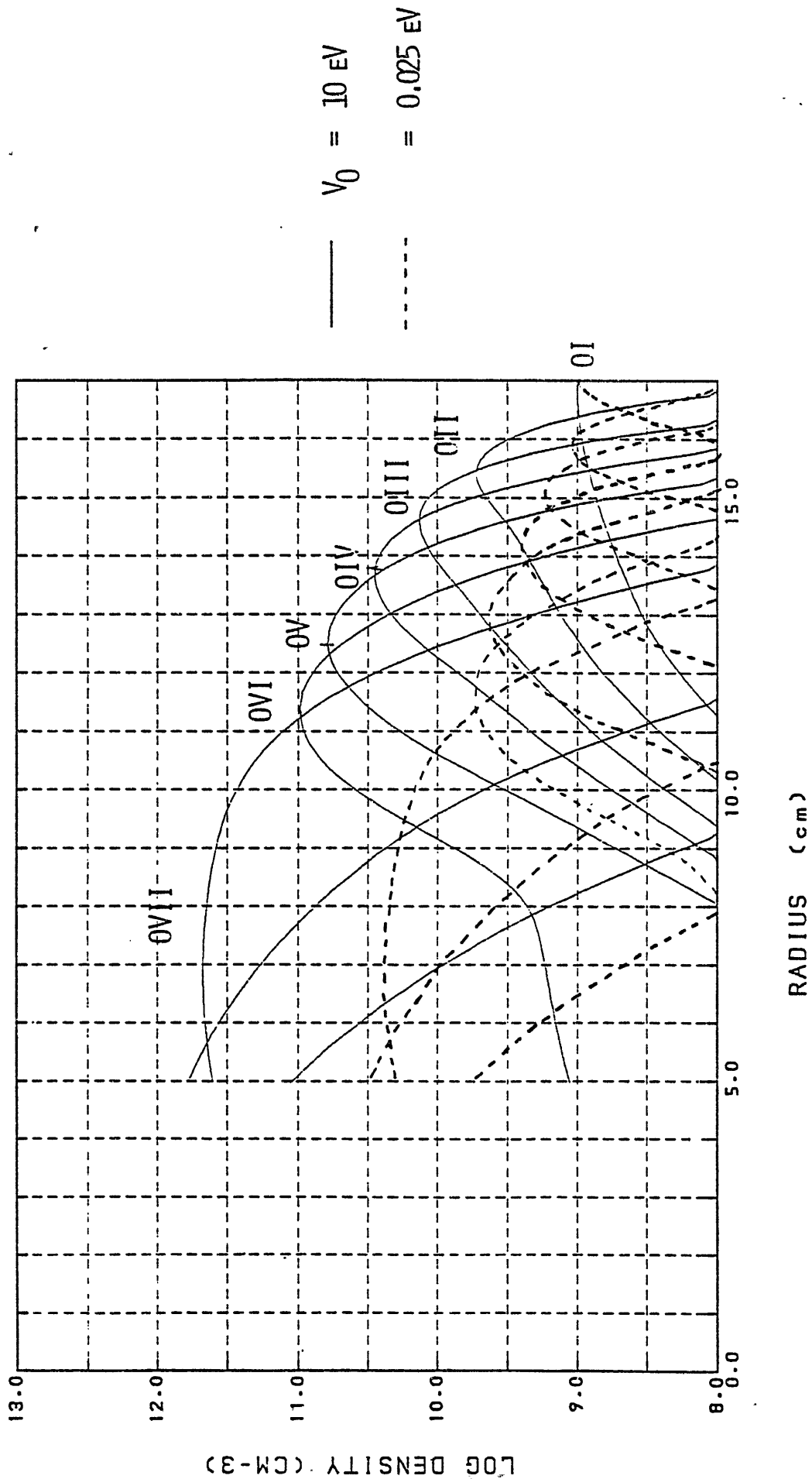


Fig. 9

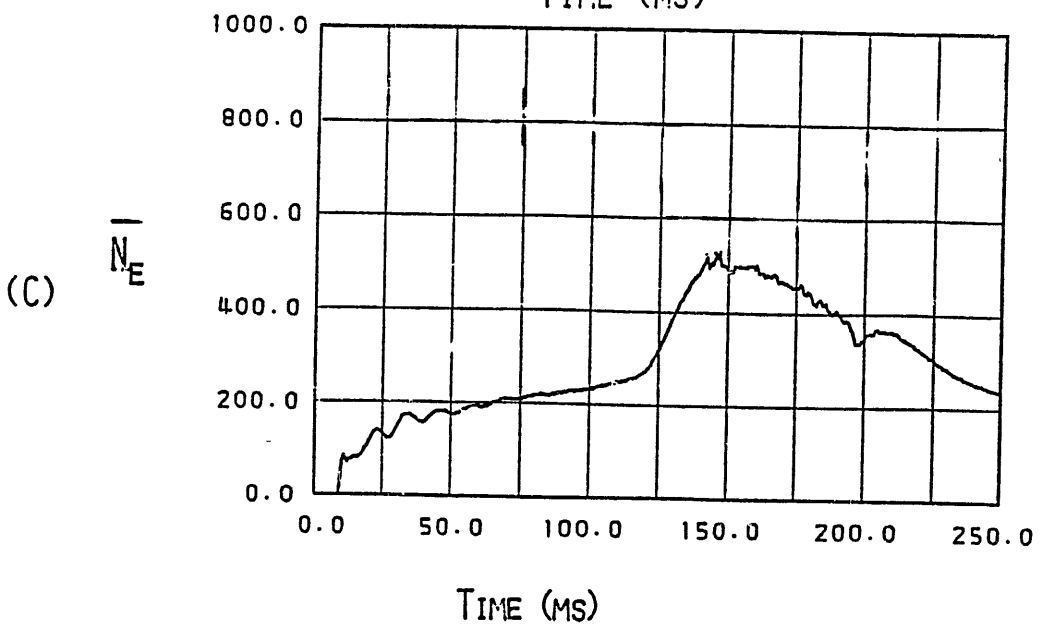
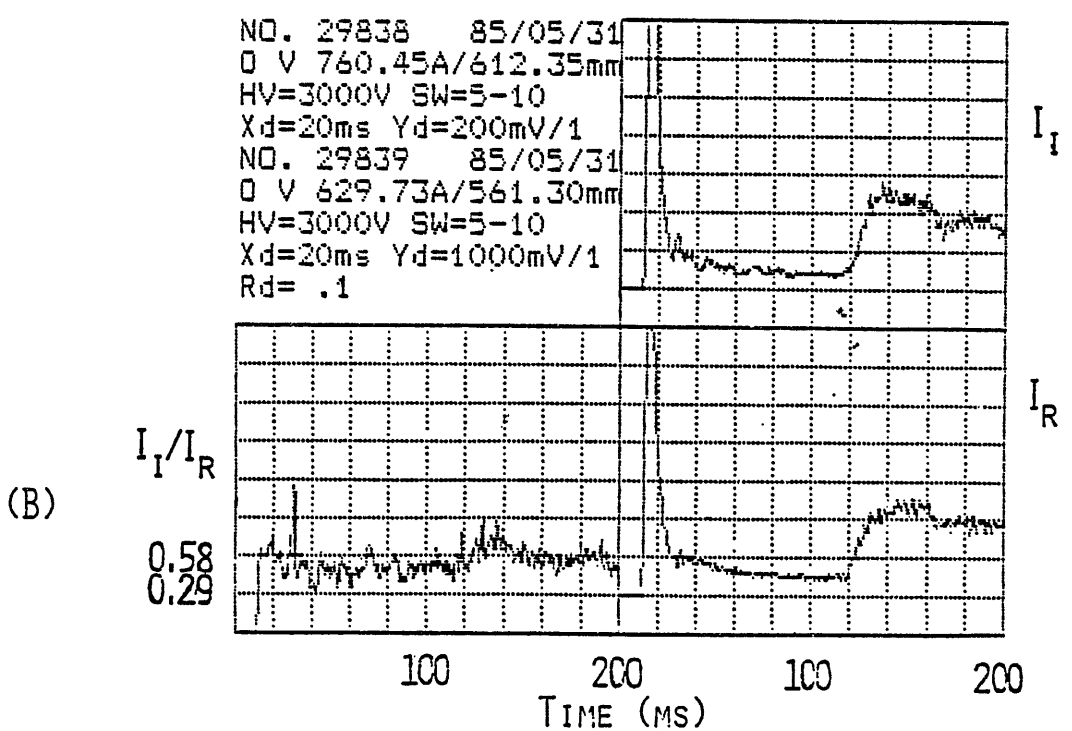
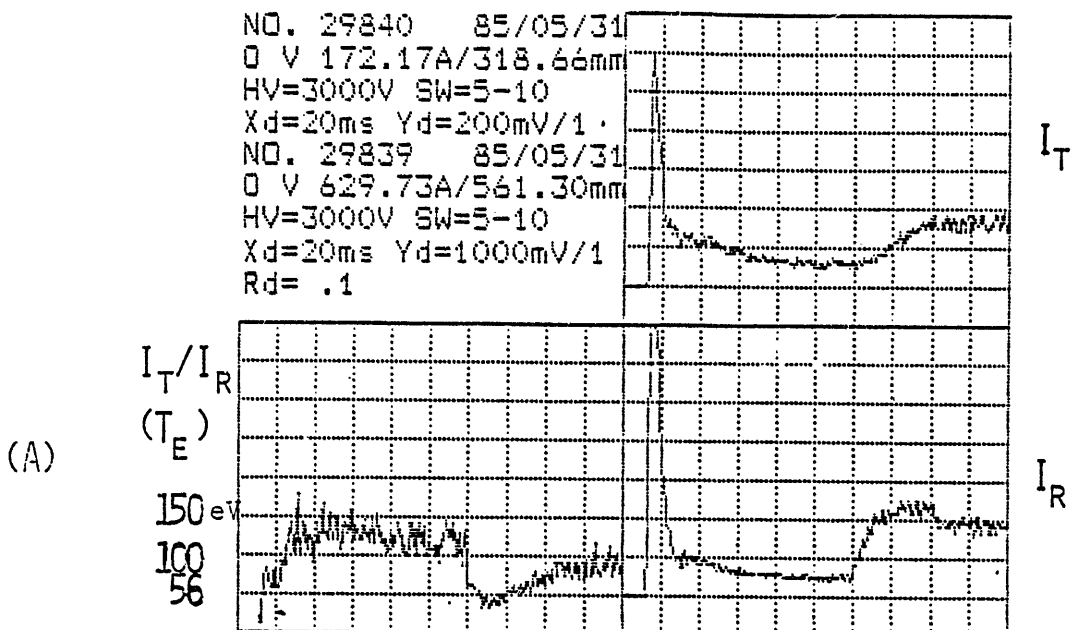


Fig. 10

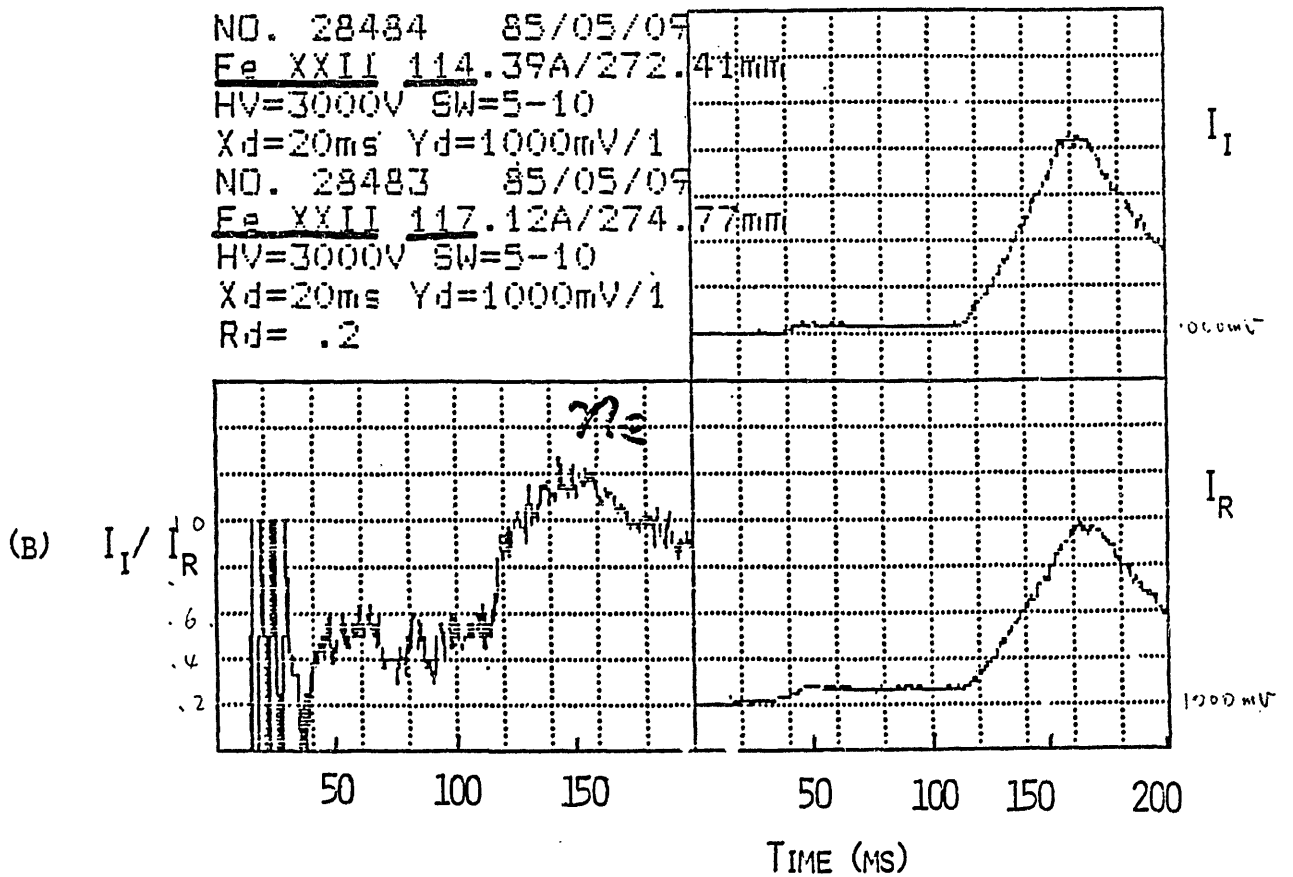
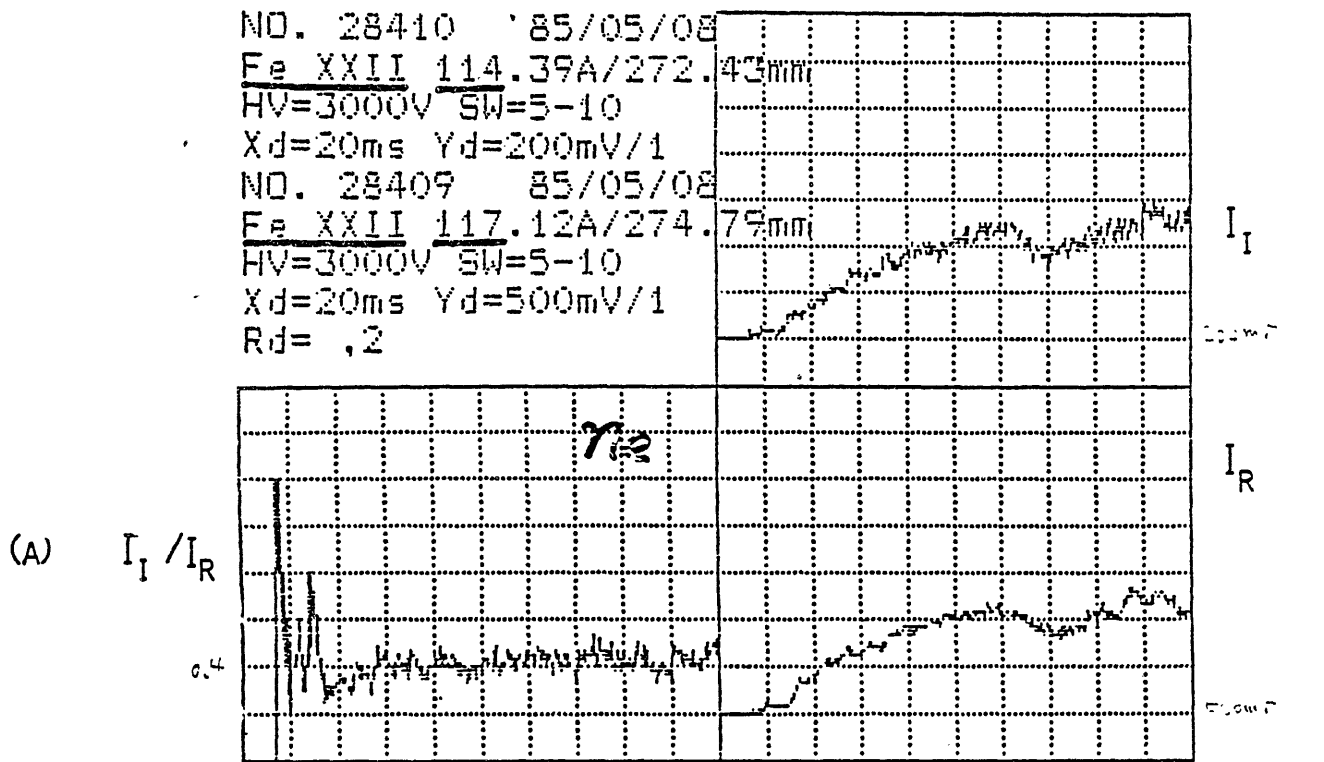


Fig. 11

3 - 16 - 1985 JSHDT - 26281 26282 26283 26284 26285 26286 26287 26288 26289 26290 26291 26292 26293 26294 26295 26296 26297 26298
 26299 26300 26301 26302

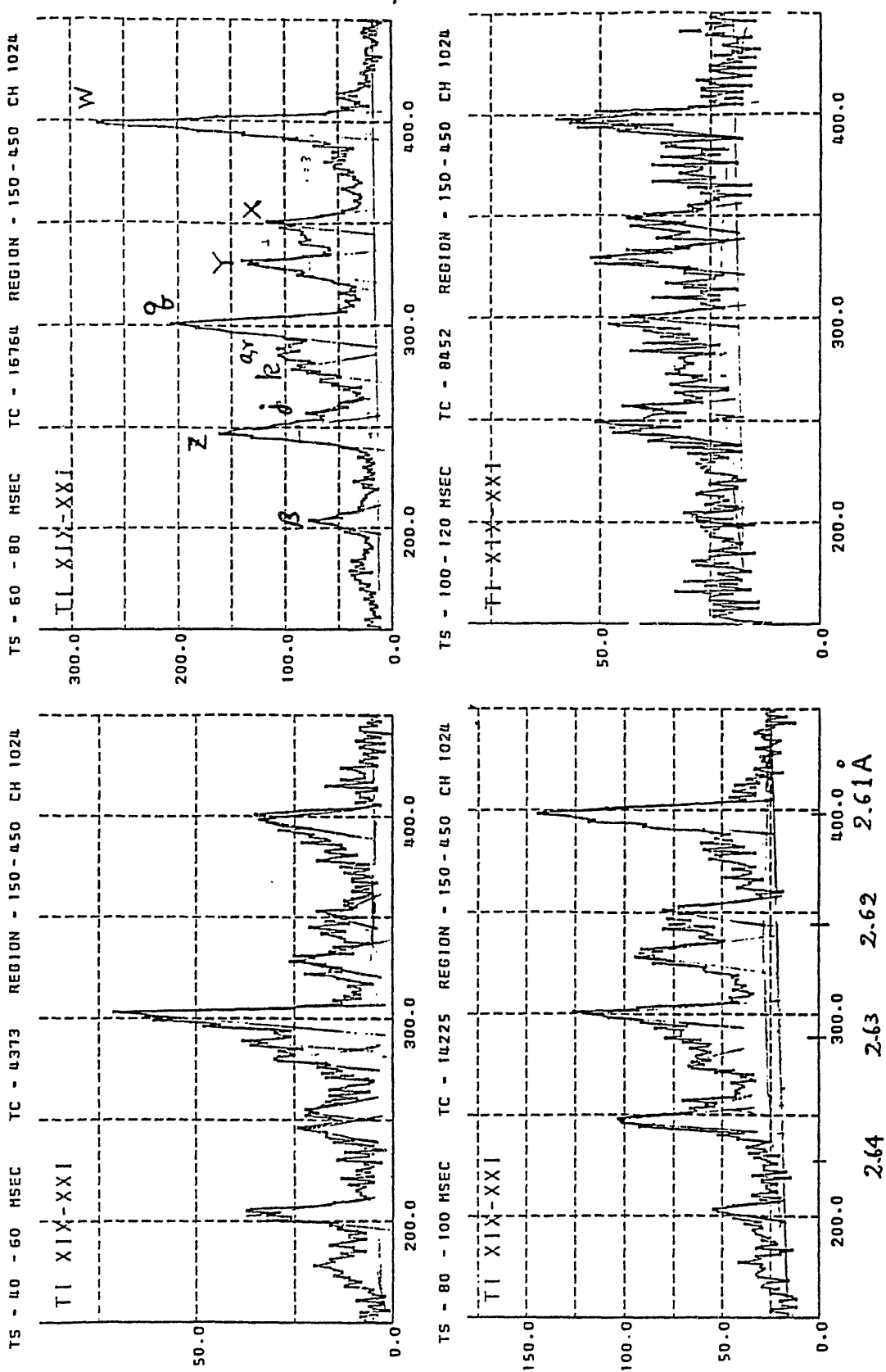


Fig. 12

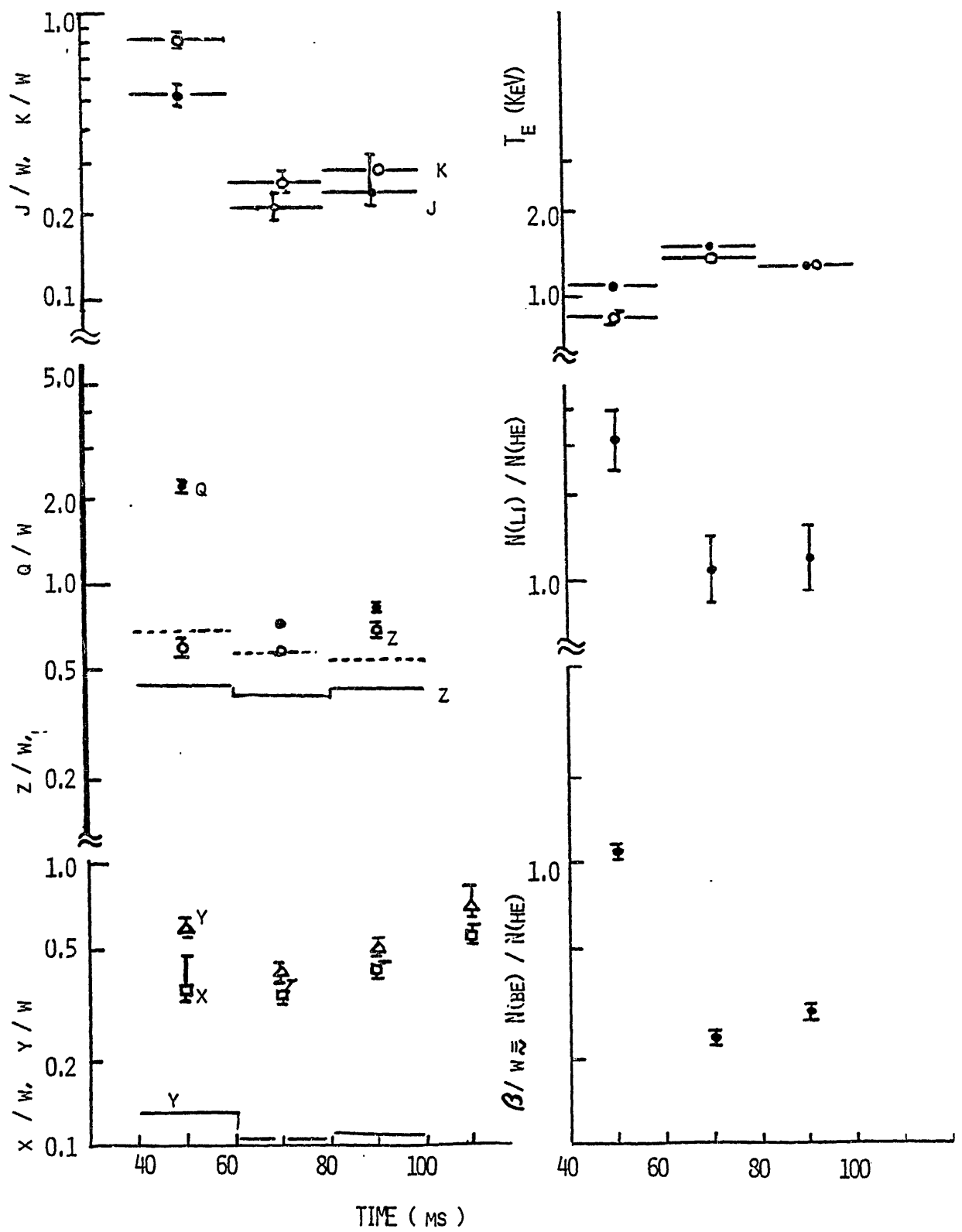


Fig. 13

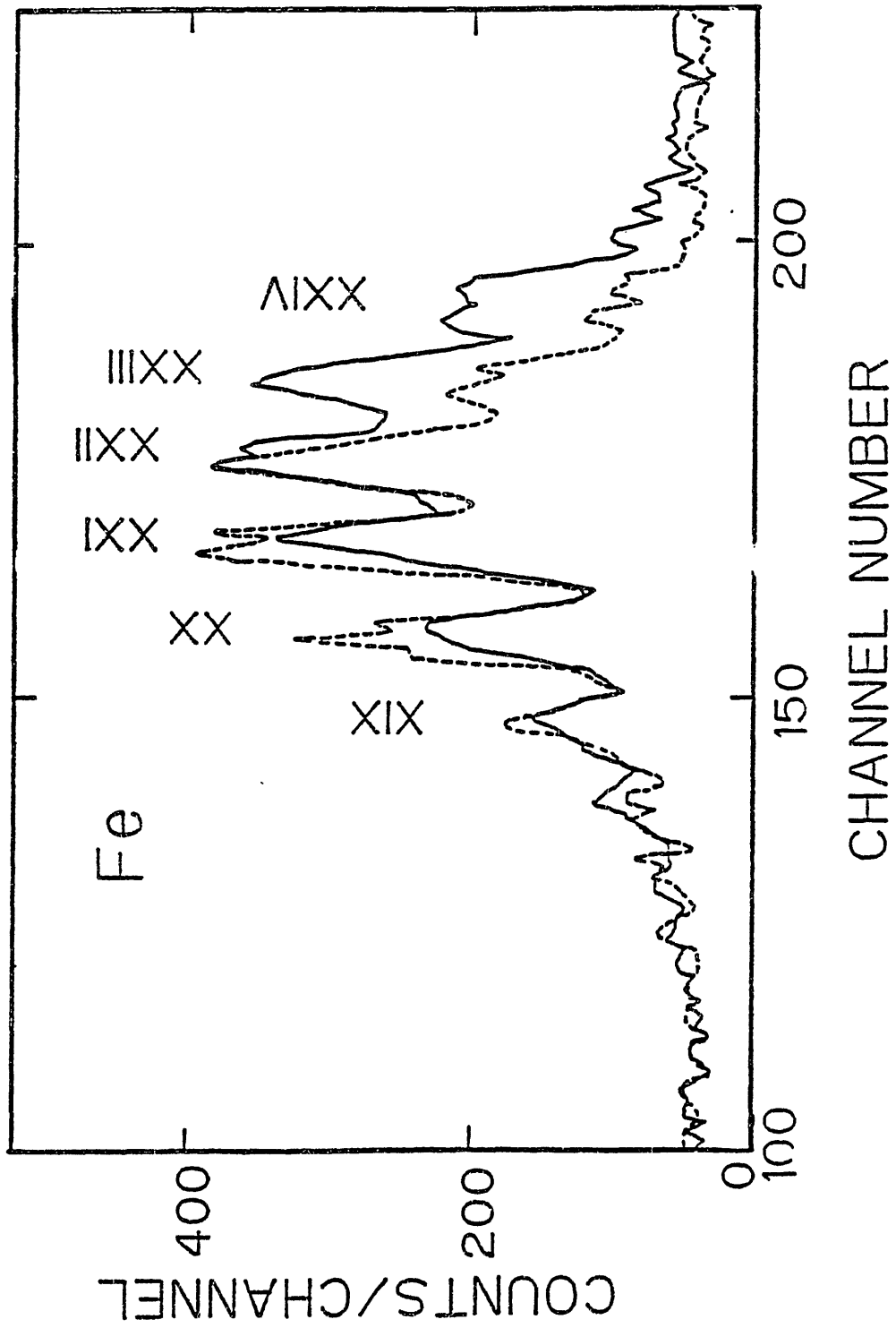
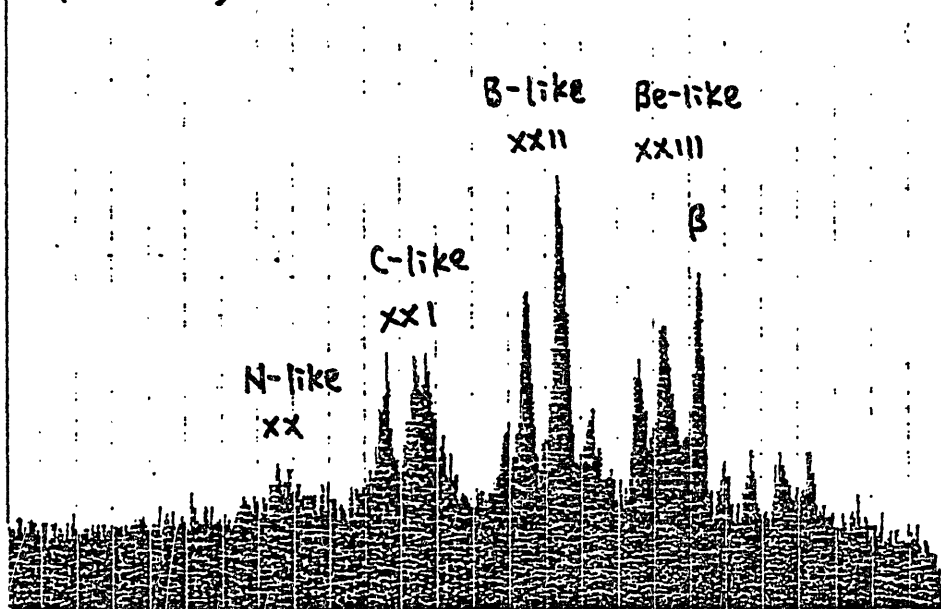


Fig. 14

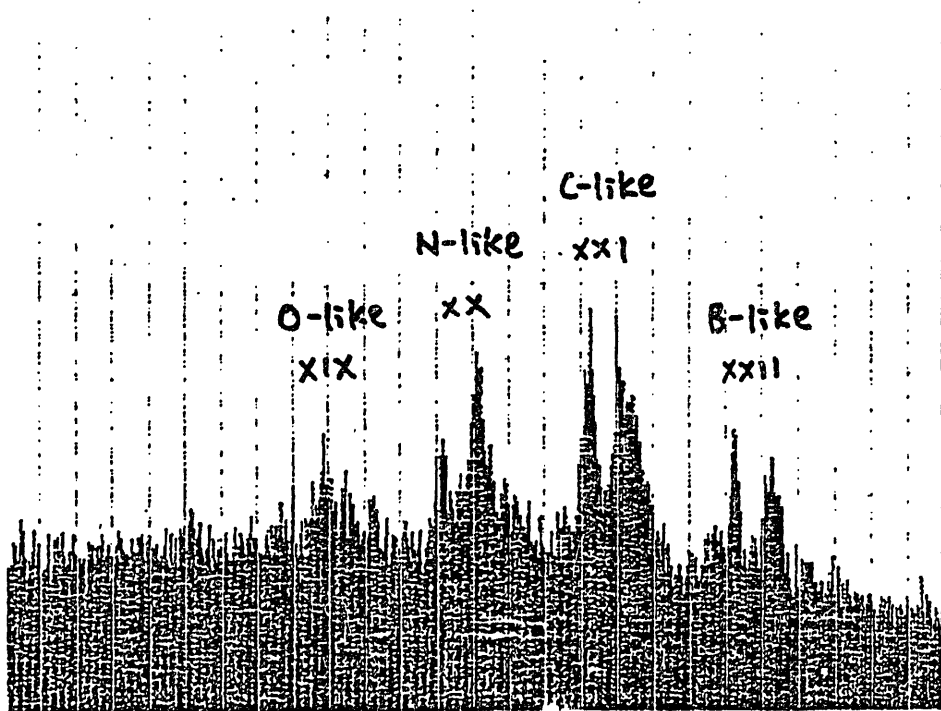
109/ 135 ROI101 0: 1024 = 105365 GROSS

Fe ($Z=26$)



109 2/4 CG=4095 LT= 0 RT= 0 1KFS 621

614/ 65 ROI103 0: 1024 = 74102 GROSS



103 2/4 CG=4095 LT= 0 RT= 0 512 FS 615

Fig. 15

AM data for Fe

--data available and data needed--

H. Tawara

IPP, Nagoya

Data for a number of AM processes involving Fe atoms and ions in different ionization stage are required for plasma and fusion research. In the following is given a short summary of AM data compilation and evaluation of various AM processes of Fe/Fe^{q+} which have been done mainly at RIC/Nagoya.

I) Sputtering of Fe by ions (stored as database SPUTY)

a) Data available

Data for total sputtering yields, their angular distribution¹⁾ and their dependence on incident angle²⁾ have been investigated and compiled. Empirical formulas for estimating the sputtering yields for any ion-(monatomic)solid target combination including D, T and He ions have been proposed and found to give fairly good agreement with experimental and simulation data. Also the threshold behavior of sputtering yields has been analyzed and found to be given by $Y \sim (E - E_{th})^{1/2}$, where E_{th} is the threshold energy for sputtering, depending on the incident angle and mass ratio of ion and target³⁾.

b) Data needed

1. the fraction of ions and atoms in the ground state and excited states
2. the variation of sputtering yields in O₂ environment
3. sputtering of alloys and compounds: preferential sputtering?

c) References

1. N. Matsunami, Y. Yamamura, Y. Itikawa, N. Itoh, Y. Kazumata, S. Miyagawa, K. Morita, R. Shimizu and H. Tawara, IPPJ-AM-32 (1983) and Atomic Data and Nuclear Data Tables 31 (1984) 1.

2. Y. Yamamura, Y. Itikawa and N. Itoh, IPPJ-AM-26 (1983); Y. Yamamura, Nucl. Instr. Meth. B 2 (1984) 578.
3. Y. Yamamura and Y. Mizuno, IPPJ-AM-40 (1985).

II) Backscattering of ions from Fe (stored as BACKS)

a) Data available

Experimental and simulation data for backscattering of ions from Fe targets have been compiled and evaluated¹⁾. Universal empirical formulas on number- and energy- backscattering coefficients including the dependence on the incident angle for H, D, T, ³He and ⁴He have been found over the energy of $10\text{-}3 \times 10^4$ eV²⁾. Furthermore these formulas have been modified to include heavier ions such as Cs³⁾.

b) Data needed

1. data for very low energies ($E < 10$ eV) where chemical effects become important. Some calculations have shown that backscattering becomes extremely low and practically zero for 0.1 eV H on Ni⁴⁾.
2. Enhanced trapping of H atoms at very low energies?

c) References

1. R. Ito, T. Tabata, N. Itoh, K. Morita, T. Kato and H. Tawara, IPPJ-AM-41 (1985).
2. T. Tabata, R. Ito, Y. Itikawa, N. Itoh, K. Morita and H. Tawara, IPPJ-AM-34 (1984); T. Tabata, R. Ito, K. Morita and H. Tawara, Rad. Eff. 85 (1985) 45.
3. R. Ito, T. Tabata, K. Morita and H. Tawara, unpublished.
4. M. I. Baskes, J. Nucl. Mat. 128/129 (1984) 676.

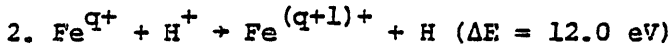
III) Charge transfer and ionization of Fe/ Fe^{q+} in collisions with H, H₂, H⁺, He, He⁺ and He²⁺.

a) Data available

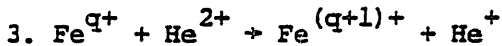
1. $\text{Fe}^{q+} + \text{H}(\text{H}_2) \rightarrow \text{Fe}^{(q-1)+} + \text{H}^+(\text{H}_2^+)$

Charge transfer (stored as CHART)

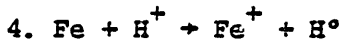
Experimental data for this process have been compiled¹⁾ for $4 \leq q \leq 15$ over the energy range $1 \text{ eV} \sim 10^2 \text{ eV/amu}$ and $\sim 10^5 \text{ eV/amu}$ and empirical formula has been proposed²⁾.



The calculated cross sections for $q=1$ behave like near-resonant process and increase with decreasing the collision energy ($3 \times 10^{-15} \text{ cm}^2$ at 1 eV)³⁾. Also the cross sections for $q=7, 15, 23$ over the energy range $10 \text{ keV/amu} \sim 1 \text{ GeV/amu}$ show broad maximum ($\sim 10^{-22} \text{ cm}^2$) at 500 keV/amu for $q=7$ ⁴⁾ and those for $q=25$ over $1 \sim 100 \text{ MeV/amu}$ show maximum ($\sim 4 \times 10^{-25} \text{ cm}^2$) at 10 MeV/amu ⁵⁾.



The cross sections for $q=25$ over $10 \sim 500 \text{ MeV/amu}$ have been calculated with a maximum ($4 \times 10^{-25} \text{ cm}^2$ at 100 MeV/amu)⁶⁾.



The calculation shows maximum cross sections ($\sim 6 \times 10^{-16} \text{ cm}^2$ at 5 keV/amu)⁷⁾.



These ionization cross sections could be calculated in principle at least for high energies, though no experimental data are available except for



over $1.5 \sim 27 \text{ keV}$ ⁸⁾ (Note 2).

b) Data needed

1. systematic measurements of cross sections over a wide range of the collision energy
2. partial cross sections over (n, l) distributions (compilation is under way at RIC/Nagoya)
3. $\text{Fe}^{q+} + \text{He} \rightarrow \text{Fe}^{(q-1)+} + \text{He}^+$
4. ionization cross section (see the process 5 above)

c) References

1. H. Tawara, T. Kato and Y. Nakai, IPPJ-AM-28, -30 (1983); Atomic Data and Nuclear Data Tables 32 (1985) 235.
2. Y. Kaneko, T. Arikawa, Y. Itikawa, T. Iwai, T. Kato, M. Matsuzawa, Y. Nakai, K. Okuno, H. Ryufuku, H. Tawara and T. Watanabe, IPPJ-AM-15 (1980).
3. U. P. Zhdanov and M. I. Chibisov, Soc. J. Plasma Phys. 3 (1977) 406.
4. K. Fujiwara, J. Phys Soc. Japan 41 (1976) 1350.
5. M. Lal, A. N. Tripathi and M. K. Srivastava, J. Phys. B 11 (1978) 4249.
6. M. Lal, M. K. Srivastava and A. N. Tripathi, Phys. Rev. A 26 (1982) 305.
7. S. Hiraide, Y. Kigoshi and M. Matsuzawa, IPPJ-AM-5 (1978).
8. P. A. Hobbs et al., unpublished (1979).

IV) Excitation of Fe and Fe^{q+} by electrons (stored as AMDIS)

No experimental data are available except for some few based upon plasma experiments for Fe VIII-X. A general review is given by Bazylev and Chibisov¹⁾.

In AMDIS the numbers of theoretical calculations of excitation for Fe^{q+} ions by electrons are summarized as follows:

q	25	24	23	22	18	16	15	14	11	8	others
records	8	91	9	2	33	20	36	23	190	78	0

References

1. V. A. Bazylev and M. I. Chibisov, Sov. Phys-USP. 24 (1981) 276.

V) Ionization of Fe and Fe^{q+} by electrons

a) Data available (stored as AMDIS)

Experimental data are available only for q=1,2 over Eth~1.5 keV¹⁾. Systematic calculations for direct ionization processes over q=0-25 have

been made by Younger. Generally his calculations are smaller than the values based on Lotz empirical formula and in particular the former are about half the latter for high q . It should be noted that for many electron ions the indirect processes such as excitation-autoionization or resonant recombination-double autoionization processes play a key role in ionization and these cross sections become large and sometimes ten times larger than those by direct processes²⁾.

b) Data needed

1. the cross sections for direct processes as well as those for indirect processes
2. data for multiple ionization processes
3. contribution from innershell ionization processes
4. enhancement of ionization at high density plasmas
5. the effect of radiative transition, compared with that due to autoionization

c) References

1. H. Tawara, T. Kato and M. Ohnishi, IPPJ-AM-37 (1985).
2. D. H. Crandall, Atomic Physics of Highly Ionized Atoms (Ed. R. Marrus, 1982, Plenum Press) p. 399.

VI) Innershell ionization of Fe and Fe^{q+} by electrons, protons and helium ions

a) Data available

K- and L-shell ionization cross sections by electrons¹⁾, protons and helium²⁾ ions are compiled and reviewed for Fe atoms. No data are available for Fe^{q+} ions.

b) Data needed

1. data for Fe^{q+} ions (also see III-5, V)
2. the fluorescence yields for different ionization states

c) References

1. C. J. Powell, Rev. mod. Phys. 48 (1976) 33; H. Kolbenstredt, J. appl. Phys. 38 (1970) 4785; J. H. Scofield, Phys. Rev. A 18 (1978) 563.
2. R. K. Gardner and T. J. Gray, Atomic Data and Nucl. Data Tables 21 (1978) 515; H. Paul, *ibid* 24 (1979) 243; R. S. Sokhi and D. Crumpton, *ibid* 30 (1984) 49.

VII) Spectroscopic data

a) Data available

1. A previous version of Grotrian diagram for Fe VIII-XXVI¹⁾ is under revision.
2. ORNL-6086 (1985) has summarized the present situations on 1) transition energies (NIR-VUV), 2) energy levels and 3) transition probabilities for Fe I-XXVI²⁾.
3. K X-ray energy data for Fe⁹⁺ ions are being compiled at RIC/Nagoya.

b) References

1. K. Mori, M. Otsuka and T. Kato, Atomic Data and Nucl. Data Tables 23 (1979) 196.
2. W. Wiese (ed.), ORNL-6086 (1985).

The Co-operative Workshop on Tokamak Plasma Modelling and Atomic Processes

Institute of Plasma Physics, Nagoya University, Nagoya 464, Japan

July 8 - 9, 1985

Workshop Program

July 8, Monday, 13:30 - 17:00

1. Present Status of Atomic Data Needed for Plasma Modelling
T. Kawamura(IPP, Nagoya Univ.)
2. Particle Control in a Tokamak
S. Sengoku (JAERI)
3. Tokamak Simulation Based on Selfconsistent Plasma-Wall Interaction
T. Hirayama (JAERI)

July 9, Tuesday, 9:30 - 12:00

4. Modelling for Ablation of Solid Pellets
Y. Nakamura (Kyoto Univ.)
5. Simulation of Impurity Transport in Tokamaks
T. Amano(IPP, Nagoya Univ.)
6. X-Ray Spectroscopy in JIPPT-II Experiments
S. Morita (IPP, Nagoya Univ.)
7. Dependences of VUV Spectra on Electron Temperature and Density
K. Masai (IPP, Nagoya Univ.)

July 9, Tuesday, 13:30 - 17:00

8. Modelling of Interstellar Medium with X-Ray Observations
S. Hayakawa (Nagoya Univ.)
9. A Comment from a Plasma Spectroscopist-----Ionizing Plasma and
Recombining Plasma
T. Fujimoto(Kyoto Univ.)
10. Effects of Multistep Ionization and Inner-Shell Ionization on Modelling
T. Kato (IPP, Nagoya Univ.)
11. AM Data Base in RIC-IPP
H. Tawara (IPP, Nagoya Univ.)

List of Participants

AMAMO, Tsuneo	Institute of Plasma Physics, Nagoya University
FUJIMOTO, Takashi	Department of Engineering Science, Kyoto University
FUJITA, Junji	Institute of Plasma Physics, Nagoya University
HAYAKAWA, Satio	Department of Astrophysics, Nagoya University
HIRAYAMA, Toshio	Japan Atomic Energy Research Institute
KATO, Takako	Institute of Plasma Physics, Nagoya University
KAWAMURA, Takaichi	Institute of Plasma Physics, Nagoya University
KAWATO, Eizo	Institute of Plasma Physics, Nagoya University
MASAI, Kuniaki	Institute of Plasma Physics, Nagoya University
MIYAHARA, Akira	Institute of Plasma Physics, Nagoya University
MIZUI, Jun-ichi	Institute of Plasma Physics, Nagoya University
MORITA, Sigeru	Institute of Plasma Physics, Nagoya University
NAKAI, Yohta	Japan Atomic Energy Research Institute
NAKAMURA, Yuji	Faculty of Engineering, Kyoto University
NODA, Nobuaki	Institute of Plasma Physics, Nagoya University
OGAWA, Yuichi	Institute of Plasma Physics, Nagoya University
OKUNO, Kazuhiko	Faculty of Science, Tokyo Metropolitan University
ONO, Tadayoshi	Department of Physics, Nagoya University
SAKIMOTO, Kazuhiro	Institute of Space and Astronautical Science
SENGOKU, Seio	Japan Atomic Energy Research Institute
TANAKA, Motohiko	Institute for Fusion Theory, Hiroshima University
TAWARA, Hiroyuki	Institute of Plasma Physics, Nagoya University

LIST OF IPPJ-AM REPORTS

- IPPJ-AM-1* "Cross Sections for Charge Transfer of Hydrogen Beams in Gases and Vapors in the Energy Range 10 eV–10 keV"
H. Tawara (1977) [Published in Atomic Data and Nuclear Data Tables 22, 491 (1978)]
- IPPJ-AM-2* "Ionization and Excitation of Ions by Electron Impact –Review of Empirical Formulae–"
T. Kato (1977)
- IPPJ-AM-3 "Grotrian Diagrams of Highly Ionized Iron FeVIII-FeXXVI"
K. Mori, M. Otsuka and T. Kato (1977) [Published in Atomic Data and Nuclear Data Tables 23, 196 (1979)]
- IPPJ-AM-4 "Atomic Processes in Hot Plasmas and X-Ray Emission"
T. Kato (1978)
- IPPJ-AM-5* "Charge Transfer between a Proton and a Heavy Metal Atom"
S. Hiraide, Y. Kigoshi and M. Matsuzawa (1978)
- IPPJ-AM-6* "Free-Free Transition in a Plasma –Review of Cross Sections and Spectra–"
T. Kato and H. Narumi (1978)
- IPPJ-AM-7* "Bibliography on Electron Collisions with Atomic Positive Ions: 1940 Through 1977"
K. Takayanagi and T. Iwai (1978)
- IPPJ-AM-8 "Semi-Empirical Cross Sections and Rate Coefficients for Excitation and Ionization by Electron Collision and Photoionization of Helium"
T. Fujimoto (1978)
- IPPJ-AM-9 "Charge Changing Cross Sections for Heavy-Particle Collisions in the Energy Range from 0.1 eV to 10 MeV I. Incidence of He, Li, Be, B and Their Ions"
Kazuhiko Okuno (1978)
- IPPJ-AM-10 "Charge Changing Cross Sections for Heavy-Particle Collisions in the Energy Range from 0.1 eV to 10 MeV II. Incidence of C, N, O and Their Ions"
Kazuhiko Okuno (1978)
- IPPJ-AM-11 "Charge Changing Cross Sections for Heavy-Particle Collisions in the Energy Range from 0.1 eV to 10 MeV III. Incidence of F, Ne, Na and Their Ions"
Kazuhiko Okuno (1978)
- IPPJ-AM-12* "Electron Impact Excitation of Positive Ions Calculated in the Coulomb-Born Approximation –A Data List and Comparative Survey–"
S. Nakazaki and T. Hashino (1979)
- IPPJ-AM-13 "Atomic Processes in Fusion Plasmas – Proceedings of the Nagoya Seminar on Atomic Processes in Fusion Plasmas Sept. 5-7, 1979"
Ed. by Y. Itikawa and T. Kato (1979)
- IPPJ-AM-14 "Energy Dependence of Sputtering Yields of Monatomic Solids"
N. Matsunami, Y. Yamamura, Y. Itikawa, N. Itoh, Y. Kazumata, S. Miyagawa, K. Morita and R. Shimizu (1980)

- IPPJ-AM-15 "Cross Sections for Charge Transfer Collisions Involving Hydrogen Atoms"
Y. Kaneko, T. Arikawa, Y. Itikawa, T. Iwai, T. Kato, M. Matsuzawa, Y. Nakai,
K. Okubo, H. Ryufuku, H. Tawara and T. Watanabe (1980)
- IPPJ-AM-16 "Two-Centre Coulomb Phaseshifts and Radial Functions"
H. Nakamura and H. Takagi (1980)
- IPPJ-AM-17 "Empirical Formulas for Ionization Cross Section of Atomic Ions for Elec-
tron Collisions –Critical Review with Compilation of Experimental Data–"
Y. Itikawa and T. Kato (1981)
- IPPJ-AM-18 "Data on the Backscattering Coefficients of Light Ions from Solids"
T. Tabata, R. Ito, Y. Itikawa, N. Itoh and K. Morita (1981) [Published in
Atomic Data and Nuclear Data Tables 28, 493 (1983)]
- IPPJ-AM-19 "Recommended Values of Transport Cross Sections for Elastic Collision and
Total Collision Cross Section for Electrons in Atomic and Molecular Gases"
M. Hayashi (1981)
- IPPJ-AM-20 "Electron Capture and Loss Cross Sections for Collisions between Heavy
Ions and Hydrogen Molecules"
Y. Kaneko, Y. Itikawa, T. Iwai, T. Kato, Y. Nakai, K. Okuno and H. Tawara
(1981)
- IPPJ-AM-21 "Surface Data for Fusion Devices – Proceedings of the U.S.–Japan Work-
shop on Surface Data Review Dec. 14-18, 1981"
Ed. by N. Itoh and E.W. Thomas (1982)
- IPPJ-AM-22 "Desorption and Related Phenomena Relevant to Fusion Devices"
Ed. by A. Koma (1982)
- IPPJ-AM-23 "Dielectronic Recombination of Hydrogenic Ions"
T. Fujimoto, T. Kato and Y. Nakamura (1982)
- IPPJ-AM-24 "Bibliography on Electron Collisions with Atomic Positive Ions: 1978
Through 1982 (Supplement to IPPJ-AM-7)"
Y. Itikawa (1982) [Published in Atomic Data and Nuclear Data Tables 31,
215 (1984)]
- IPPJ-AM-25 "Bibliography on Ionization and Charge Transfer Processes in Ion-Ion
Collision"
H. Tawara (1983)
- IPPJ-AM-26 "Angular Dependence of Sputtering Yields of Monatomic Solids"
Y. Yamamura, Y. Itikawa and N. Itoh (1983)
- IPPJ-AM-27 "Recommended Data on Excitation of Carbon and Oxygen Ions by Electron
Collisions"
Y. Itikawa, S. Hara, T. Kato, S. Nakazaki, M.S. Pindzola and D.H. Crandall
(1983) [Published in Atomic Data and Nuclear Data Tables 33, 149 (1985)]
- IPPJ-AM-28 "Electron Capture and Loss Cross Sections for Collisions Between Heavy
Ions and Hydrogen Molecules (Up-dated version of IPPJ-AM-20)
H. Tawara, T. Kato and Y. Nakai (1983) [Published in Atomic Data and
Nuclear Data Tables 32, 235 (1985)]

- IPPJ-AM-29 "Bibliography on Atomic Processes in Hot Dense Plasmas"
T. Kato, J. Hama, T. Kagawa, S. Karashima, N. Miyanaga, H. Tawara,
N. Yamaguchi, K. Yamamoto and K. Yonei (1983)
- IPPJ-AM-30 "Cross Sections for Charge Transfers of Highly Ionized Ions in Hydrogen
Atoms (Up-dated version of IPPJ-AM-15)"
H. Tawara, T. Kato and Y. Nakai (1983) [Published in Atomic Data and
Nuclear Data Tables 32, 235 (1985)]
- IPPJ-AM-31 "Atomic Processes in Hot Dense Plasmas"
T. Kagawa, T. Kato, T. Watanabe and S. Karashima (1983)
- IPPJ-AM-32 "Energy Dependence of the Yields of Ion-Induced Sputtering of Monatomic
Solids"
N. Matsunami, Y. Yamamura, Y. Itikawa, N. Itoh, Y. Kazumata, S. Miyagawa,
K. Morita, R. Shimizu and H. Tawara (1983) [Published in Atomic Data and
Nuclear Data Tables 31, 1 (1984)]
- IPPJ-AM-33 "Proceedings on Symposium on Atomic Collision Data for Diagnostics and
Modelling of Fusion Plasmas, Aug. 29 – 30, 1983"
Ed. by H. Tawara (1983)
- IPPJ-AM-34 "Dependence of the Backscattering Coefficients of Light Ions upon Angle of
Incidence"
T. Tabata, R. Ito, Y. Itikawa, N. Itoh, K. Morita and H. Tawara (1984)
- IPPJ-AM-35 "Proceedings of Workshop on Synergistic Effects in Surface Phenomena
Related to Plasma-Wall Interactions, May 21 – 23, 1984"
Ed. by N. Itoh, K. Kamada and H. Tawara (1984) [Published in Radiation
Effects 89, 1 (1985)]
- IPPJ-AM-36 "Equilibrium Charge State Distributions of Ions ($Z_1 \geq 4$) after Passage
through Foils – Compilation of Data after 1972"
K. Shima, T. Mikumo and H. Tawara (1985)
- IPPJ-AM-37 "Ionization Cross Sections of Atoms and Ions by Electron Impact"
H. Tawara, T. Kato and M. Ohnishi (1985)
- IPPJ-AM-38 "Rate Coefficients for the Electron-Impact Excitations of C-like Ions"
Y. Itikawa (1985)
- IPPJ-AM-39 "Proceedings of the Japan-U.S. Workshop on Impurity and Particle Control,
Theory and Modeling, Mar. 12 – 16, 1984"
Ed. by T. Kawamura (1985)
- IPPJ-AM-40 "Low-Energy Sputterings with the Monte Carlo Program ACAT"
Y. Yamamura and Y. Mizuno (1985)
- IPPJ-AM-41 "Data on the Backscattering Coefficients of Light Ions from Solids (a
Revision)"
R. Ito, T. Tabata, N. Itoh, K. Morita, T. Kato and H. Tawara (1985)
- IPPJ-AM-42 "Stopping Power Theories for Charged Particles in Inertial Confinement
Fusion Plasmas (Emphasis on Hot and Dense Matters)"
S. Karashima, T. Watanabe, T. Kato and H. Tawara (1985)

- IPPJ-AM-43 “The Collected Papers of Nice Project/IPP, Nagoya”
Ed. by H. Tawara (1985)
- IPPJ-AM-44 “Tokamak Plasma Modelling and Atomic Processes”
Ed. by T. Kawamura (1986)

Available upon request to Research Information Center, Institute of Plasma Physics, Nagoya University, Nagoya 464, Japan, except for the reports noted with*.